UNIVERSITA' DEGLI STUDI DI PADOVA

DEPARTMENT OF INDUSTRIAL ENGINEERING

MASTER DEGREE COURSE IN ELECTRICAL ENGINEERING

MASTER THESIS

"Numerical Models for Induction Hardening of Gears"

SUPERVISOR: Prof. Fabrizio Dughiero

CO-EXAMINER: Eng. Mattia Spezzapria

Prof. Philippe Bocher (ETS, Montréal)

GRADUATE: Damiano Mingardi

SESSION 2012/2013

Ringraziamenti

Nel mio cammino verso la conclusione del lungo periodo da studente universitario ci sono state alcune persone che per me sono state di fondamentale importanza non solo per quanto riguarda aiuto fisico o morale, ma anche solo per la loro splendida presenza.

Voglio pertanto ringraziare dinanzi tutto i miei genitori, che hanno sempre creduto nelle mie capacità e che hanno sempre saputo darmi buoni consigli in questo impegnativo periodo della mia vita.

Un grazie particolare va anche a tutta la famiglia Perin, composta da persone con dei valori davvero inestimabili, che mi è sempre stata vicino.

Un grazie va anche a tutti i miei amici e in particolare Alberto e Alberto, da sempre compagni d'avventure.

Voglio ricordare anche il maestro Pierluigi che mi ha visto impegnato nelle sfide tra le più grandi della mia vita, ed è anche grazie ai suoi insegnamenti che sono arrivato fino a questo traguardo.

Grazie anche a coloro che mi hanno permesso di svolgere questa Tesi: in primis il professor Fabrizio Dughiero, ma anche Mattia per i suoi innumerevoli consigli e il professor Philippe Bocher, che mi ha allegramente accolto e guidato nel periodo trascorso a Montréal.

NUMERICAL MODELS FOR INDUCTION HARDENING OF GEARS

Damiano Mingardi

SUMMARY

Nowadays, induction heat treatment processes are increasingly used in aeronautics and automotive to improve the service performance of several mechanical components such as gears. With induction, heating can be localized to the specific areas where metallurgical changes are desired. For example, in contrast to carburising and nitriding, induction hardening does not require heating of the whole gear and the heating effect on adjacent areas is minimum. Furthermore by its selective heating, the process can produce residual compressive stresses favorable to the fatigue behavior without generating excessive distortion.

The heating and the quenching rate affect the final microstructure of the workpiece, and the case depth generated are machine dependent parameters (frequency, power, preheating and heating times, design of the coil etc). At the current state of the art there are several numerical models able to predict the temperature distribution during the heating process. They allow the designers to avoid a trial and error approach, that is costly and time consuming, to establish the parameters for the induction heating process. Due to the complexity of the phenomena involved in the induction hardening process, in numerical models it is necessary to introduce simplifications such as in the description of the material's properties. These simplifications may lead to errors and substantial differences between the models and the real process of induction hardening. Nevertheless there are no studies in literature that analyze the accuracy of these methods by comparing them with experimental measurements.

Therefore, this thesis involves a study of sensitivity of the hardness profile of a gear heated by induction using finite element method (FEM) software, and it proposes a comparison with experimental measurements of superficial temperature, that is a necessary step towards the development of prediction models.

This study aims at evaluating the effect of machine parameters (frequency, coil dimensions and the presence of a flux concentrator over and below the gear) in order to obtain a homogeneous hardened profile both in the tip and in the tooth of the gear, and to prevent the entire tooth from being austenitised. In particular it is supposed that the flux concentrator has a key role in reducing the edge effect, otherwise difficult to control. In addition a robust method for the measurement of surface temperature fields during fast induction heating treatment is chosen for the comparison to the isotherm obtained by numerical models. It is based on the coupling of temperature indicating

lacquers and a high speed camera system, that allows to extract the temporal evolution of the 816°C and 927°C isotherms. Models with different approximation of the material's properties are proposed, in order to understand their effect on the isotherm's evolution. In addition a comparison between the edge effect estimated by the simulations and the actual one has been proposed by observing the hardened layer.

Keywords: Validation, induction hardening, numerical models, simulation, sensitivity study, experimental, gear, isotherm

NUMERICAL MODELS FOR INDUCTION HARDENING OF GEARS

Damiano Mingardi

Sommario

Al giorno d'oggi, i trattamenti termici ad induzione sono sempre più usati nell'industria aeronautica e automobilistica per migliorare le prestazioni di componenti meccanici quali ruote dentate, cuscinetti ecc. Con il riscaldamento ad induzione è possibile riscaldare selettivamente la parte del materiale in cui si desiderano le modifiche metallurgiche. Per esempio nel processo di tempra ad induzione di ruote dentate è possibile evitare il riscaldamento dell'intero pezzo andando a concentrare il riscaldamento solo superficialmente, cosa non possibile in processi come la carbocementazione e la nitrurazione. Inoltre il processo di tempra ad induzione può portare alla presenza di stress residui di compressione in superficie che migliorano in comportamento a fatica del materiale.

Nei trattamenti termici ad induzione la velocità di riscaldamento e di raffreddamento del pezzo ne influiscono la microstruttura finale, e lo strato temprato dipende da parametri di macchina quali la frequenza, la potenza, la presenza e la durata di una fase di preriscaldo ecc.

Nello stato dell'arte attuale sono presenti diversi modelli numerici in grado di simulare i processi termici ad induzione e quindi di prevedere la distribuzione di temperature nel pezzo in un dato istante. Essi permettono inoltre ai progettisti di evitare un approccio trial and error, lungo e costoso, nello stabilire i parametri di macchina necessari per il risultato voluto.

Data la complessità dei fenomeni coinvolti nella tempra ad induzione, nei modelli numerici è necessario effettuare delle semplificazione ed approssimazioni, come ad esempio nella descrizione delle proprietà dei materiali. Tali semplificazioni possono condurre ad errori e differenze significative tra i processi simulati e i risultati reali. Ciò nonostante in letteratura non si trovano pubblicazioni o articoli che analizzano l'accuratezza dei modelli numerici confrontando i risultati da essi proposti con misurazioni sperimentali di reali trattamenti termici ad induzione.

Questa Tesi di Laurea pertanto affronta inizialmente uno studio tramite software agli elementi finiti sull'influenza dei parametri di macchina (frequenza, dimensioni dell'induttore e presenza di un concentratore di flusso posto sopra e sotto la ruota) nell'ottenere uno strato temprato omogeneo nel

dente e nella cava di una ruota dentata temprata ad induzione, evitando l'austenitizzazione di tutto il dente. In particolare si suppone che l'uso del concentratore di flusso abbia un ruolo chiave nella riduzione dell' effetto di bordo.

Successivamente è stato proposto un confronto tra i risultati di misure sperimentali di temperatura su un processo di tempra e i risultati delle simulazioni numeriche dello stesso processo. Per le misure sperimentali si è scelto di utilizzare speciali vernici termiche che tendono a trasformarsi visibilmente al raggiungimento di una determinata temperatura. Filmando il processo di tempra con una telecamera ad alta velocità di acquisizione è stato possibile risalire all'evoluzione temporale delle isoterme a 816°C e 927°C. Sono stati proposti modelli con diverse approssimazioni delle proprietà dei materiali, allo scopo di capirne l'influenza sull'evoluzione delle isoterme. Inoltre è stato proposto anche un confronto tra l'effetto di bordo stimato dalle simulazioni e quello reale osservando la profondità dello strato temprato.

Parole chiave: Validazione, tempra ad induzione, modelli numerici, simulazioni, misurazioni sperimentali, isoterme, ruote dentate

1. Induction hardening

1.1 Introduction

Nowadays, induction heat treatment processes such as induction hardening are increasingly used in automotive and aeronautics to improve the service performances such as fatigue life, resistance at usury and plastic deformation of various mechanical components.
Induction hardening is a reliable and time-saving process, as it takes few seconds to take place, due to higher specific power of the process. Moreover heating can be localized to the specific areas where metallurgical changes are desired (e.g., flank, root and gear tip can be selectively hardened) and the heating effect on adjacent areas is minimum.
Last but not least, an induction system improves working conditions for employees and reduces pollution by eliminating smoke, waste heat, noxious emissions and loud noise. Heating is safe and efficient with no open flame to endanger the operator or obscure the process.

1.2 The electromagnetic problem

1.2.1 Theoretical background

In electrical engineering practice, the simulation of devices, measuring arrangements and various electrical equipments is based on Maxwell's equations coupled with the constitutive relations.
The Maxwell equations are the set of four fundamental equations governing electromagnetism, which can be used in the frame of any numerical field analysis tool, e.g. in the finite element method.
The field quantities are depending on space r and on time t, therefore in the following, a shorter notation will be used. For example we have that magnetic field intensity $\vec{H} = \vec{H}(\vec{r}, t)$.
These equations, written in differential vector form, are:

1. $\nabla \cdot \vec{B} = 0$
2. $\nabla \cdot \vec{D} = \rho$

3. $\nabla \times \vec{E} = -\frac{\partial \vec{B}}{\partial t}$
4. $\nabla \times \vec{H} = \vec{J} + \frac{\partial \vec{D}}{\partial t}$

Where the first equation is the gauss's law for magnetism, that states that the divergence of the vector magnetic flux density $\vec{B}$ $[T]$ is equal to zero. In other words, $\vec{B}$ is a solenoidal vector field. Free magnetic charges do not exist physically and magnetic flux lines close upon themselves.

The second equation is the electric Gauss's law. It describes the relationship between an electric field and the electric charges that cause it. The source of electric field is the electric charge and electric flux lines start and close upon the charge. $\vec{D}$ $[C \cdot m^{-2}]$ is electric flux density, and ρ $[C \cdot m^{-3}]$ is the free electric charge density.

The third equation is called Faraday's law and demonstrates that each variation of magnetic flux density produces an electric field intensity $\vec{E}$ $[V \cdot m^{-1}]$.

The fourth and last equation is Ampère-Maxwell's law, that states that magnetic field intensity $\vec{H}$ $[A \cdot m^{-1}]$ can be generated by an electrical current ($\vec{J}$ $[A \cdot m^2]$ is the conduction current density) and by the so called displacement current in dielectric media, which is generated by a time-varying electric field.

In order to Maxwell's equations to be definite it is necessary to specify the constitutive relations of materials that are, for a linear, isotropic medium:

- $\vec{D} = \varepsilon \cdot \varepsilon_0 \cdot \vec{E}$
- $\vec{J} = \sigma \cdot \vec{E}$
- $\vec{B} = \mu_r \cdot \mu_0 \cdot \vec{H}$

Where ε is the relative permittivity of the material, μ_r is the magnetic permeability, and σ is the electric conductivity of the material. The constant $\mu_0 = 4 \cdot \pi \cdot 10^{-7}\ H/m$ is the permeability of vacuum and $\varepsilon_0 = 8.854 \cdot 10^{-12} F/m$ is the permittivity of free space
The Maxwell equations can be rearranged in the case of induction heating, in which frequencies remain below 10 MHz [4].

Indeed, in this case it is possible to neglect the terms $\frac{\partial \vec{D}}{\partial t} = \frac{\partial \varepsilon_0 \cdot \varepsilon \cdot \vec{E}}{\partial t}$ on the Ampere-Maxwell equation that becomes

1) $\nabla \times \vec{H} = \sigma \cdot \vec{E}$

Moreover, after some vector algebra and by replacing the latter constitutive equation in the third Maxwell law, we obtain

2) $\nabla \times \left(\frac{1}{\mu_r} \nabla \times \vec{\mathrm{E}}\right) = -\mu_0 \cdot \sigma \frac{\partial \vec{\mathrm{E}}}{\partial \mathrm{t}}$

The Faraday's law can also be expressed remembering that $\vec{B}$ is solenoidal and hence we can write $\vec{B} = \nabla \times \vec{A}$, where $\vec{A}$ is the magnetic vector potential. We have

3) $\nabla \times \vec{E} = -\frac{\partial \nabla \times \vec{A}}{\partial t} = -\nabla \times (\frac{\partial A}{\partial t})$

That integrated gives

4) $\vec{E} = -\frac{\partial \vec{A}}{\partial t} - \nabla \varphi$

Where φ is the electric scalar potential. By multiplying 4) for σ, we have

5) $\vec{J} = -\sigma \frac{\partial \vec{A}}{\partial t} + \vec{J}_0$

Where $\vec{J}_0 = -\sigma \nabla \varphi$ is the source current density in the induction coil. 5) states that the total current density is given by eddy currents and the current imposed in the inductor.

By replacing the second constitutive equation and 3) in 2), neglecting the hysteresis and magnetic saturation we have

$$\nabla \times \left(-\nabla \times \frac{\partial \vec{\mathrm{A}}}{\partial \mathrm{t}}\right) = \mu_0 \cdot \mu_r \cdot \frac{\partial \vec{\mathrm{J}}}{\partial \mathrm{t}}$$

And hence

$$\frac{1}{\mu_r \cdot \mu_0} \cdot \nabla \times \left(\nabla \times \vec{\mathrm{A}}\right) = \vec{\mathrm{J}}$$

That, remembering the equation 5), becomes

6) $\frac{1}{\mu_r \cdot \mu_0} \cdot \nabla \times \left(\nabla \times \vec{\mathrm{A}}\right) = -\sigma \frac{\partial \vec{A}}{\partial t} + \overrightarrow{J_0} = -j\omega\sigma\vec{A} + \overrightarrow{J_o}$

Where ω is the angular frequency. Equation 6) is the potential vector formulation.

For the great majority of induction heating processes such as hardening a heat effect due to hysteresis losses does not exceed 7% compared to the heat effect due to eddy current losses [4]. So in these case neglecting hysteresis is quite valid.

One of the major difficulties in electromagnetic field and heat transfer computation is the nonlinearity of material properties, as clarified subsequently. So, using simple analytical methods that cannot take into account the variation of these properties could lead to unpredictable and erroneous results. Moreover, the geometries of the coil and the workpiece are often very complex. For these reasons, modern induction heat treatment specialists turns to highly effective numerical

methods such as finite element method, that are widely and successfully used in the computation of electromagnetic and heat transfer problems in heat treatment.

1.2.2 Basics electromagnetic phenomena in induction heating

Induction heating is the process of heating an electrically conducting object by electromagnetic induction, where eddy currents (also called Foucault currents) are generated within the material by electromagnetic forces, according to the third Maxwell's equation, and resistance leads to Joule heating of the metal.

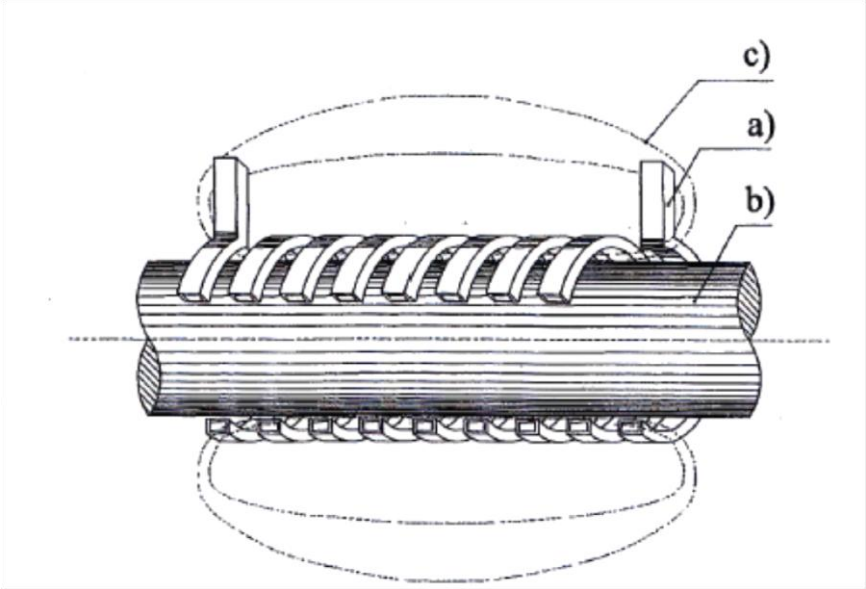

Fig. 1.1 Simple scheme of induction heating process: a) coil, b) load, c) magnetic field lines

By several electromagnetic effects such as skin effect, proximity effect and ring effect current distribution in the coil and in the load is not uniform.

1.2.2.1 Skin effect

Skin effect is the tendency of an alternating electric current to become distributed within a conductor such that the current density is largest near the surface of the conductor, and decreases with greater depths in the conductor, following the formula:

$$G = G_0 \cdot e^{-\frac{x}{\delta}}$$

Where G_0 is the current density at the surface and δ is called skin depth. Skin depth is defined as the depth below the surface of the conductor at which the current density has fallen to 1/e of G_0. In normal cases it is well approximated as:

$$\delta = \sqrt{\frac{2 \cdot \rho}{\omega \cdot \mu_r \cdot \mu_0}}$$

Where ρ is the resistivity of the conductor, ω is the angular frequency of current and μ_r is the relative magnetic permeability of the conductor. Approximately 86 % of the power will be concentrated in the first penetration depth.

It is necessary to mention that penetration depth is not constant during the induction heating process. Indeed the value of relative magnetic permeability has a nonconstant distribution within the workpiece and moreover it changes with the temperature of the material and the magnetic field.

The skin effect causes the effective resistance of the conductor to increase at higher frequencies, where the skin depth is smaller, thus reducing the effective cross-section of the conductor. The skin effect is due to opposing eddy currents induced by the changing magnetic field resulting from the alternating current.

Power distribution, related to current density, follows the law:

$$w = \rho \cdot G^2 = w_0 \cdot e^{-\frac{2 \cdot x}{\delta}}$$

Where w is the power density in the sample and w_0 is the power density at the surface.

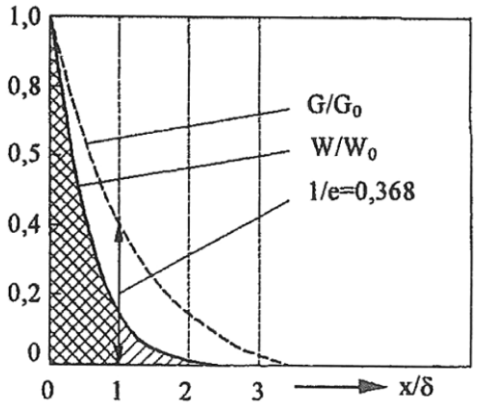

Fig. 1.2 Current and power density distribution in a square sample heated by induction.

1.2.2.2 Electromagnetic proximity effect

A changing magnetic field will influence the distribution of an electric current flowing within an electrical conductor, by electromagnetic induction. When an alternating current flows through an isolated conductor, it creates an associated alternating magnetic field around it. The alternating magnetic field induces eddy currents in adjacent conductors, altering the overall distribution of current flowing through them. The result is that the current is concentrated in the areas of the conductor furthest away from nearby conductors carrying current in the same direction. Current distribution is concentrated on the neighbor side of conductors if they are carrying current in the opposite direction.

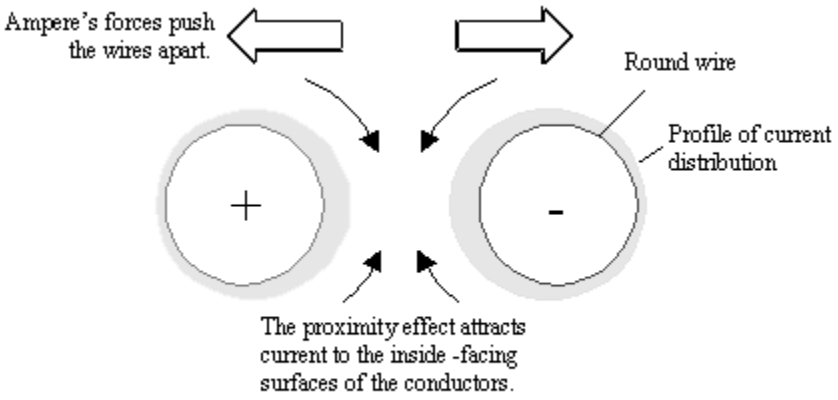

Fig. 1.3 proximity effect

1.2.2.3 Electromagnetic ring effect

Up to now we discussed current density distribution in straight conductors. If a conductor is bent to shape it into a ring, then its current will be redistributed as shown in figure 1.4.

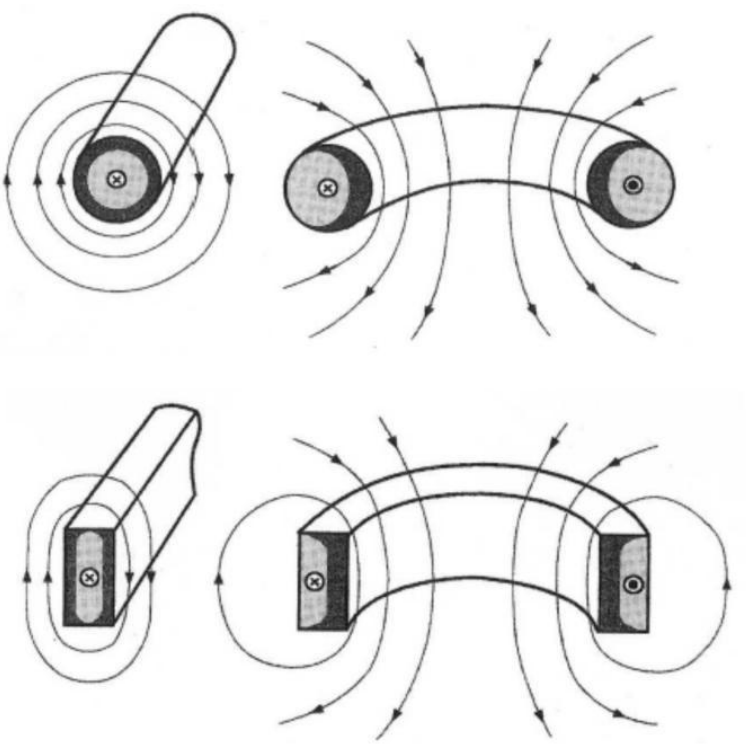

Fig. 1.4 ring effect.

Magnetic flux lines will be concentrated inside the ring and therefore the density of the magnetic field will be higher inside the ring. As a result, the majority of the current will flow within the thin inside surface layer of the ring.

The presence of ring effect can have a positive effect in induction heating of cylinder for example. Indeed, where the workpiece is located inside the induction coil, the combination of ring effect and skin and proximity effects will leads to a concentration of the coil current on the inside diameter of the coil. As a result, there will be close coil-workpiece coupling, which leads to good coil efficiency.

1.3 The thermal problem

In the design of a induction heating system it is very important to know precisely heating time and power necessary to obtain a determined temperature's profile needed for the process.
Moreover, due to the consideration explained in previous chapter, a typical specific power distribution of an induction heating process is not constant. For these reasons we need to know the thermal transient in the workpiece.

All the three heating transfer methods are important for induction heating processes: so it is useful to describe equations that settle thermal balance.

1.3.1 Conduction

The heat generated by the induced currents in the workpiece flows by conduction from hot regions to cold heart of the piece. The basic law which describes the transfer of heat by conduction is Fourier's law.

$$q_{cond} = -k \cdot grad(T)$$

Where q_{cond} is the heat flux by conduction $[W \cdot m^{-2}]$, k is thermal conductivity $[\frac{W}{m \cdot K}]$ and T is temperature [K]. According to Fourier's law, the greater is the temperature's difference between the surface and the core, the greater is q_{cond}.

1.3.2 Convection

During the induction heat treatment, part of the heat generated is lost toward the surrounding environment by convection. Convection is carried out by fluid and Newton's law states that the rate of convective heat transfer is directly proportional to the difference between the surface temperature of the workpiece and the fluid surrounding it.

$$q_{conv} = \alpha(T_s - T_f)$$

Where q_{conv} is the density of heat lost by convection $[W \cdot m^{-2}]$, α is the coefficient of heat loss by convection $[\frac{W}{m^2 \cdot K}]$, Ts is the surface temperature [K] of the workpiece and T_f is the temperature of the fluid of the environment [K].

The coefficient of heat loss by convection α depends on the thermal properties of the material and part of the surrounding fluid , the inductor, the viscosity of the fluid and the speed of rotation of the workpiece during heating. In fact, convection is considered forced regime and not free because the parts are rotated or displaced during heating. In practice we will use the so called differential curves of speed quenching in order to describe the quenching phase.

1.3.3 Irradiance

Heat transfer by radiation is explained as a propagation phenomenon of electromagnetic energy caused by the temperature difference between two bodies. This phenomenon is governed by the Stefan-Boltzmann law

$$q_{rad} = \sigma_s \cdot \varepsilon \cdot (T_s^4 - T_f^4)$$

Where q_{rad} is the density of heat lost by radiation $[\frac{W}{m^2}]$ and σ_s is the Stefan-Boltzmann coefficient. ε is the emissivity, that takes into account the differences between the real case and the ideal case (black body), in which the emissivity is equal to 1. Emissivity depends on the temperature and the surface shape factor.

T_s and T_f are respectively the surface temperature of the workpiece and the temperature of the surrounding fluid [K].

Equations can be rearranged as follows:

Chart 1.1 *Equations of thermal balance*

Interested zone	Phase of the process	Equations
internal	Heating	$\rho \cdot c \cdot \frac{dT}{dt} = \lambda \cdot \nabla^2 T + Q_{ind}$
surface		$\rho \cdot c \cdot \frac{dT}{dt} = \lambda \cdot \nabla^2 T + Q_{ind} + S\sigma\varepsilon \cdot (T^4 - T_{aria}) + S\alpha \cdot (T - T_{aria})$
Internal	hardening	$\rho \cdot c \cdot \frac{dT}{dt} = \lambda \cdot \nabla^2 T$
surface		$\rho \cdot c \cdot \frac{dT}{dt} = \lambda \cdot \nabla^2 T + S\alpha \cdot (T_{acqua} - T)$

Stefan-Boltzmann and Newton's laws are very useful to estimate the average loss by convection and radiation. At low temperatures the contribution of losses by convection predominates losses by radiation; the situation is reversed at high temperatures.

1.4 Material's properties

1.4.1 Electrical properties

The electromagnetic properties more involved in induction hardening processes are relative magnetic permeability μ_r and electrical conductivity.

1.4.1.1 Electrical conductivity

The electrical conductivity (σ) expressed in Siemens per meter $\left[\frac{S}{m}\right]$ measures the capacity of a material to conduct an electrical current. Generally, metallic materials are considered good electrical conductors compared to insulating materials.
This electrical property corresponds to the inverse of the electrical resistivity and it depends on the temperature. Conductivity trend as function on temperature can be approximated as linear, according to the relation:

$$\sigma = \sigma(T) = \frac{1}{\rho_0 \cdot (1 + \alpha_0 \cdot T)}$$

In which ρ_0 is the resistivity of the material at 0 ° C, while α_0 is a coefficient to increase the resistivity with temperature.

However, this approximation may differ from the actual behavior. For example, in carbon steel one can observe that conductivity varies in a nonlinear way, decreasing approximately five times in the range 0-800 ° C, while at 1200-1300 ° C it is approximately seven times less than the one measured at room temperature.

1.4.1.2 Relative magnetic permeability

The relative magnetic permeability μ_r indicates the capacity of the material to conduct a magnetic flow compared to vacuum and it is a complex function of the magnetic field and temperature.
While in non magnetic materials μ_r is equal to 1, in magnetic material it starts from the value of the permeability at 20 ° C (μ_{20}), varies a little increasing temperature, and collapses to unit value reaching the Curie temperature of the material, becoming diamagnetic.

1.4.2 Thermal properties

Thermal properties involved in induction hardening processes are thermal conductivity and specific heat.

1.4.2.1 Thermal conductivity

Thermal conductivity defines the rate at which a heat flow is transmitted by conduction in the materials in function of time.
In the case of induction hardening of gears we have to remember that steel has rather high thermal conductivity, so heat generated in a thin region in the surface is rapidly transferred to the cold heart of the piece and hence, it becomes difficult to control heat generated in the surface. This especially applies to the root of the gear.
Thermal conductivity is function of temperature and heating rate.

1.4.2.2 Specific heat

The specific heat corresponds to the amount of heat required to increase of 1°C the mass unit, kg. This property is also a complex function of temperature and heating rate.
Specific heat of steel increases linearly with temperature until the temperature of the beginning of austenitization (Ac1). After that it reaches rapidly the peak of 1600 $\frac{J}{kg \cdot °C}$ at a temperature between Ac1 and Ac3, and then it decreases drastically before reaching Ac3. This behavior is due to the latent heat of phase transformation.

1.5 Metallurgical analysis of martensitic hardening

1.5.1 Austenitization and hardening

The austenitizing process is an extremely delicate phase in the process of induction hardening.

Typically, in the through hardening by conventional heaters, it is possible to determine the austenitizing temperature by the proper iron-carbon diagram. Usually alloying elements extend the field of existence of ferritic or austenitic region.

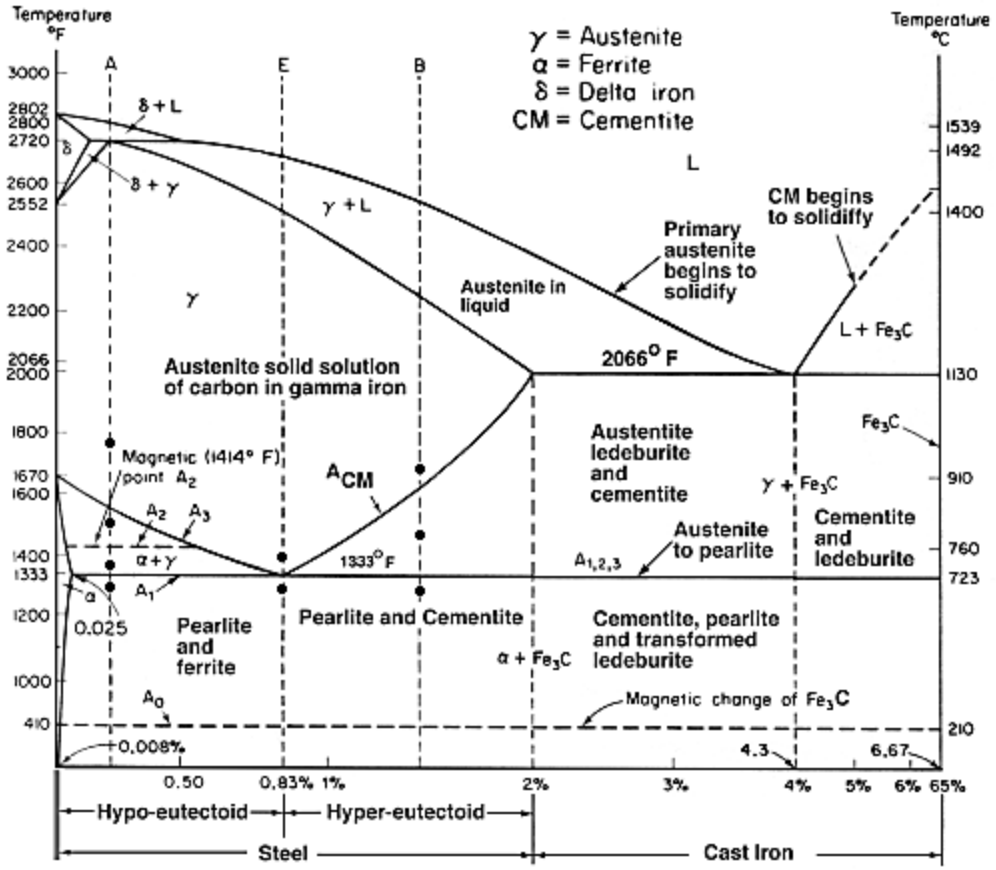

Fig. 1.5 Iron-carbon diagram

Austenitization can be partial, if it reaches a temperature between AC1 and AC3, or total if the temperature is higher than AC3.

Unfortunately surface induction hardening process is much more complex. Indeed, iron-carbon diagram is calculated in equilibrium condition, or for a slow process, and on the contrary, austenitization is very fast and it lasts a maximum of few seconds.

Propagation of atoms in crystals is not instantaneous, due to the rigidity of the crystalline metallic state. This thermal "inertia" causes a shift in the structure of the iron-carbon diagram in fast heating processes such as hardening.

For this reason, in order to properly austenitize the steel, it is necessary to reach higher temperatures than those predicted the Fe-C diagram, to provide enough driving-force to the process. Indeed the high heating rates and short austenitization times that are realized in induction heating

treatments affect the microstructure of the austenite immediately prior to quenching.

Choosing the proper treatment temperature is possible by using CHT diagrams, or "Continuous-Heating-Transformation".

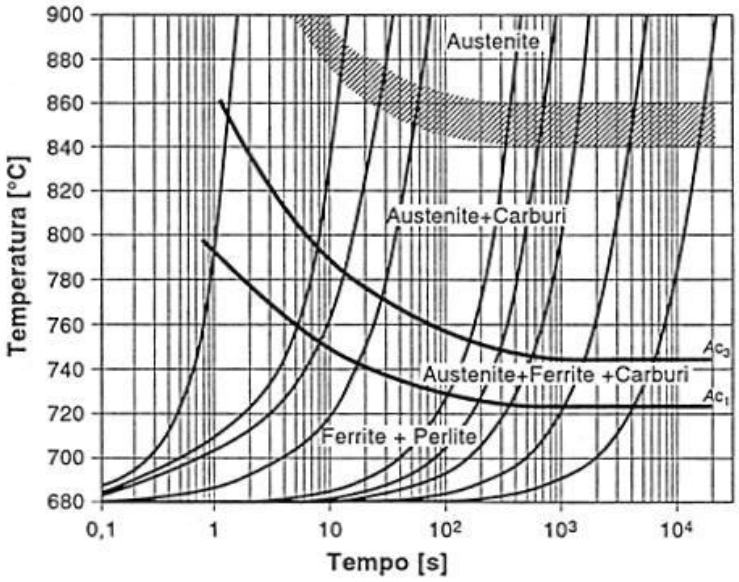

Fig. 1.6 CHT diagram for C60 steel

In determination of austenitizing temperature the prior metallurgical structure is also very important. Indeed the more ε cementite carbides are dispersed, the lower is the temperature necessary to obtain homogeneous austenite.

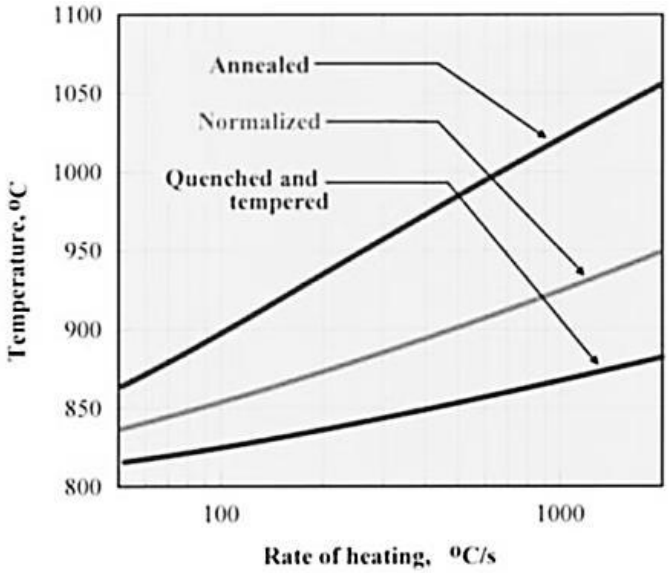

Fig. 1.7 Influence of prior microstructure on starting austenitization temperature

When discussing induction hardening, it is imperative to mention the importance of having "favourable" material conditions prior to gear treatment. Hardness repeatability and the stability of the hardness pattern are grossly affected by the consistency of the microstructure prior to heat treatment and the steel's chemical composition.

A good initial microstructure, comprising a homogeneous fine-grained quenched and tempered structure leads to fast and consistent response to induction heat treating, with the smallest shape/size distortion and a minimum amount of grain growth. This type of prior microstructure results in higher hardness and deeper hardened case depth compared to a ferritic/pearlitic initial microstructure.

Having a good microstructure improves also mechanical characteristics of the core, especially fatigue resistance.

Longer heat time and higher temperature of austenitization leads to grain growth, the appearance of coarse martensite, data scatter, an extended transition zone, and gear shape distortion. Coarse martensite has a negative effect on tooth toughness and creates favourable conditions for crack development.

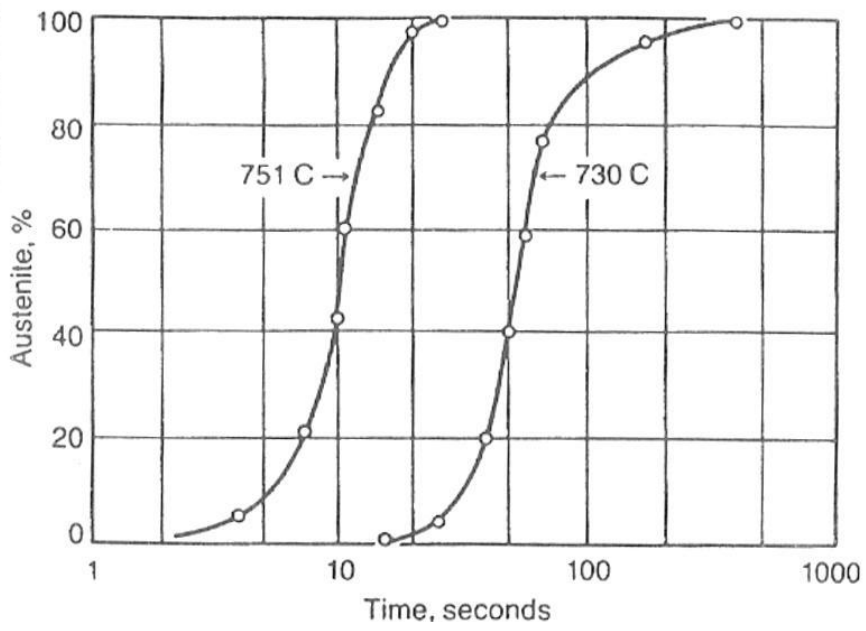

Fig. 1.8 *Influence of temperature on the kinetics of austenitization*

After austenitization the real hardening process takes place. Martensite transformation is realized on rapid cooling of steel. The minimum cooling rate at which the martensite is formed is called the lower critical rate of cooling, while the rate at which transformation by the pearlite and bainite

mechanism are suppressed completely is referred to as the upper critical rate of cooling or quenching. The upper critical rate of cooling can be determined through CCT diagrams (Continuous-Cooling-Transformation).

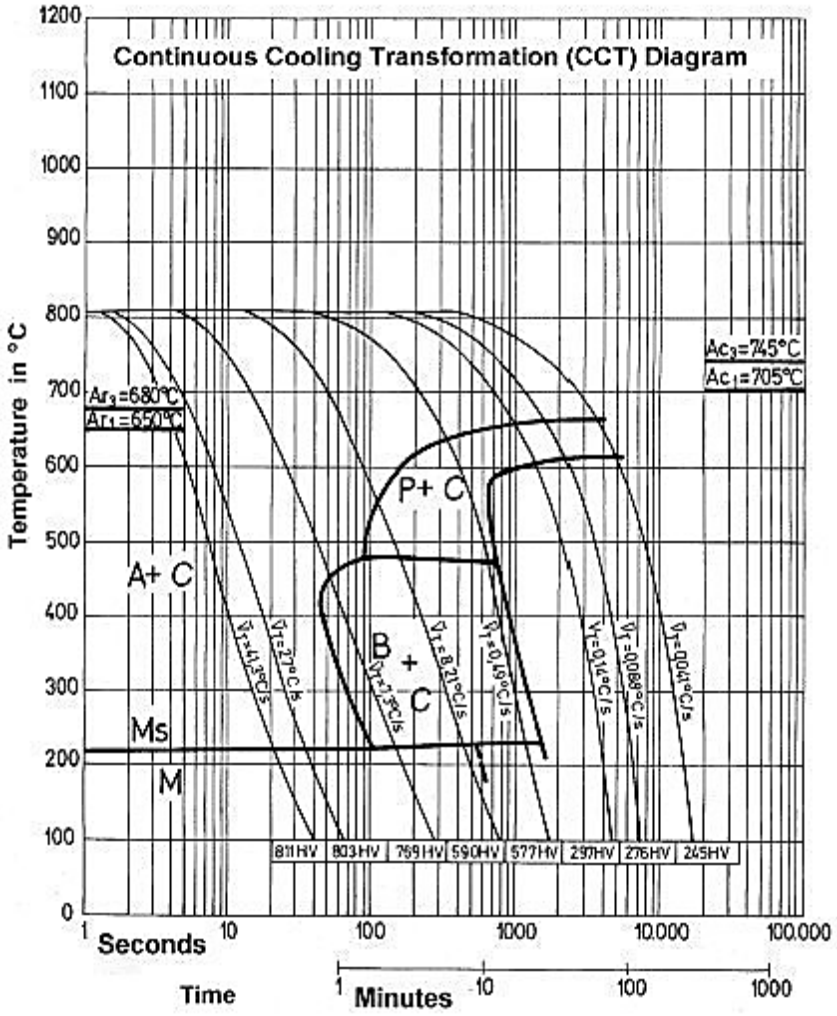

Fig. 1.9 CCT diagrams

1.5.2 Quenching

The main purpose of the quench, however applied, is to remove the heat from the part as rapidly as possible while minimizing any stresses that may occur in the process.

We consider for the moment that quenching is done by soaking the workpiece in a liquid bath without agitation, immediately after induction heating.

Cooling rate is not constant but varies as a function of the surface temperature of the workpiece.

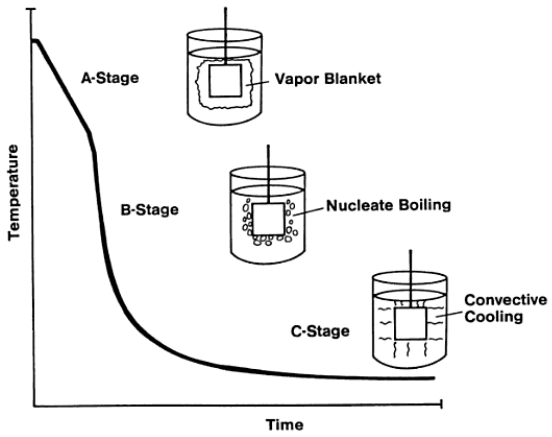

Fig. 1.10 *The three stages of cooling*

The three stages of the quenching process are:

1. Calefaction: in this stage a steam barrier is formed around the material, causing a minimal heat transfer and therefore a slower cooling. Indeed the coolant fluid is not in direct contact with the material. This behavior is called the Leidenfrost effect. It appears when the workpiece temperature is much higher than the liquid one.
2. Boiling: decreasing workpiece's temperature, the film of steam gradually decreases in thickness until the fluid touches it's hot surface. In this stage heat transfer is maximum.
3. Convection: The temperature of the surface of the workpiece falls below the liquid's saturation temperature, ending the boiling's stage. Heat transfer is smaller.

Nevertheless, this subdivision represent just a qualitative information about quenching phenomena, because of the multitude of factors involved. For example, especially for induction hardening, quenching speed is not the same throughout the material, and a big amount of heat flows towards the cold heart of the piece.

Quenching phase determines the final properties of the treated material and it is critical for residual stresses distribution during the process. So it is necessary to take into account some criteria in choosing the coolant fluid:

- The length of the film-boiling phase must be sufficiently short so that the steel can be hardened and not so long so that the cooling process would extend into the ferrite-pearlite transformation region of the steel.
- The cooling rate value must be sufficiently high through the nose of the ferrite-pearlite transformation region, which is typically approximately 500-600 °C for many steels, to minimize the potential formation of these transformation product.

- The nucleate boiling to convective cooling transformation temperature should be as low as possible to achieve maximum hardening potential.
- In the convective region, cooling should be sufficiently low in order to avoid distortion and /or cracking. Quench cracking is caused by the formation of stresses within the part due to the normal contraction of the metal as it is cooled. In addition, microstructural stresses also occur as the steel expands with the formation of martensite.

The quenching media in general use are :

- **Water:** it is probably the most widely quenchant fluid used as it is simple and effective. Cold water is one of the most severe of the quenchants, and rapid agitation allows it to approach the maximum capabilities of the liquid quenchants. It cools at the rate of 982°C per second. It tends, however, to form bubbles on the surface of the metal being quenched and causes soft spots. Furthermore, cooling rate in martensitic transformation region is very high, causing the formation of cracks and distortions, so a brine solution is often used to prevent this trouble.

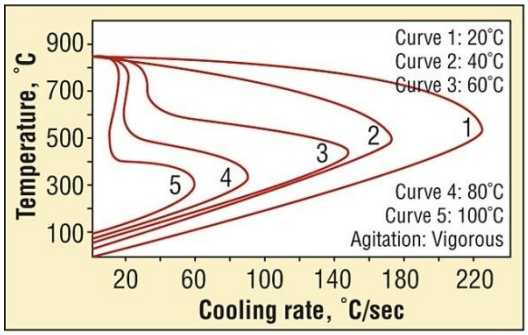

Fig. 1.11 Effect of temperature on quenching properties of water

- **Brine:** Brine cooling rates are the most rapid of all the quenchants. While steam breakdown is extremely rapid, higher cooling rates may increase the possibility of distortion, and quench cracking of the part may occur. Brine quenching can eliminate soft spots where the part geometry permits rapid quenching. This rapid quenching action is caused by minute salt crystals that are deposited on the surface of the work. Localized high temperatures cause the crystals to fragment violently, creating turbulence that destroys the vapor phase. A 10% solution of NaCl is usually an effective quench. The relationship of brine concentration to hardness is shown in figure 1.12. Number above curve indicates distance from quenched end in units of 1/16 inch. Small variations in quench temperature will not greatly affect the

cooling rate of the system. A temperature of 20˚C assures maximum effectiveness of cooling.

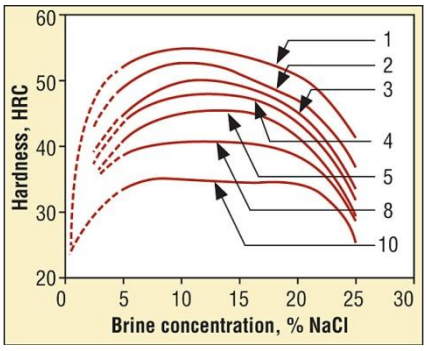

Fig. 1.12 Relation of hardness to brine concentration in 90˚C brine solutions.

- **Oils:** Oils are characterized by quenching speed and operating temperature among other factors. Oils range from normal speed for quenching high-hardenability steels to high speed for steels with low hardenability. A major factor in selection of oils is the flash point, or temperature at which the oil vapors will ignite if an ignition source is present. Ignition occurs if the part is not quenched rapidly or if the oil does not remove heat fast enough. Rapid agitation of the oil and adequate quenchant cooling are necessary to reduce the possibility of fire.

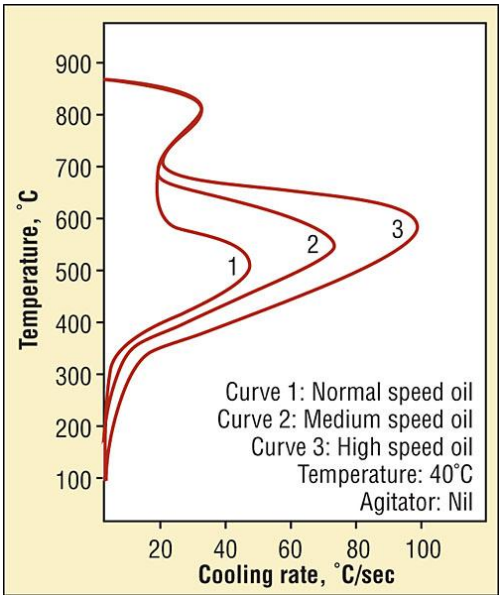

Fig. 1.13 Cooling rate curves for quenching oils

- **Polymers:** Polymer quenchants are materials that are added to water to simulate the quenching characteristics of oil. This is obtained by varying the concentration of the polymer in the water. Benefits of this system include the elimination of smoke as well as possible hazard of ignition and fire. The polymer helps to develop a film at the interface of the heated material and the quenchant and acts as an insulator to slow down the cooling rate

to approach that of oil. This film eventually collapses, and the quenchant comes in contact with the part being processed. This results in nucleate boiling and a high heat-extraction rate. The balance of the cooling is due to convection and conduction in the liquid. The polymer film on the surface of the heated area dissolves into the fluid when the surface temperature of the part falls below the separation temperature of the polymer quenchant. A range of quench characteristics can be achieved through variations in the concentration of the polymer, quenchant temperature and its agitation.

Nevertheless, drop quenching is not the unique method used after induction heating. Indeed spray quenching is the most common form of application; the quenchant is applied to the part at the completion of the heating cycle by a ring or head with perforations, through which quenchant is passed directly onto the part. With this technique there are several advantages, such as the possibility to regulate the flow and the almost total elimination of the vapor phase, that allows to increase the drastic nature of the cooling and the consequent increase of hardness and favorable compressive residual stress values on the profile.

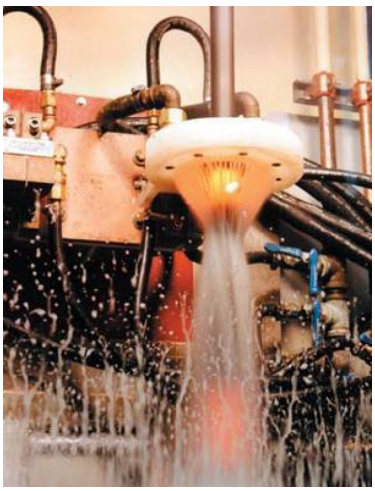

Fig. 1.14 spray quenching

1.5.3 Retained austenite

In practice, it is very difficult to have completely martensitic structure by hardening treatment. Some amount of austenite is generally present in the hardened steel. This austenite existing along with martensite is referred to as retained austenite. The presence of retained austenite greatly reduces mechanical properties and such steels do not develop maximum hardness even after cooling at rates higher than the critical cooling rate.

Fig. 1.15 Retained austenite (white) trapped between martensite needles (black) (x 1000).

There are many factors that could cause austenite to be retained:

During transformation from austenite, in order for martensite to form, the temperature must past through Ms (martensite start) and Mf (martensite finish), according to CCT diagram.

The first factor is the steel's carbon contents: as the concentration of carbon increases, both temperatures of Ms and Mf will be lowered. It may happen that the room temperature is between them and the resulting microstructure consists of martensite + metastable austenite, that should be transformed into lower bainite, but since the diffusion of carbon at 20 ° C is extremely low, this austenite remains in the structure.

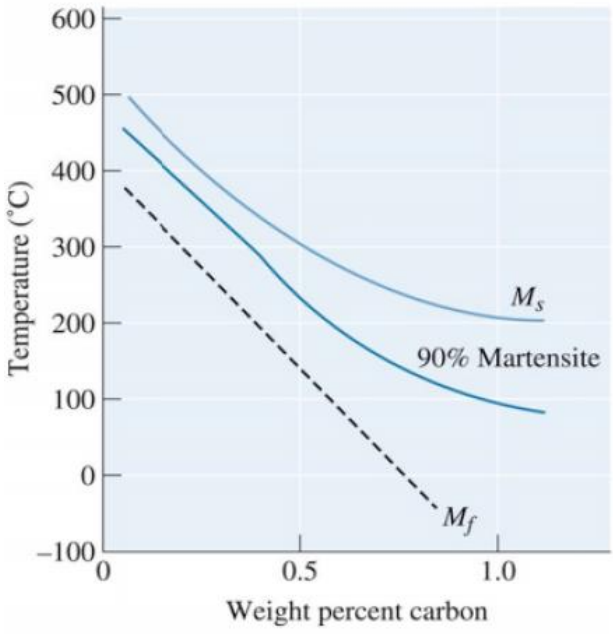

Fig. 1.16 Increasing carbon reduces the Ms and Mf temperature

Another cause is that almost all alloying substitutional elements lower Ms temp, except for some, such as aluminium and cobalt, causing the same phenomena.

Usually the higher is austenitization temperature, the greater is the amount of residual austenite. This is due to the austenite behavior to become more stable when increasing the amount of alloying elements and hence the amount of carbides solubilized during austenitizing process.

In order to avoid the presence of retained austenite a second cooling process at temperatures below 0 ° C is carried out. Retained austenite is converted into martensite by this treatment and this conversion results in increased hardness, wear resistance and dimensional stability of steel.

This treatment is employed for high carbon and high alloy steels used for making tools, bearings, measuring gauges and components requiring high impact and fatigue strength coupled with dimensional stability-case hardened steels.

The process consist of cooling steel to sub-zero temperature which should be lower than Mf temperature of the steel. Mf temperature for most steels lie between -30°C and -70°C. During the process, a considerable amount of internal stresses are developed in the steel, and hence tempering is done immediately after the treatment. This treatment also helps to temper martensite which is formed by decomposition of retained austenite during subzero treatment.

Mechanical refrigeration units, dry ice, and some liquefied gases such as liquid nitrogen can be used for cooling steels to sub-zero temperature.

1.5.4 Tempering

After the hardening treatment is applied, steel is often harder than needed and is too brittle for most practical uses. Also, severe internal stresses are set up during the rapid cooling from the hardening temperature.

The tempering process takes place after steel is hardened, but it is not less important in metal heat treatment. Tempering temperatures are usually below the lower transformation temperature and their main purposes are to increase the toughness of steel, to yield strength and ductility, to relieve internal stresses, to improve homogenization, and to eliminate brittleness. After holding the workpiece at the right temperature for the required length of time, an air cooling process usually follows.

In other words, because of tempering it is possible to improve the mechanical properties of the workpiece, to reduce the stresses caused by the previous heat treatment stage and the chance of distortion and possibility of cracking without losing too much of the achieved hardness.

During tempering carbon begins to spread and tetragonal martensite transforms to cubic ferrite. But being the temperature too low to ensure a significant diffusion of carbon, it remains in the ferrite, generating nuclei of carbides $\varepsilon'(Fe_{2,4}C)$. This structure has a hardness similar to martensite's one, but greater toughness and it is called tempered martensite.

It is important that the time from quench to temper is held to a minimum. Otherwise the internal stresses may have enough time to allow shape distortion or cracking to take place, nullifying tempering benefits.

Retained austenite can be a serious problem. Martensite softens and becomes more ductile during tempering. After tempering, the retained austenite cools below the *M*s and *M*f temperatures and transforms to martensite, since the surrounding tempered martensite can deform. But now the steel contains more of the hard, brittle martensite. A second tempering step may be needed to eliminate the martensite formed from the retained austenite.

1.5.5 The hardened profile

The final distribution of the temperature is directly related to the hardness profile. Indeed, usually the hypothesis that all regions heated above the Ac3 temperature become hardened after quenching in water is done, neglecting that not every part of the gear may have different value of Ac3, due to the different heating rate.
Nevertheless the typical hardness profile is formed by four distinct parts, as shown in figure 1.17. The first is characterized by a maximum hardness, and the hardened depth is about 0.5 mm. In the second zone hardness falls rapidly to a minimum, for then rising to the value of initial hardness in the third part. The fourth and last part is not affected by the transformation during the metallurgical treatment.
According to figure 1.17, we can distinguish these zones by three depths: maximum hardness depth (d_{max}), the depth measured from the intersection between the curve and the initial hardness (d_{start}) and finally, the depth of the area affected by the induction heat treatment (d).

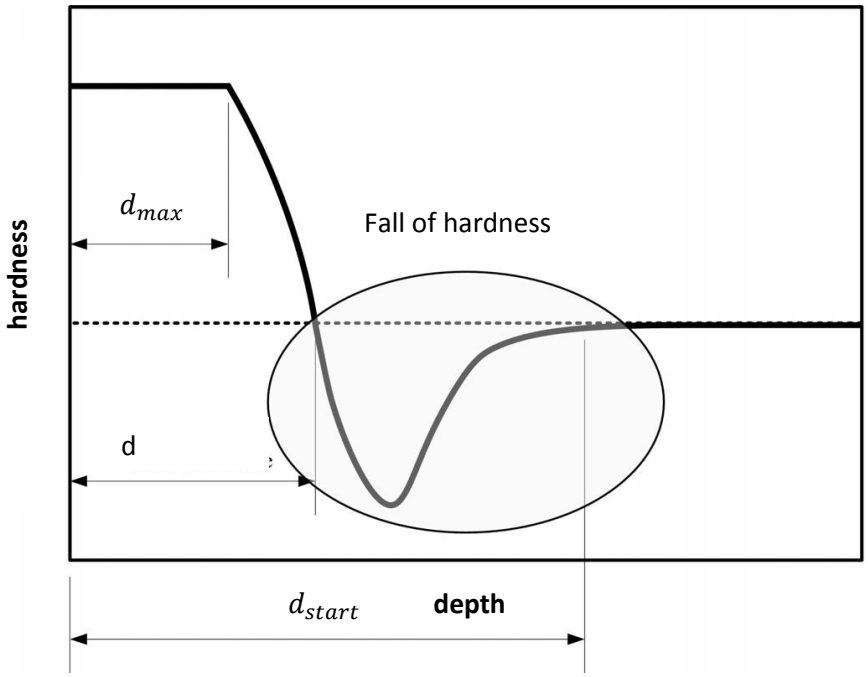

Fig. 1.17 typical hardness profile after induction hardening treatment

The third is a critical zone, because of the minimum hardness value which could affect the fatigue performance and the reliability of the workpiece. This is due to the self-tempering process that occurs to the region that exceeds the tempering temperature of the material.

This problem is not so relevant for stainless steel such as 4340, due to its good hardenability. It presents a martensitic structure also if air quenched and self-tempering zone is very limited.

The hardness profile is a specification of the design of the gear. Designers must take in account that the load is usually concentrated in the middle of the teeth, and that part of the root is overheated by the edge effect, as explained in the next chapters. An homogeneous microstructure is needed and compressive residual stresses would be favorable.

1.5.6 Residual stresses

Residual stresses are stresses that remain after the original cause of them (external forces, heat gradient) has been removed. They remain along a cross section of the component, even without the external cause.

Residual stresses occur for a variety of reasons, including inelastic deformations and heat treatment. It is important to remember that the residual stress system is self-equilibrating; that is, there is always a balance of stresses in the workpiece. If certain regions have compressive residual stresses,

then somewhere else there must be offsetting tensile stresses. If the stresses weren't balanced, "movement" would then result.

In general, two types of stress are encountered: thermal and phase transformation stresses.

- **Thermal stresses:** Thermal stresses are caused by temperature gradients between the surface and the core of the gear, due to the heating and cooling process. Considering the cooling process, the surface cools faster than the heart, leading to a faster contraction. This causes the surface to be tensioned, while the core becomes compressed. However, if deformation is elastic-linear, the situation is temporary because when all the components reach the same temperature deformation disappears.
- **Transformation stresses:** Transformation stresses primarily occur due to volumetric changes accompanying the formation of phases such as austenite, bainite, and martensite. Considering the quenching phase of an induction hardening process, being the heat removed from the surface, the martensitic transformation starts from the surface itself, while in depth transformation needs more time to occur. Having austenite and martensite different specific volumes, this causes the formation of stresses. These stresses will disappear once the workpiece reaches a homogeneous temperature, if they don't excess the threshold of elastic deformations.

The total stress is a combination of the two components.

It often happens that stresses exceed the yield strength threshold, leading to inhomogeneous plastic deformation within the piece. So residual stresses remain after the thermal equalization of the workpiece.

It is important to remember that the phase variation leads also to a variation of the mechanical properties, increasing the yield strength in the martensite.

It is possible to control the magnitude of residual stress by a careful study on the type and the quenching speed. Compressive residual stresses on the surface layers, especially in the root of the gear are desired. Indeed, they act as a prestress on the most strongly loaded surface layer, which increases the load capacity of the machine part and prevents crack formation or propagation on the surface. The machine parts treated in this way are suited for the most exacting thermomechanical loads since their susceptibility to material fatigue is lower. Consequently, much longer operation life of the parts can be expected.

Tensile residual stresses, on the other hand, can be dangerous. Having a maximum tensile stress located just beneath the hardened case facilitates the subsurface crack initiation.

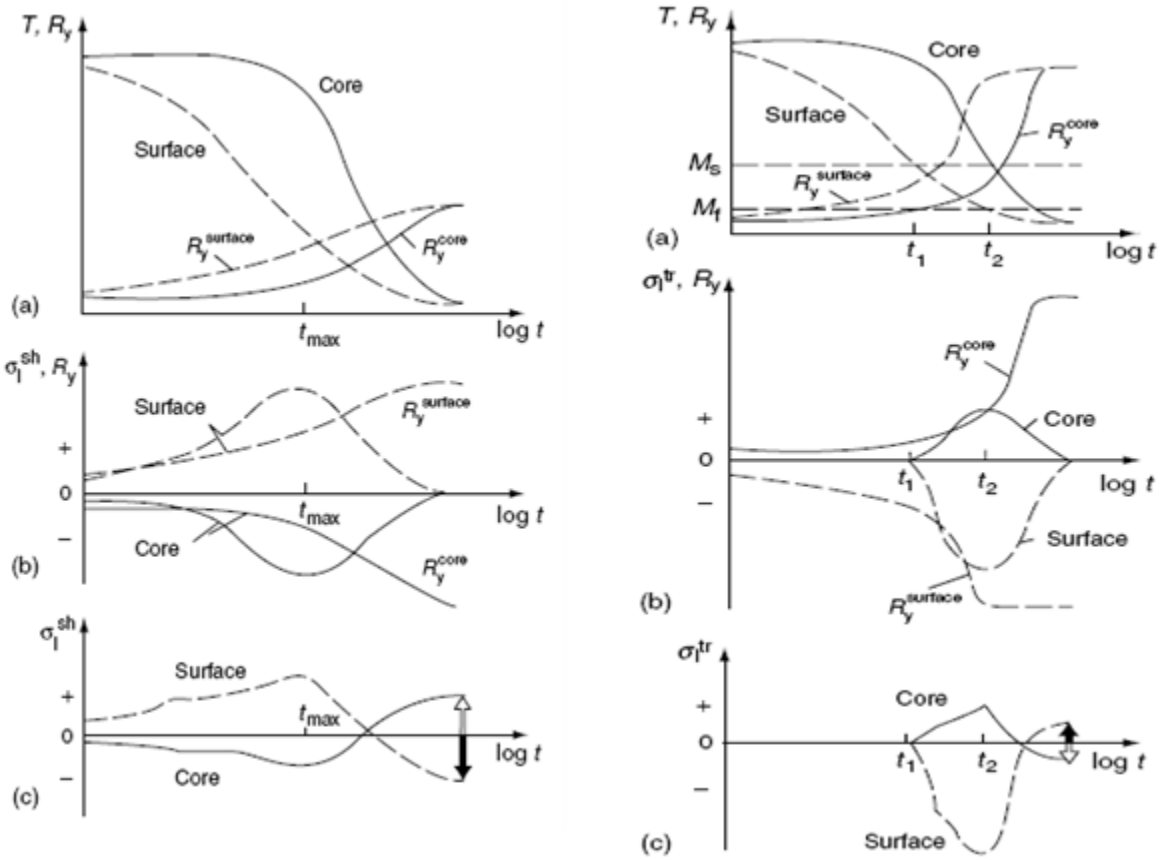

Fig. 1.18 Residual stresses for elasto-plastic material.

1.6 Power supplies for induction heat treatment

The complexity of induction hardening process is due to the large number of variables that influence it. For example, to achieve a specific case hardening pattern of a gear, it is necessary to have a device that provides the correct power/frequency/time combination. Depending on the desired result, it is possible to use a large range of frequencies, as shown in figure 1.19.

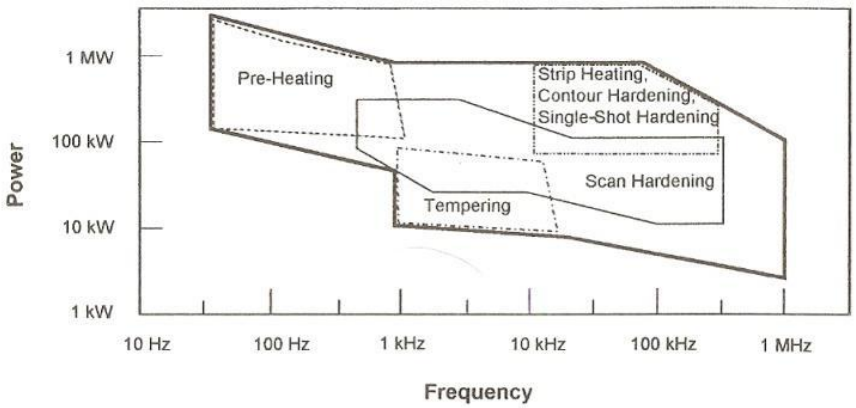

Fig. 1.19 Range of frequency utilized in induction heating

Frequency is a very important parameter in the design of induction heating power supplies because the power components must be rated for operation at the specified frequency. In particular, the power circuit must guarantee that these components are operated with a proper margin to yield high reliability at this frequency.

The coil geometry and the electrical properties of the material to be heated determine the coil voltage, current and power factor. Defining these parameters is necessary to ensure that the output of the power supply is capable of matching the requirements of the coil.

In general, an induction heating machine is composed of the power supply, the load matching and a process control system, as shown in a basic diagram in figure 1.20.

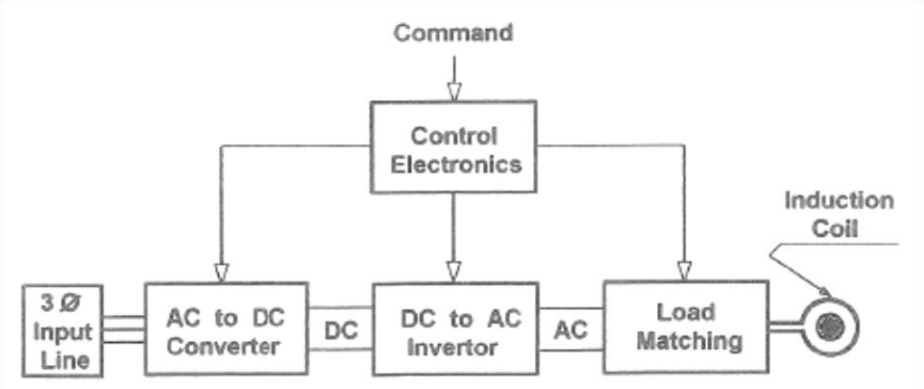

Fig. 1.20 Induction heat treatment power supply, basic block diagram

1.6.1 Power supplies

Induction heating power supplies convert the available line frequency power to the desired single phase power at the frequency required by the induction heating process.

Power supplies for induction hardening vary in power from a few kilowatts to hundreds of kilowatts, and in frequencies from 1 kHz to 400 kHz, including dual frequency units, dependent of the size of the component to be heated and the production method employed. Higher and lower frequencies are available but typically these will be used for specialist applications.

In the early days of induction heating, the motor-generator, a rotary-driven system composed of a motor coupled to a generator, was used extensively for the production of MF power up to 10 kHz, until the advent of solid state technology in the early 1970s.

Initially, solid state power supplies was limited to the use of thyristors for generating the MF range of frequencies using discrete electronic control systems. With this system, line voltage is converted

to direct current and then it is applied by means of a capacitive voltage divider to an SCR inverter circuit.

State of the art units now employ IGBT or MOSFET technologies for generating current as of MHz's order of magnitude.

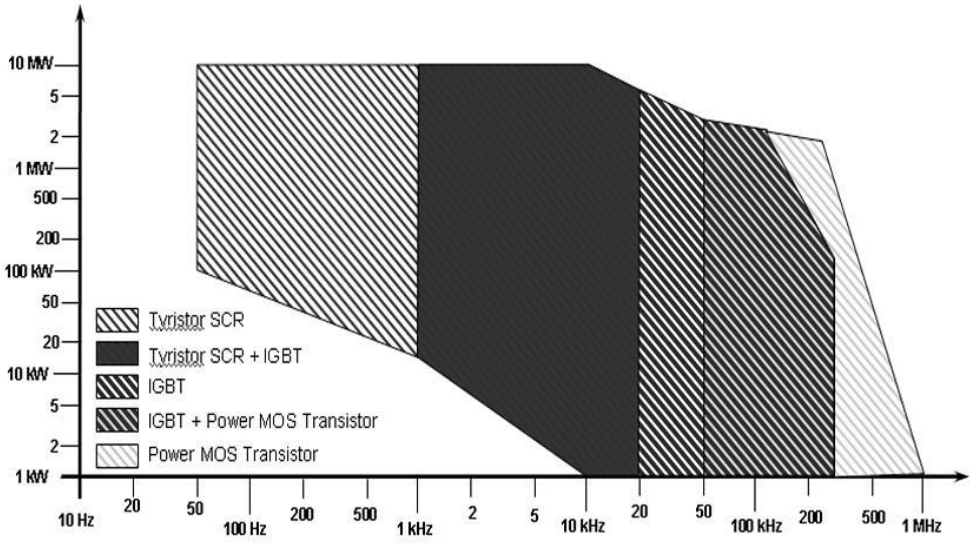

Fig. 1.21 switches utilized

A whole range of techniques are employed in the generation of MF and HF power using semiconductors.

Semiconductor switching devices may operate in Hard Switch Mode in various types of PWM (pulse width modulation) DC-DC converters and DC-AC inverter topology employed in a power system. In this mode, a specific current is turned on or off at a specific level of voltage whenever switching occurs. This process results in switching loss. The higher the frequency the more the switching loss, which obstructs efforts to raise the frequency. Switching loss can be calculated with the following formula:

$$P_{sw} = \frac{1}{2} V_{sw} \cdot I_{sw} \cdot f_s \cdot (t_{on} + t_{off})$$

Where P_{sw} is switching loss [W], V_{sw} is the switching voltage [V], I_{sw} is switching current [A], f_s switching frequency [Hz], t_{on} is the switch turn-on time [s] and t_{off} is the switch turn off time.

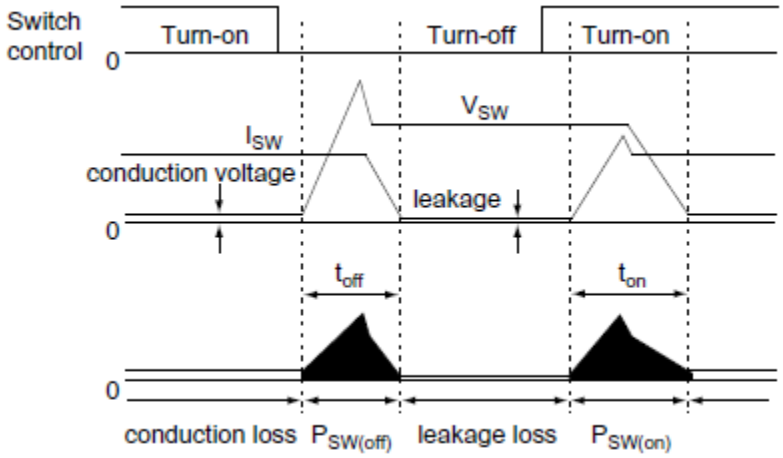

Fig. 1.22 wave form for a switching device

Switching also causes an EMI problem, because a large amount of di/dt and dv/dt is generated in the process.

Resonant converters, that operate in soft switching mode, offer an attractive solution to the problem of high switching losses at high frequency.

One of the major advantages of resonant converters is the absorption of the switching transistor capacitance and other parasitic components into the converter topology. However, the choice of using resonant converters rather than conventional switching converters should be based on the fact that the reduction in switching losses is greater than the increase in semiconductor device conduction losses due to the higher peak current or voltage in the resonant topologies.

A great variety of solutions have been proposed for power supplies in this rapidly evolving field, but all power units tend to feature four distinct elements: AC to DC rectifier, DC to AC inverter, output circuit and control system.

1.6.1.1 AC to DC rectifier

This portion of the power supply converts the line frequency alternating current input to direct current.

The simplest rectifier, the uncontrolled diode based rectifier, provides an output voltage (V_{DC}) related to the input line to line voltage (V_{AC}) following the formula

$$V_{DC} = 1.35\, V_{AC}$$

Since no control of the output is carried out by this rectifier, it must be used with an inverter section capable of regulating the power supply output.

The phase controlled rectifier has thyristor instead diode, that can be switched on in a manner that provides control of the DC output relative to the input line voltage. However, the control response time is slow and the input line power factor is not acceptable when the DC output voltage of the converter is less than a minimum, so schemes with additional power components are required.

Another solution is to have an uncontrolled rectifier followed by a switch mode regulator (buck) as shown in figure 1.23. This rectifier can therefore regulate the output power of the inverter by controlling the supply of direct current.

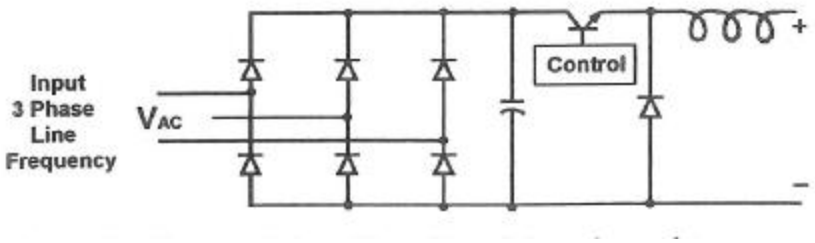

Fig. 1.23 Uncontrolled rectifier with switch mode regulator

In most heat treatment situations where the power supply rating is less than 600 kW, and where utility requirements do not require reduced harmonic content, a six pulse rectifier is acceptable. On the other hand a 12 pulse rectifier or a H bridge rectifier can be used.

1.6.1.2 DC to AC inverter

The inverter portion converts the DC supply to a single phase AC output at the relevant frequency. This features the SCR, IGBT or MOSFET and in most cases is configured as an H-bridge or an H-half bridge.

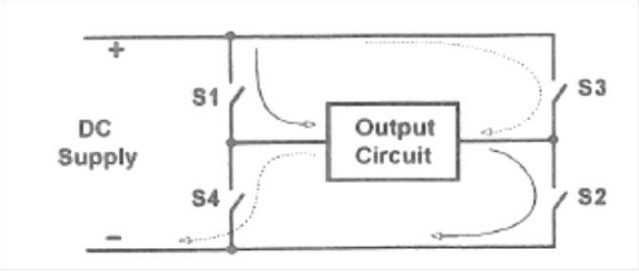

Fig. 1.24 basic full-bridge inverter

The H-bridge has four legs each with a switch and the output circuit is connected across the centre of the devices. When the relevant two switches are closed current flows through the load in one direction. These switches then open and the opposing two switches close, allowing current to flow in the opposite direction. By precisely timing the opening and closing of the switches, it is possible to sustain oscillations in the load circuit.

The 2 major types of inverter most commonly used in induction heating power supplies are the voltage-fed and the current-fed. Figure 1.25 shows the principal design features of the inverter involved in induction heating.

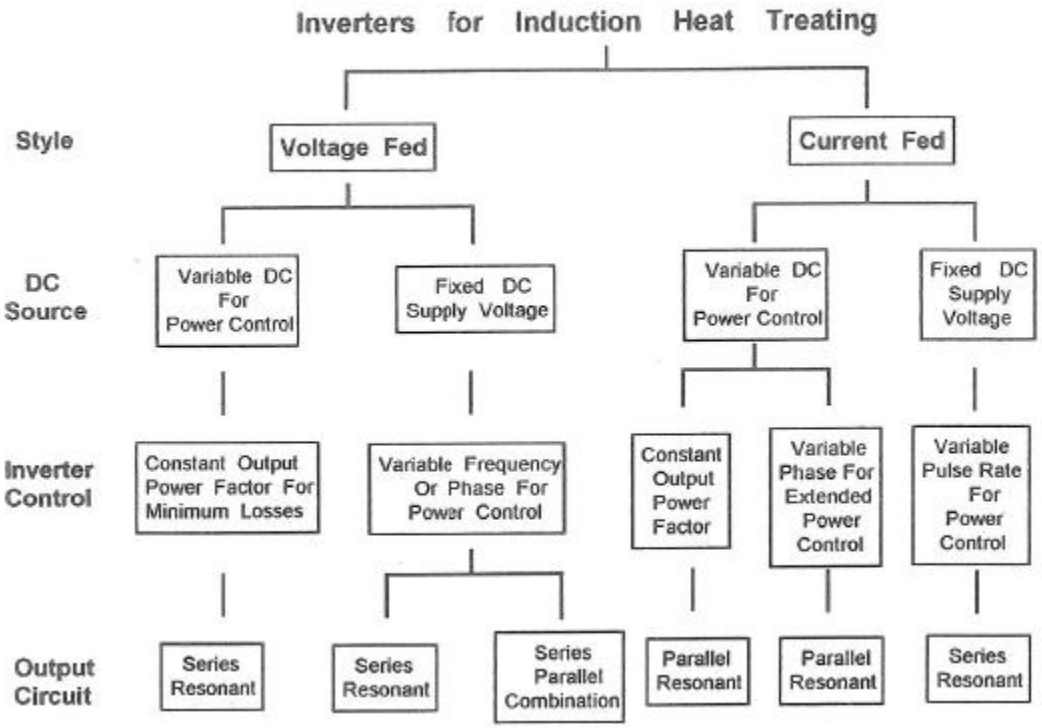

Fig. 1.25 Induction heat treatment inverters

As shown in figure 1.25, the two principal types of inverter can be divided by the DC source (fixed or variable), the mode of inverter control and the load circuit connection (series or parallel).

- **Voltage fed inverter with simple series load**

  Voltage fed inverters are distinguished by the use of a filter capacitor at the input of the inverter and a series-connected output circuit as shown in the simplified power circuit schematic of figure 1.26.

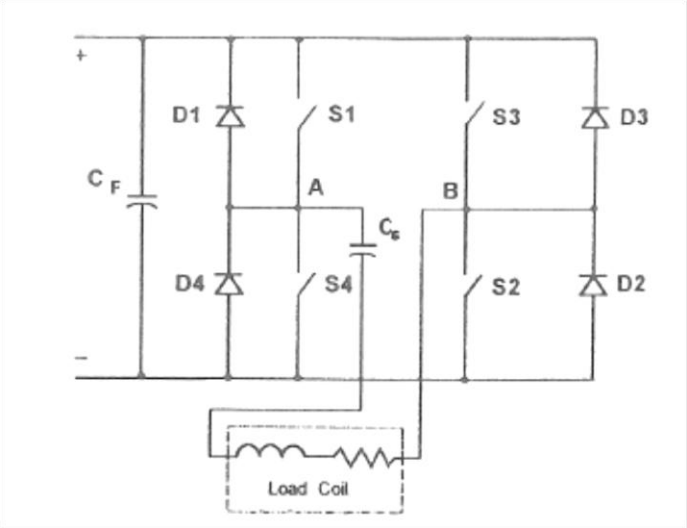

Fig. 1.26 Voltage-fed series-connected output

The series-loaded resonant converter topology has an important advantage over the parallel-loaded resonant converter in high voltage applications since it does not require an output inductor.

This inverter can be switched below resonance in the case of thyristor. Indeed diode conduction must follow thyristor conduction for sufficient time to allow the tyristor to turn off. Transistors do not require turn off time and therefore can be operated at resonance, switching while current is zero, thus minimizing switching losses and maximizing power transferred from the DC source to the load. To regulate power in this case the DC supply voltage must be controlled. Transistors can also be switched above resonance and in this case the conducting switches are turned off prior to the current reaching zero. This forces the current to flow in the diodes that are across the non-conducting switches. The non-conducting switches can then be turned on as soon as the load current change direction, thus minimizing transistor and diode switching losses while allowing the inverter to operate off resonance to regulate power.

In nearly all heat treatment applications, an output transformer is required to step up the current available from the inverter to the higher level required by the induction heating coil.

- **Voltage fed inverter with series connection to a parallel load**

  This type of inverter has an internal series-connected inductor and capacitor that couple power to a parallel resonant output as shown in figure 1.27.

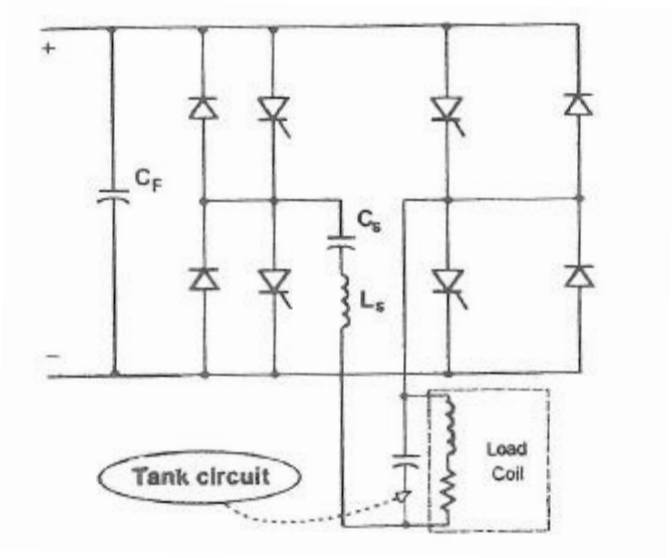

Fig. 1.27 Voltage fed inverter with series connection to parallel load

An important characteristic of this kind of inverter is that the internal series circuit isolates the bridge from the load, protecting the inverter from load faults caused for example by shorting or arcing, or badly tuned loads. This feature make this inverter a very robust induction power supply available for heat treatment.

The voltage fed inverter with series connection to a parallel load has an unregulated DC input supply. Regulation of output power is done by varying the firing frequency relative to the parallel load resonant frequency.

- **Current fed inverters**

The current fed inverter uses a variable-voltage DC source followed by a large inductor at the input of the inverter bridge and a parallel resonant load circuit at the output. Figure 1.28 shows a simplified power circuit of this inverter.

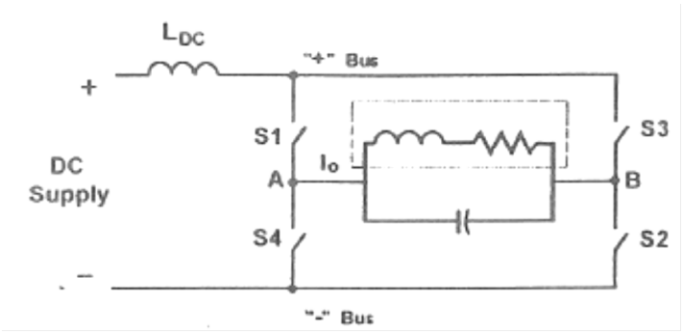

Fig. 1.28 Current fed full bridge inverter

Current fed inverter can be operated from the resonant frequency of the parallel resonant load.

At the resonant frequency the switching or commutation is done when the voltage of the load, inverter bus, and the switch is zero, minimizing the switching losses and therefore

allows for higher frequency operation. The output power musty be regulated by controlling the input current to the inverter. This is accomplished by using a variable voltage DC supply.

However power electronics is a rapidly evolving field, and several other inexpensive inverter configurations have been proposed for heat treating.

In general voltage fed inverter is preferred in applications with high ohmic inductor like melting or forging, due to its features. On the other hand current fed inverters are normally used for applications with low ohmic inductor like hardening and tube welding.

1.6.2 Load matching

A very important task during the design of an induction heating machine is to successfully deliver to the workpiece the maximum available power for a given power supply at the minimum cost.

In practice, it is usually best to tune the appropriate induction heating circuit to obtain a unity power factor and then to match the coil and workpiece impedance to that of the power supply.

This involved variable ratio transformers, capacitors and sometimes inductors that are connected between the output of the power supply and the induction coil and the adjustment of these components is referred to as load matching. Indeed, the simple addition of an isolation transformer is often not enough to satisfy the requirements of every component.

Moreover, since a relatively large current is required to successfully heat a workpiece, it is necessary to build power sources with extremely high output current capability or to use a simple resonant circuit to minimize the actual current or voltage requirement of the frequency converter and in the same time relaxing also the requirement of interconnecting cables, contactors and transformers operating in the area of the improved power factor.

It is not easy to get an optimal design of a complete induction heat treatment. Indeed the induction coil quite often is designed to achieve the desired induction heat treatment pattern without regard to the power supply that will be used. In this case, a flexible interface is required to match the output characteristics of the power supply to the input characteristics of the induction coil and workpiece combination.

Furthermore, material's properties such as electrical conductivity and magnetic permeability vary during the heating cycle. In addition, combinations of production mix and variation of materials

properties result in changing coil resistance and reactance, which affects the tuning and performance of the power supply by changing the phase angle between the coil voltage and coil current of a given circuit.

For example, flexibility is required if the heat treatment machine is general-purpose, such as a scan hardening machine. In this case, the ability to match a wide range of coils at more than one frequency is essential, and dual frequency capacitor banks is recommended.

1.6.3 Process control

The control section monitors all the parameters in the load circuit, providing an operator with information about what is actually happening during the process and whether the heat treatment of the workpiece has been successful.

With the advent of microcontroller technology, the majority of advanced systems now feature digital control, allowing systems to measure many variables at once with corresponding real-time graphing of the function within the preset set point as well as any required analysis.

For induction hardening, a list of possible variables that could ensure that the process has been successfully repeated and what the correlation is between the variables and the heat treatment process is shown in figure 1.29.

Workpiece chemistry	Workpiece geometry
Coil geometry	Coil material
Workpiece-to-coil location	Frequency
Power, voltage, current	Cycle time
Workpiece temperature	Quench flow
Quench data (media, temperature, purity, concentration)	

Fig. 1.29 variables in induction hardening

It highlights the fact that energy or coil monitors are not enough in a process as hardening, because the quenching phase is as critical to the proper hardening of the part as the heating phase.

To make an example, variation in electrical resistivity and magnetic permeability during the heating cycle leads to changes in penetration depth in the workpiece. This changes can be observed by monitoring the coil voltage, current and phase angle at the induction coil. However in induction hardening the actual change in inductance from cold to hot may be relatively small. Indeed, due to

the high power densities and magnetic field, relative magnetic permeability has relatively small values, and since penetration depth varies as the inverse square root of μ_r, there will be not great difference in inductance and impedance.

2. The gears and AISI 4340's properties

2.1 Introduction

The material properties involved in an induction heating process were briefly described in chapter 1. They depend on the temperature and also on the microstructure and on some machine's parameters as the magnetic field and heating rate.

Usually, these properties are measured in thermodynamic equilibrium conditions but induction hardening process is anything but in equilibrium. Indeed, as CHT diagrams show, heating rate may affect phase transformation temperatures, in the heating phase and also in the cooling phase. This affects also physical properties, by modifying the critical points. Usually, for high heating rate, they are shifted, generally towards higher temperatures, as shown in chart 2.1. As a result, it is very important to properly describe the materials properties in order to obtain a well-posed numerical model.

The hardened spur gears that we considered are made of a quenched and tempered AISI 4340 martensitic steel.

Chart 2.1 Transformation's temperature for AISI 4340 for different heating rate

Heating rate	Ac1 [°C]	Ac3 [°C]	Acm [°C]
2739 °C/s	726	983	1058
814 °C/s	787	982	1048
427 °C/s	778	949	1038
99 °C/s	768	856	910

2.2 Test case 1

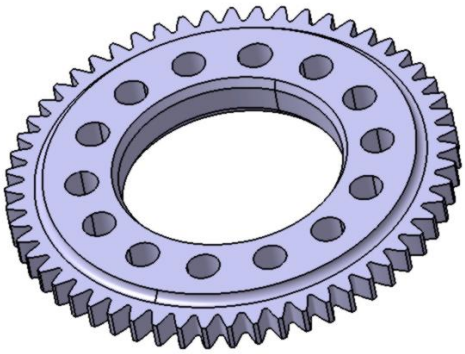

Fig. 2.1 Geometry of the gear of test case 1

The data that characterized the gear are summarized in chart 2.2.

Chart 2.2 Data of the gear

Pitch diameter [mm]	140
No. teeth	56
Module [mm]	2.5
Tooth thickness [mm]	3.656
Face width [mm]	9

2.3 Test case 2

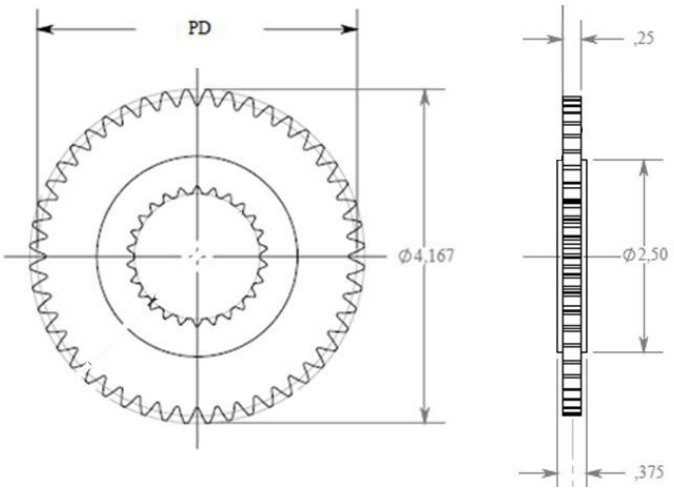

Fig. 2.2 Geometry of the gear of test case 2

Chart 2.3 data of the gear

Number of teeth	48
Diametral pitch	12.00
Pressure angle	25.00°
Outside diameter	105.84 mm
Base diameter	92.08 mm
Root diameter	95.38 – 95.50 mm
Pitch diameter	101.6 mm
Form diameter	97.88 mm
Arc tooth thickness	3.20-3.25 mm
Tooth length	6.35 m

2.4 AISI 4340

AISI 4340 is a heat treatable, low alloy steel containing nickel, chromium and molybdenum. It is very suitable for the process of induction hardening considered the carbon content and the alloying elements which improve the hardenability and the mechanical properties of the heart. Indeed it is known for its toughness and capability of developing high strength in the heat treated condition while retaining good fatigue strength.

Typical applications are for structural use, such as aircraft landing gear, power transmission gears and shafts and other structural parts.

Chemistry data of AISI 4340 are summarized below.

Chart 2.4 Chemistry data of AISI 4340

Element	**weight %**
Carbon	*0.38-0.43*
Manganese	*0.60-0.80*
Phosphorus	*0.035 (max)*
Sulphur	*0.04 (max)*
Silicon	*0.15-0.30*
Chromium	*0.70-0.90*
Nickel	*1.75-1.90*
Molybdenum	*0.20-0.30*

2.4.1 Relative magnetic permeability

Magnetic permeability μ_r influences the skin depth, given by the following formula

$$\delta = \sqrt{\frac{2 \cdot \rho}{\omega \cdot \mu_r \cdot \mu_0}}$$

and hence the power distribution due to the eddy currents.

The evolution of μ_r as a function of temperature is a simplistic representation of a much more complex behavior. Indeed, neglecting the effect of the microstructure, the relative magnetic permeability also depends on the magnetic field strength.

During high frequency induction heating, in itself very short, the different parts of the gear are affected by different values of magnetic field. In the more complex cases of a preheating at medium frequency or a double frequency, the variation in frequency influences also the distribution of the magnetic field.

The measurement of μ_r remains a difficult task and requires advanced measurement techniques and colossal resources for heating rates.

Figure 2.3 shows the behavior of μ_r as a function of temperature for different values of magnetic field.

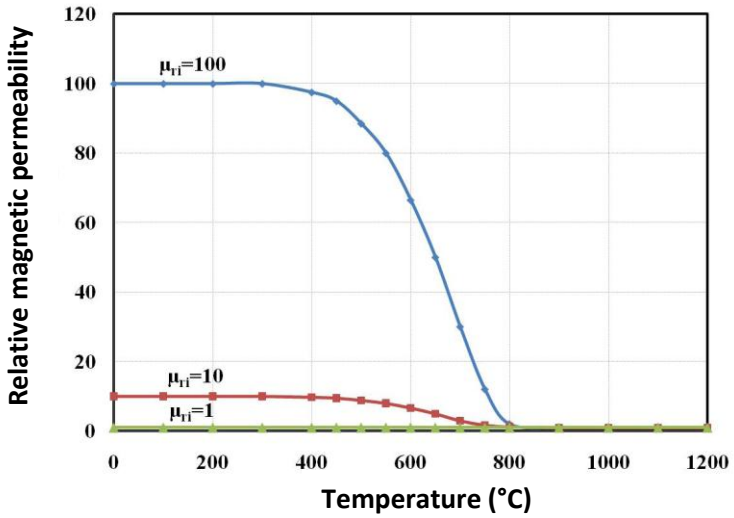

Fig. 2.3 $\mu_r(T)$ of steel for different magnetic field intensities

It is possible to see that all the curves have a common characteristic. Below Curie temperature, at about 770°C, the permeability is decreasing while the magnetic field intensity is increasing. Above the curie temperature, μ_r is always unity.

In particular in literature it is shown that considering a higher initial value of μ_r the edge effect will be enhanced and superficial temperatures of the workpiece increase, in a HF heating [9].
So, in the numerical model it is very important to consider the correct μ_r profile as a function of temperature or, better, even as a function of magnetic field.
Furthermore, it is demonstrated by sensitivity study of material properties that relative magnetic permeability is the parameter whose variations affect more the profile's temperature, especially in HF heating. This is due to its influence on skin effect and edge effect.

2.4.2 Specific heat

To quantify the effects of the heating rate on specific heat profile as a function of temperature for AISI 4340, three curves Cp1, Cp2 and Cp3 are considered in figure 2.4.

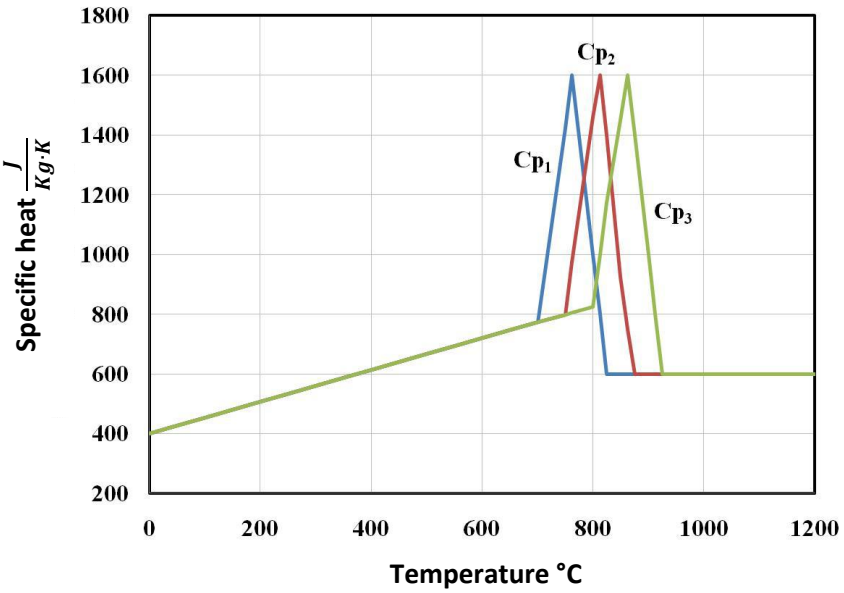

Fig. 2.4 different specific heat curves for AISI 4340, as a function of temperature

These curves are obtained by shifting temperatures Ac1 and Ac3 and assuming constant the latent heat peak, taking into account the variations of critical points of steel due to high heating rate.
This behavior generally allows the workpiece to reach lower maximum temperature, due to the higher energy required for heating a material which has higher specific heat (area of the shifted curve is greater that the non shifted curves).

2.4.3 Electrical conductivity

Studying the effect of the heating rate of electrical conductivity for AISI 4340, three temperatures of Ac3 are considered: 775°C, 825°C and 875°C. Curves σ1, σ2 and σ3 respectively represent the three related conductivities, showed in figure 2.5. Curve σ1 is the behavior in thermodynamic equilibrium. Above Ac3 temperature, electrical conductivity is assumed constant.

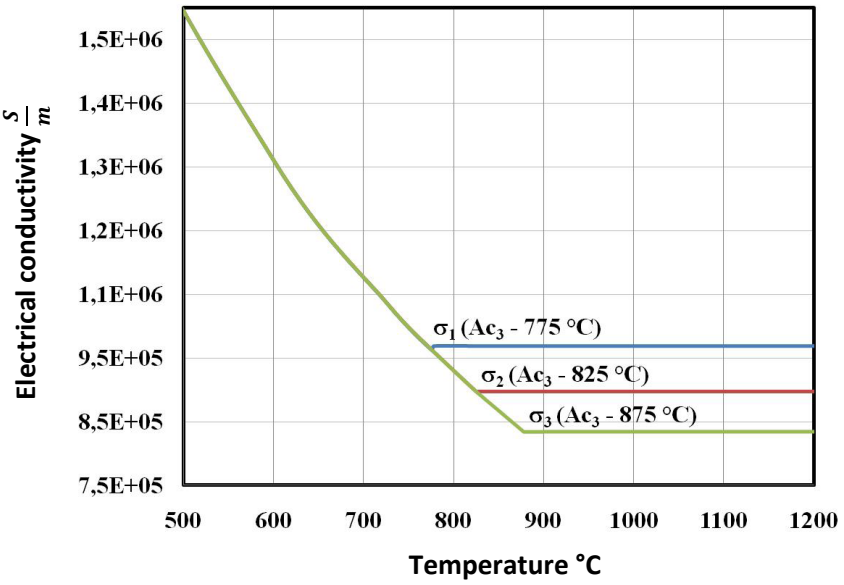

Fig. 2.5 influence of heating rate on electrical conductivity of AISI 4340

It is clear that increasing heating rate and hence Ac3 temperature, conductivity decrease.
However variations of this property affect very little temperature's profile [9], so in this work they are neglected.

2.4.4 Thermal conductivity

This property depends on the temperature and on the heating rate too. The three curves in fig 2.6 show the behavior of thermal conductivity for AISI 4340 at different Ac3 temperatures; 775 ° C, 825 ° C and 875 ° C.

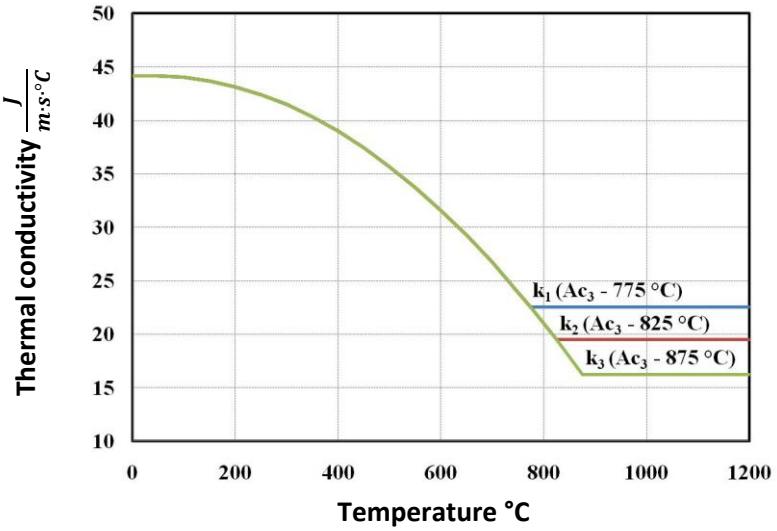

Fig. 2.6 Thermal conductivity for different Ac3 temperatures

The curves show that thermal conductivity reaches a minimum at the austenitization temperature. However, even in this case, variations of this property don't affect much the surface's temperatures [9], so we will neglect them on numerical model.

3. Numerical modeling of the process

3.1 Introduction

The design of induction hardening devices and the choice of the hardening parameters such as frequency, inductor's current and power, are often carried out by experience and experimentation. Nevertheless, as mentioned before, this approach results very expensive and difficult if complex geometries of the workpiece are involved and even studying the effect of the variation of hardening parameters results very hard. Thus, simulations dramatically reduce development time of the process and reduce rejection of samples.

The numerical simulations of induction heating process offer new possibilities in these fields. Together with validation tests, these models provide an essential solution to control the method of heat treatment by induction.

The finite element method (FEM) is a numerical technique for obtaining an approximate solution to different technical problems, including those encountered in induction heat treatment.

In general in finite element discretization we have that the area of study is subdivided into nonoverlapping finite elements. The sides of finite elements intersect at nodes.

The FEM provides an element wise approximation to the governing equations (reported below), solving the global set of resulting simultaneous algebraic equations with respect to the unknown, for example magnetic vector potential at each node in the region of evaluation.

$$\frac{1}{\mu_r \cdot \mu_0} \cdot \nabla \times \left(\nabla \times \vec{\mathrm{A}}\right) = -j\omega\sigma\vec{A} + \overrightarrow{J_o}$$

$$\rho \cdot c \cdot \frac{dT}{dt} = \lambda \cdot \nabla^2 T + Q_{ind}$$

To obtain reasonable accuracy of the numerical solution, the finite element mesh has to be relatively fine in the regions where the rate of change of the unknown (i.e. magnetic vector potential and temperature) is high.

The current density, flux density, conductivity, magnetic permeability and other material properties are postulated to be constant within each element.

In order to reduce the complexity of the computation, the designer should take advantage of the symmetry involved in the system geometry.

After solving the system of algebraic equations and obtaining the distribution of the magnetic vector potential in the region of modeling, it is possible to find all the required output parameters of the electromagnetic field such as:

- induced current density in conductors $\overrightarrow{J_e} = -j\omega\sigma\vec{A}$
- total current density in the conductor $\vec{J} = \overrightarrow{J_0} - j\omega\sigma\vec{A}$
- magnetic flux density components by the relation $\vec{B} = \nabla \times \vec{A}$ and hence flux density $\vec{B}$
- magnetic field density from the relation $\vec{B} = \mu_r \cdot \mu_0 \cdot \vec{H}$
- electric field intensity $\vec{E} = -j\omega\vec{A}$
- Electromagnetic force density in current-carrying conductors and in the workpiece by the formula $\vec{F} = \vec{J} \times \vec{B}$

Finally from a vector potential solution it is possible to compute the other important quantities of the process such as energy stored, flux leakage, total power loss and coil impedance.

Different finite element programs are used for the computation of coupled electromagnetic and thermal problems, such as ANSYS, COMSOL and FLUX. These tools also allow to take into account important temperature-dependent material parameters. FLUX 3D is used in this study to carry out different analysis.

In this chapter the steps needed to build simulations and related problems have been described,:

- Building of the geometry
- Building of the mesh
- Description of the materials and their properties
- Description of the problem and of the boundary conditions
- Post-processing and analysis of the results

3.2 Building of the geometry

FLUX 3D allows designers to import geometries drawn with CAD-CAE software. Simple geometries could be drawn directly on FLUX. The geometry of test case 1 has been imported from CAD-CAE software. This gear is showed in the picture of this chapter. The geometry of test case 2 has been designed directly on FLUX.

In order to reduce the computing time, it is necessary to reduce as much as possible the geometry, by exploiting the symmetries of the workpiece.

In the case of a gear, the original circular geometry is reduced in a quarter of tooth exploiting the tooth periodicity and its symmetry along the middle radial plane.

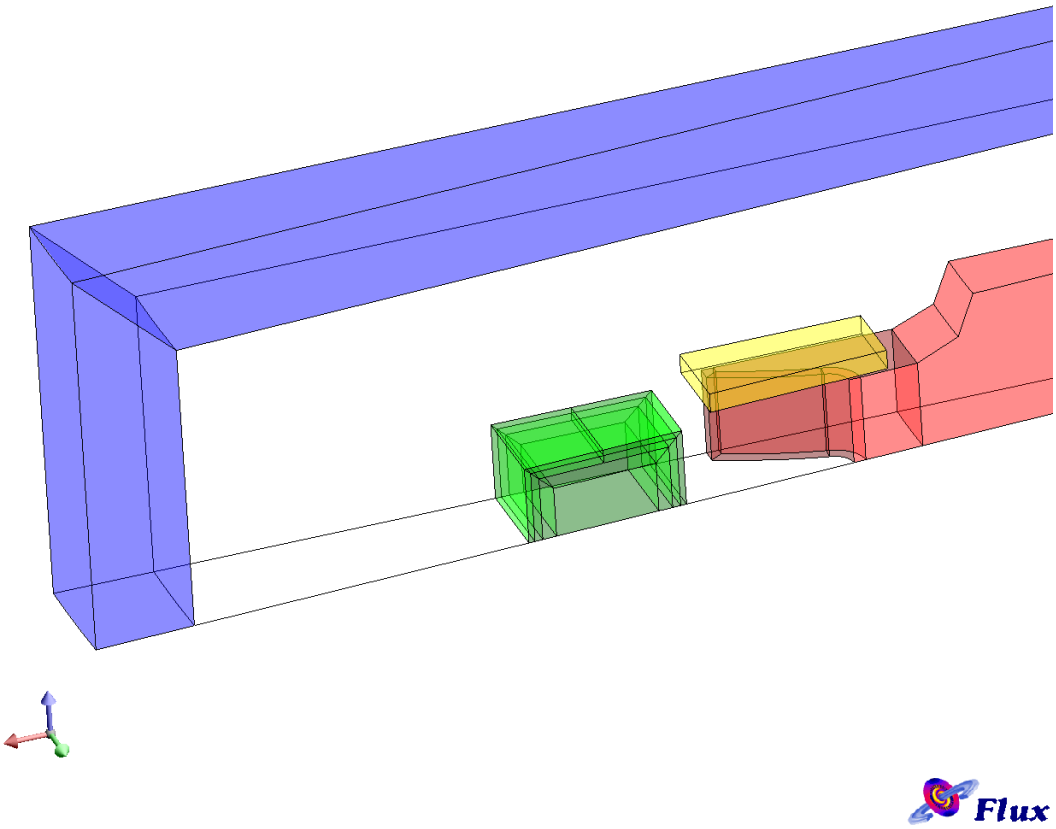

Fig. 3.1 Geometry and infinite box, test case 1

The coil has been designed only taking into account the active part and considering only the electrical properties. This hypothesis is not so far from reality because the coil is water cooled, and its temperature doesn't change a lot during the process. Moreover, at high frequency, current will be distributed mainly on the interior surface of the coil, due to the skin effect and the proximity effect.

At the boundary of the simulation domain, infinite boundary conditions have been posed in order to let the magnetic field vanish at infinite distance by means of an “infinite Box”.

The effect of a ring made in magnetic but non-conductive material above the gear, called flux concentrator, has also been studied in the analysis of the model. All the parts of the model (the gear, the coil, the flux concentrator and the infinite box) were split into different volumes, in order to allow the designer to better develop the mesh and the model in general.

3.3 Building of the mesh

As mentioned before, when defining the mesh it is very important that superficial elements are very dense. It is also very important to accurately describe the surface of the inductor because its current will be distributed in a thin layer, due to skin effect, ring effect and proximity effect.

The conditions are more critical at higher frequency, where δ is lower. In this work the maximum frequency considered was 250 kHz, so we have

$$\delta_{250000,AISI4340,20°C} = \sqrt{\frac{2 \cdot \rho}{\omega \cdot \mu_r \cdot \mu_0}} = 0.161\ mm$$

$$\delta_{250000,copper,20°C} = \sqrt{\frac{2 \cdot \rho}{\omega \cdot \mu_r \cdot \mu_0}} = 0.142\ mm$$

Where we consider for copper that

$\rho = 2 \cdot 10^{-8} \Omega \cdot m$ $\mu_r = 1$

And for AISI 4340 we have

$\rho = 2.57 \cdot 10^{-7} \Omega \cdot m$ $\mu_r = 10$

Hence it is necessary to have at least 2 surface elements of about 0.05 mm to obtain truthfully results and for the convergence of the solution.

Moreover, as shown in figure 3.2, a superficial volume has been built in the coil and in the gear that have mapped mesh, rather that automatic such as in the other parts of the model.

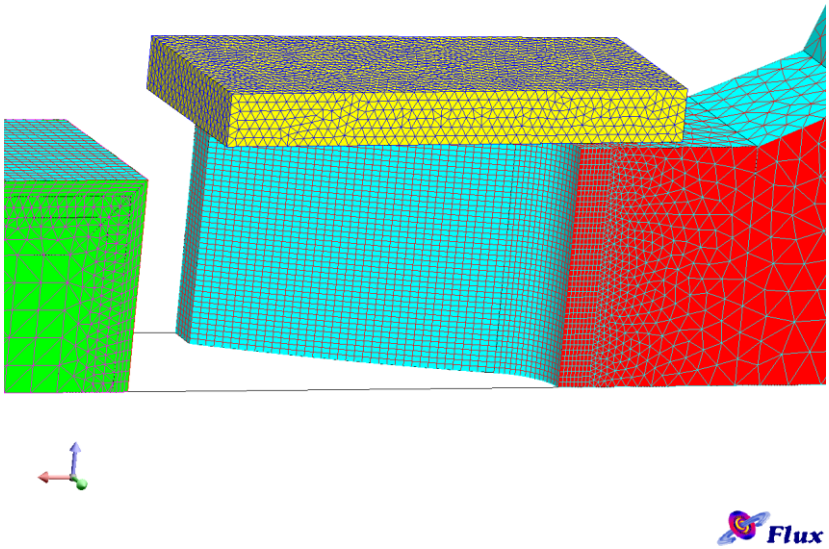

Fig. 3.2 mapped mesh on the coil and on the inductor, test case 1

In the inner areas of the gear, where magnetic field is weaker than in the surface, a more relaxed mesh has been designed, reducing the number of elements and hence the computation time. Likewise, in the interior part of the coil a relaxed mesh has been built.

Differentiation of the dimensions of mesh elements was possible by creating what is called "mesh lines". Indeed, we imposed the length of the elements at the beginning and at the end of lines, relaxing the mesh when low magnetic field is involved.

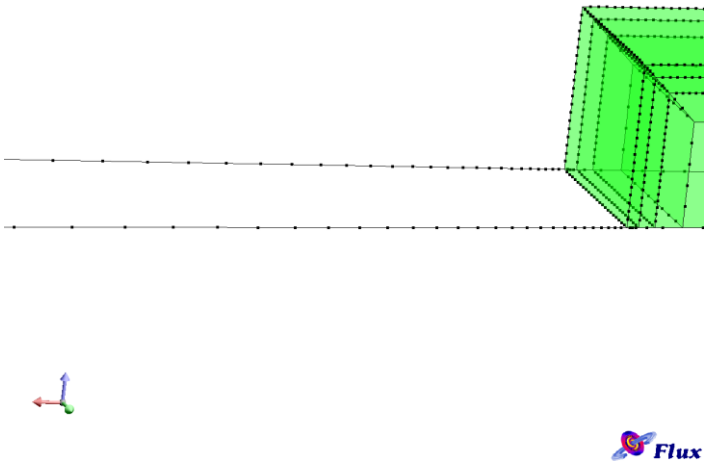

Fig. 3.3 example of mesh lines.

3.4 Description of materials and their properties

As already clarified, we have to introduce some approximations for the description of the model, due to the uncertainty of data in literature and to the limits of the simulation programs.

1. **Gear:** The properties of AISI 4340 have been described in the previous chapter. In particular it is not easy to solve complex computational models with relative permeability function of both temperature and magnetic field. An alternative could be using a magnetic permeability function only of temperature, taking in account the magnetic field agent choosing the value of μ_{20} (see figure 3.4).

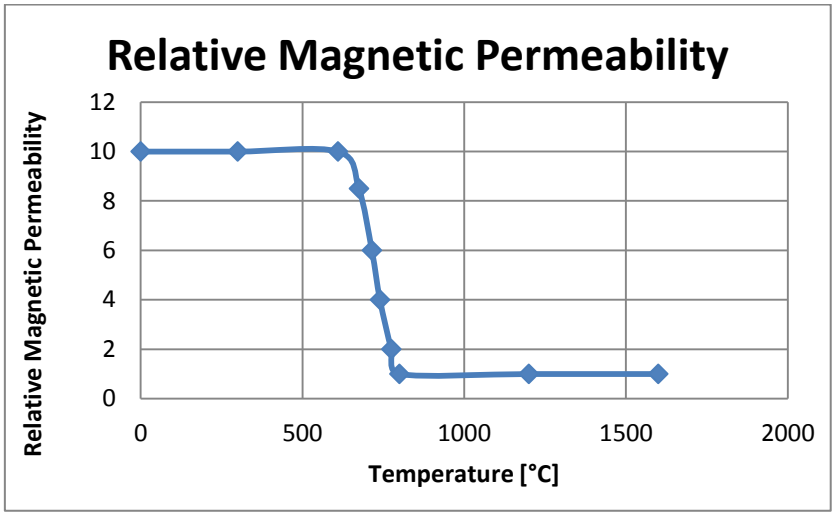

Fig. 3.4 relative magnetic permeability as a function of temperature, test case 1

Volumetric heat capacity trend for test case 1 is shown in figure 3.5.

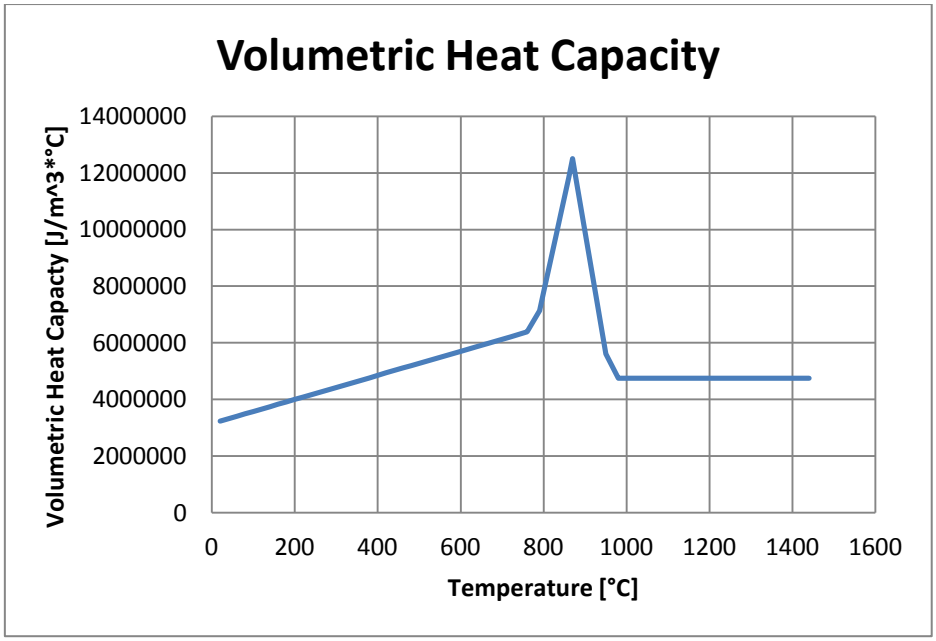

Fig. 3.5 Volumetric heat capacity, test case 1

The superficial average heating rate was taken into consideration by shifting the specific heat peak. For the computation of heating rate in the different recipes we considered only the HF heating.

Chart 3.1 Heating rate

	HF heating (s)	Ac1 (°C)	Ac3 (°C)	Average superficial Heating rate (°C/s)
Test case 1	0.2	778	949	2700
Test case 2	2	726	983	500

Electrical and thermal conductivity are shown in figure 3.6 and 3.7 respectively.

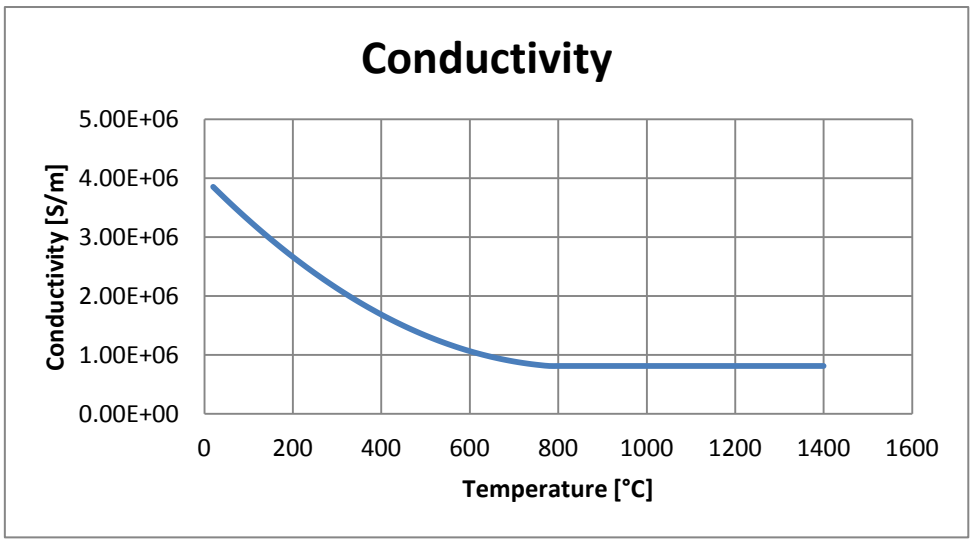

Fig. 3.6 electrical conductivity as a function on temperature, test case 1 and 2

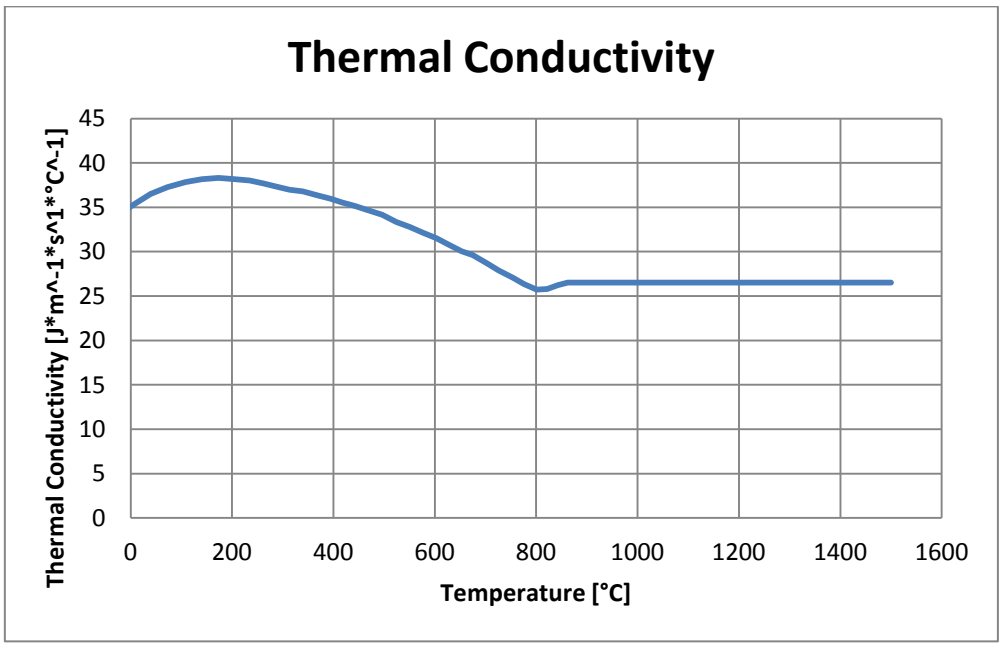

Fig. 3.7 thermal conductivity as a function of temperature, test case 1 and 2

We neglect the influence of high heating rate on the latter two properties.

2. **Coil:** The coil is made of copper. We consider the resistivity $\rho = 2 \cdot 10^{-8} \Omega \cdot m$.
3. **Flux concentrator:** Soft magnetic composites materials iron-and-ferrite-based compositions called flux concentrators are provided by different industries in order to obtain selective heating of certain areas of the workpiece, improving the electrical efficiency of the induction coil and acting as an electromagnetic shield to prevent the undesirable heating of adjacent regions. As a result these materials must have a high relative permeability and low-power-losses.

   One of the flux concentrator used in induction heating is "FLUXTROL 50", because of its good performance over a wide range of frequencies (10-1000 kHz).

Chart 3.2 Properties of FLUXTROL 50

Density	6.1 g/cm^3
Initial Permeability	36
Maximum Permeability	55
Saturation Flux Density	1.5 T
Operating Frequency Range	10-1000 kHz
Major Frequency Range	50-500 kHz
Temperature Resistance	250 °C Long Term 300 °C Short Term
Thermal Conductivity	0.06 W/cm K
Resistivity	0.5 kΩcm

In numerical models simplifications are necessary in order for the model to be solved in a reasonable time. In particular, considering the value of magnetic field involved in the induction hardening process, we assume for the flux concentrator a value of relative magnetic permeability of 40, constant with temperature. Moreover, the actual resistivity of FLUXTROL 50 is very high and so we can assume that it is non conductive. These assumption allows the model to be simplified without making too many mistakes.

3.5 Description of the problem and of the boundary conditions

Solving the coupled magnetic and thermal problem to simulate the induction hardening process, the "Steady-state AC Magnetic Transient Thermal" has been chosen.

To complete the model, it has been necessary to define "volume regions", and assign them to "real" volumes, in order to assign the behavior of the different part of the model. The volume regions created could be described as follows.

Chart 3.3 Volume regions

VOLUME REGION	MAGNETIC DEFINITION	THERMAL DEFINITION	MATERIAL
AIR	Air or Vacuum region	Inactive region	/
COIL	Solid conductor region	Inactive region	Copper
GEAR	Solid conductor region	Heat computed by Joule effect	AISI 4340
FLUX CONCENTRATOR	Magnetic non conducting region	Inactive region	Fluxtrol 50

Moreover, a voltage control has been chosen to regulate the power in the workpiece. This was done by imposing an electric potential at the end of the inductor. Taking into account the symmetries of the problem the electric potential has been assigned to the faces of a fraction of the entire circular section of the inductor. This was done by creating two "face regions", described in chart 3.4. Another face region was created to play back the effect of losses by radiation and convection. For convection an α coefficient of 10 has been considered while for radiation losses a value of $\varepsilon = 0.8$ has been chosen. These conditions have been assigned in the external part of the gear that are the hottest.

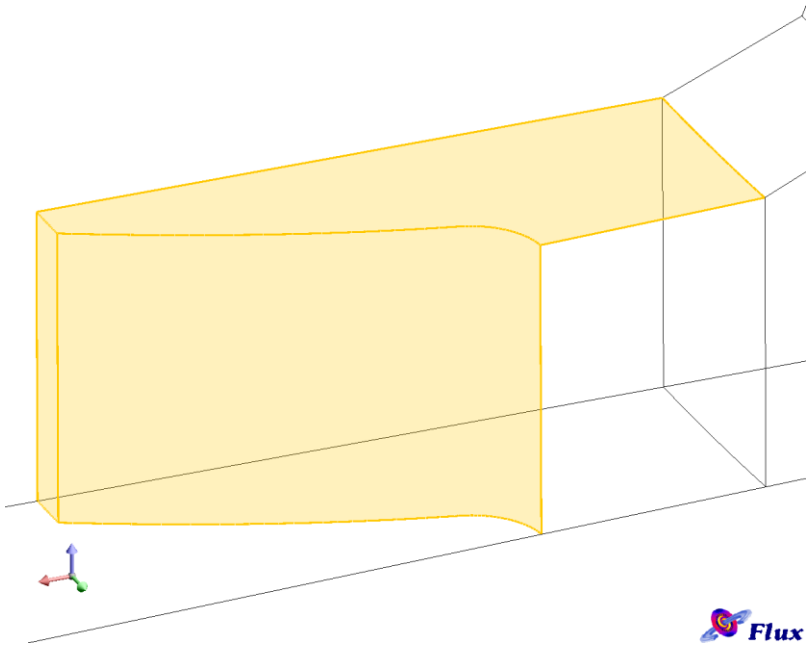

Fig. 3.8 external faces subject to radiation and convection losses, test case 1

chart 3.4 Face regions

REGION	MAGNETIC DEFINITION	THERMAL DEFINITION
V0	Boundary condition: Imposed electrical potential	Inactive region
V1	Boundary condition: Imposed electrical potential	Inactive region
EXCHANGE	Inactive Region	Surface of thermal exchange and heat source

3.6 Computation and post processing of the results

Once the mesh and the physics of the problem have been designed, the model is ready for the computation.

For the computation it is important to remember for the computation that:

- Very short time steps are required during high power variations, such as at the beginning or at the end of a heating phase, to allow the convergence of the method.
- Longer time step are required during the preheating phase in MF, as there are lower values of temperature and power density gradient in the workpiece.
- Short time steps are required for the convergence of the method in the heating phase in HF, due to the higher temperature and power density gradient.

Simulations have been solved with a Professional Workstation, and computing time varied from three to six hours, as a function of the number of time steps implemented.

It has been possible to achieve a great number of output parameters in all the time steps, as already clarified.

4. Optimization of induction hardening parameters

4.1 Introduction

In this work simulations are used to study the effect of machine's parameters such as frequency and dimension of the inductor on the distribution of temperature, and also to evaluate the effect of a flux concentrator above the gear. This in order to obtain a homogeneous hardened profile of at least 0.6 mm, both in the tip and in the tooth of the gear. Furthermore is also important to prevent the entire tooth from being austenitised, avoiding unwanted phenomena which would lead to a deterioration of the mechanical properties.

Numerical models are very useful for this kind of study. Indeed, they allow researchers to save a great amount of energy, materials, time and equipment needed for the measurements. Moreover it is possible to compute the parameters, such as power, needed by designers in order to design properly an induction hardening machine.

Once the model of test case 1 has been built following the principle explained in the previous chapter, the induction hardening process was split into 3 periods. The first, preheating at MF; the second, an interruption of power of 0.2 s needed by experimental devices for changing the frequency and required also by diffusion to homogenize the temperature; finally, the third, the real hardening that consists in 0.2 s HF at 350 kW.

4.2 Influence of flux concentrator

To understand the effect of the flux concentrator, 3 models have been created: Recipe A and B with two different thicknesses of flux concentrator (2 and 1 mm respectively) and recipe C without it. All the simulation consists in a 3 s of preheating phase at 5000 Hz, and 0.2 s of heating phase at 200 kHz. The dimension of the inductor is 8 mm height and 8 mm thick.

The following figures show the inducted power density, the magnetic field arrows and the temperature's profile at the end of the HF heating phase for all the recipes.

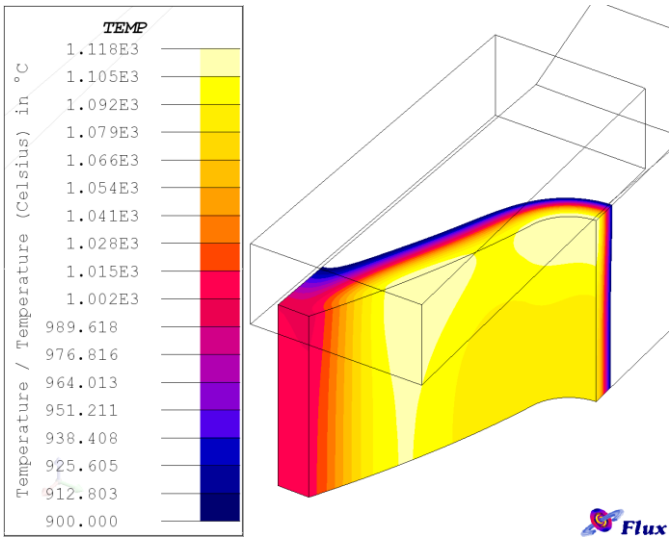

Fig. 4.1 900°C isotherm at the end of HF heating, recipe A

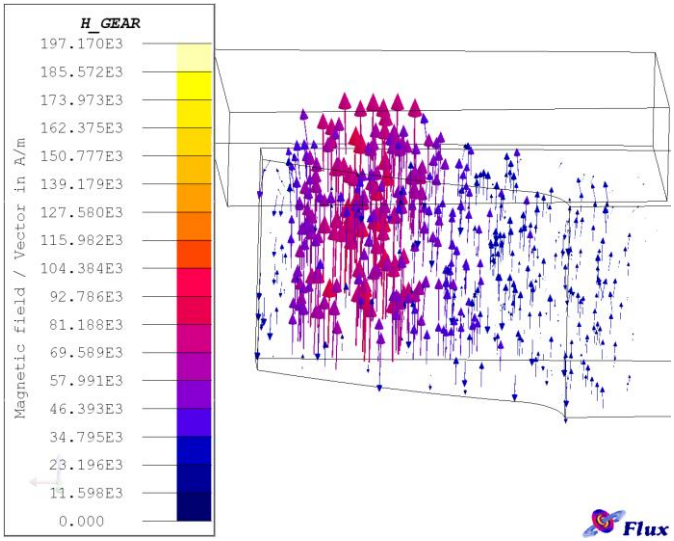

Fig. 4.2 magnetic field arrows at the end of HF heating, recipe A

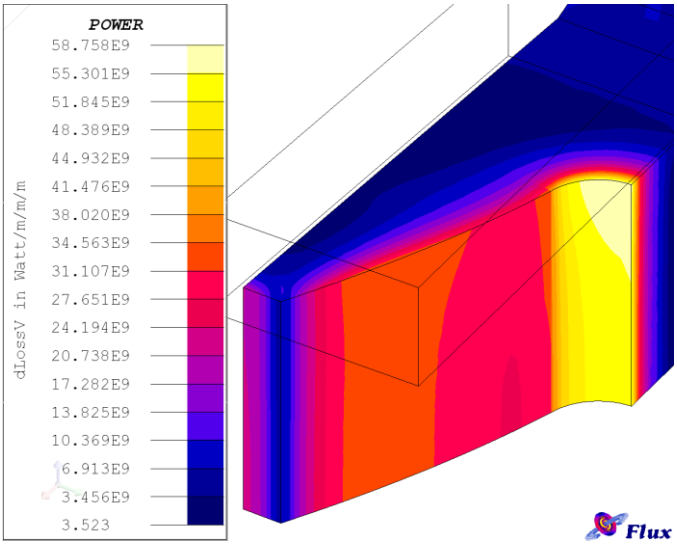

Fig. 4.3 power density at the end of HF heating, recipe A

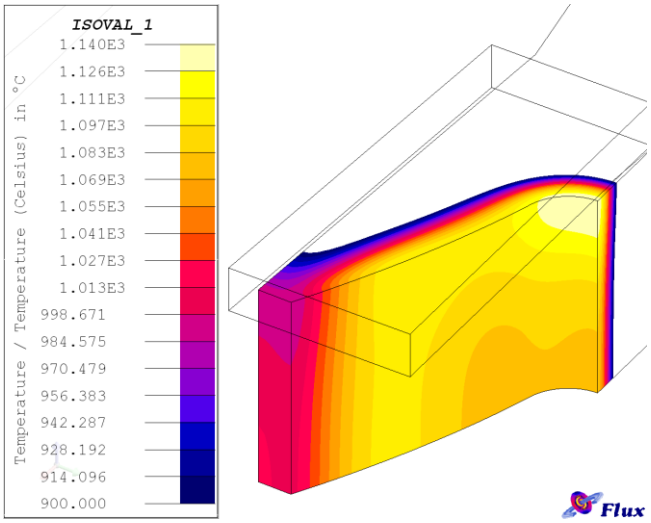

Fig. 4.4 900°C isotherm at the end of HF heating, recipe B

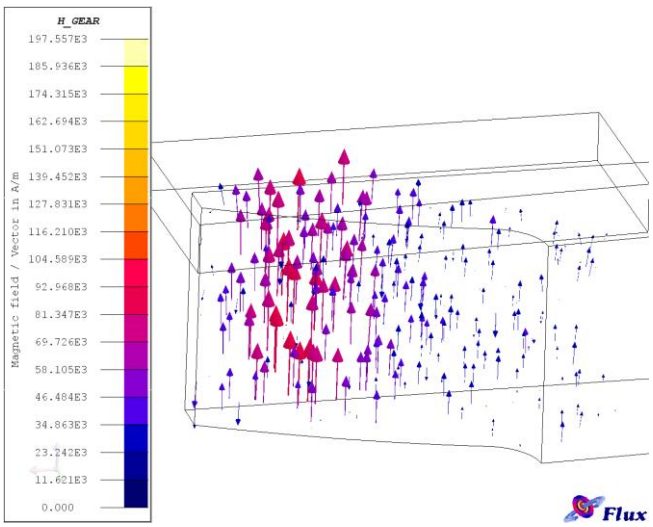

Fig. **4.5** magnetic field arrows at the end of HF heating, recipe B

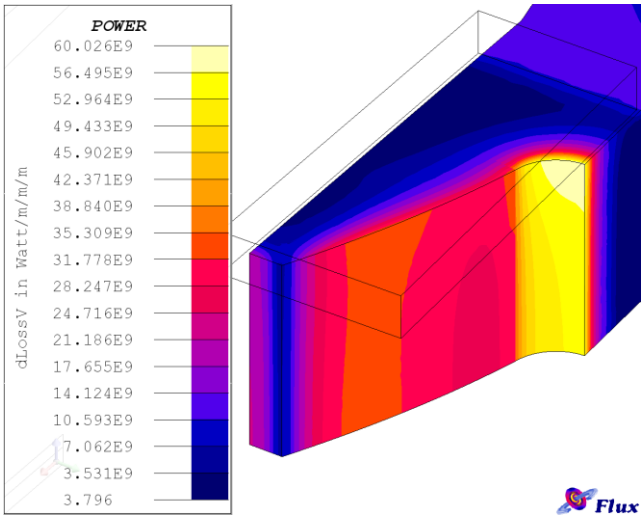

Fig. **4.6** power density at the end of HF heating, recipe B

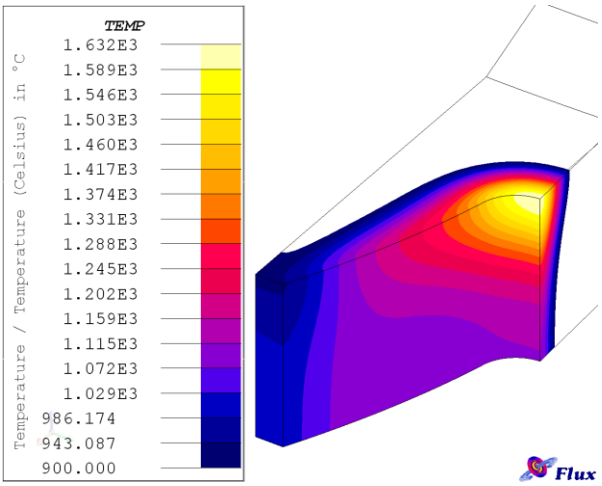

Fig. 4.7 900°C isotherm at the end of HF heating, recipe C

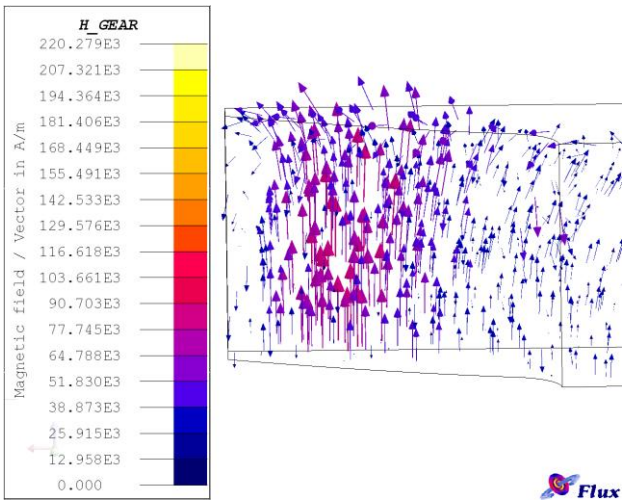

Fig. **4.8** magnetic field arrows at the end of HF heating, recipe C

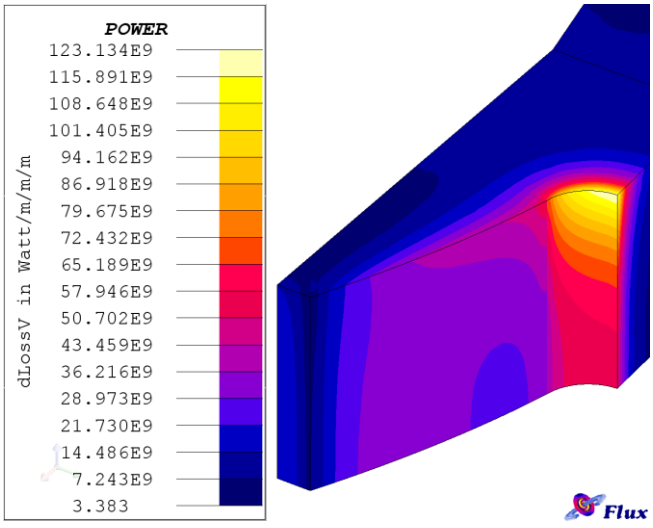

Fig. **4.9** power density at the end of HF heating, recipe C

It is possible to see how magnetic field lines tend to close in the workpiece, causing the edge effect. This phenomenon is more marked in the model without flux concentrator, both in the tip and in the root. As a result, the maximum power density value is about twice in the case without flux concentrator in the external part of the root. In order to evaluate the uniformity of the heating between the middle and the surface of the gear, the parameter of uniform heating is introduced as

$$P.U.H. = \frac{MD}{SM}$$

Where SM is the heating depth in the surface of the gear, and MD in the middle. The more P.U.H. is close to unity, the more the heating is homogeneous.

Chart 4.1 Depth of the 900°C isotherm

		Root			tip		
Recipe	Thickness of the flux concentrator (mm)	MD (mm)	SM (mm)	P.U.H	MD (mm)	SM (mm)	P.U.H.
A	2	0.58	0.66	0.88	1.69	1.63	1.04
B	1	0.59	0.71	0.83	1.68	1.53	1.10
C	/	0.66	1.33	0.50	1.06	1.61	0.66

Consequently, the flux concentrator allows the workpiece to obtain a more homogeneous power density throughout the length of the root, and hence a better distribution of temperature between the external part and the internal part of the gear. This will certainly evolve in a more homogeneous hardened layer. We can conclude that the higher thickness the flux concentrator has, the smaller is the edge effect, at the same power applied. However increasing the thickness of the flux concentrator beyond 1 mm doesn't reduce much more the edge effect.

4.3 Influence of inductor's dimensions

Three simulations with different height of the coil are proposed. A 1 mm thickness flux concentrator has been left. A 3 s, 5 kHz preheating and a 0.2 s, 200 kHz shot have been proposed for all the recipes. For the simulations to be comparable, the same current was flowing in the inductor.

Recipe	height of the coil (mm)
D	6
E	8
F	10

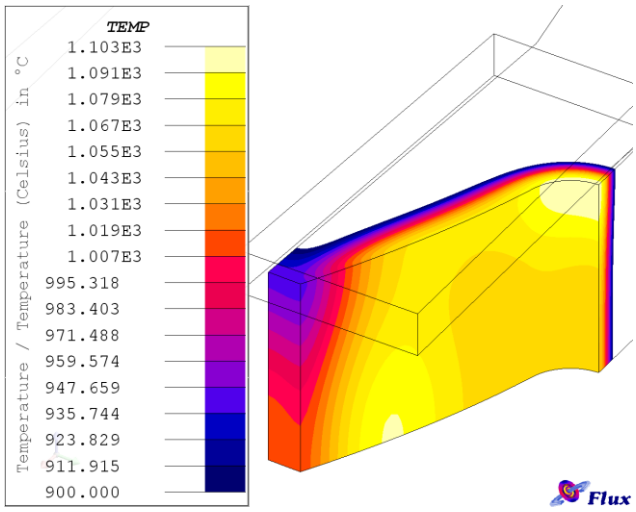

Fig. 4.10 900°C isotherm at the end of HF heating, recipe D

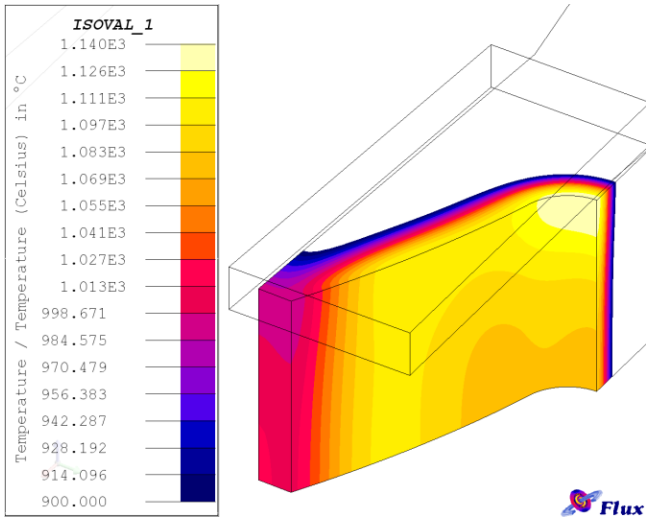

Fig. 4.11 900°C isotherm at the end of HF heating, recipe E

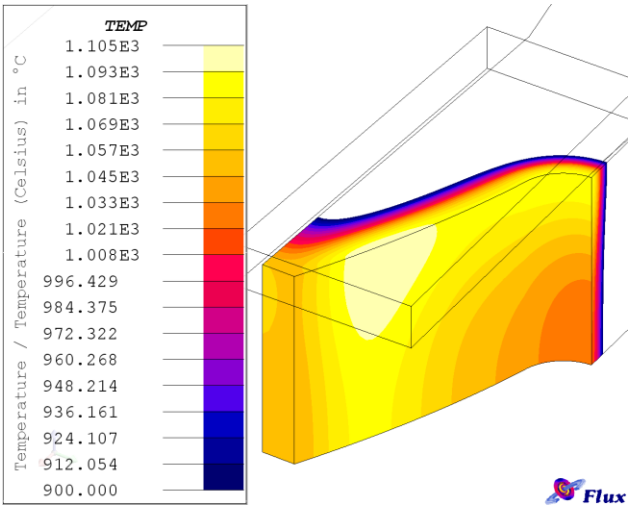

Fig. 4.12 900°C isotherm at the end of HF heating, recipe F

Figures show that the dimension of the coil affects the final distribution of temperature. In particular if the height of the coil is rather small compared with the height of the gear, the external part of the tip remains colder than the core of the tip. This behavior is certainly caused by the fact that the eddy current in the gear are mainly distributed in the section in front of the coil. On the other hand, if the coil's height is greater than the height of the gear, the external part of the tip are more heated. It is important to remember that in the edge of the gear the power density are higher because of the edge effect. Therefore the choice of the dimension of the coil is a compromise in order to obtain a heating as homogeneous as possible along the contour of the tooth. Usually a coil slightly lower than the gear is chosen.

4.4 Influence of the frequency and the duration on MF preheating phase

In order to understand how preheating phase affects the final distribution of temperature, different models have been proposed. The same 200 kHz, 0.2 s heating phase is considered for better comparison.

Recipe	Preheating time (s)	Preheating frequency (kHz)
1	1	10000
2	1	5000
3	1	1000
4	3	10000
5	3	5000
6	3	1000
7	5	10000
8	5	5000
9	5	1000

The power of the different preheating phase was calibrated by varying the tension of the inductor so as to achieve the same superficial temperature at the end of the MF heating, always kept below 600°C in order to avoid modifications of the microstructure.

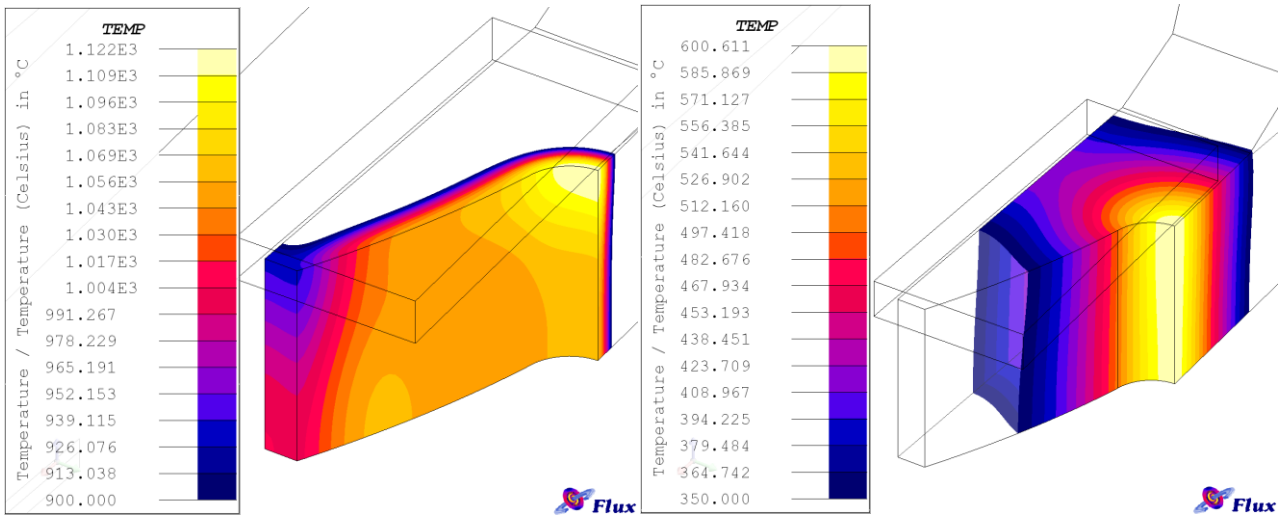

Fig. 4.13 isotherms at the end of HF and MF heating respectively, recipe 1

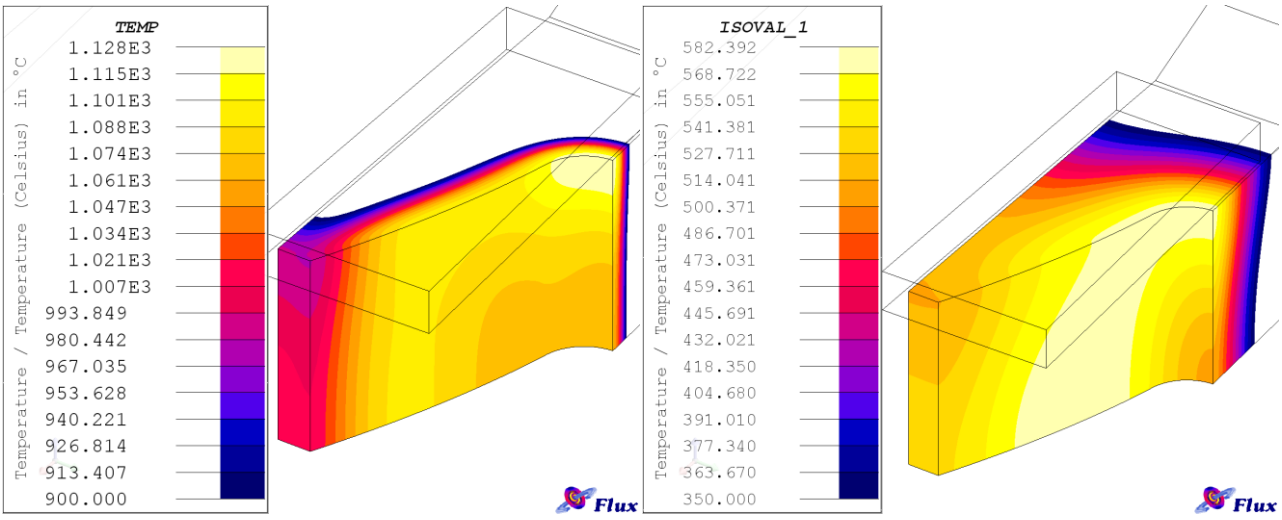

Fig. 4.14 isotherms at the end of HF and MF heating respectively, recipe 2

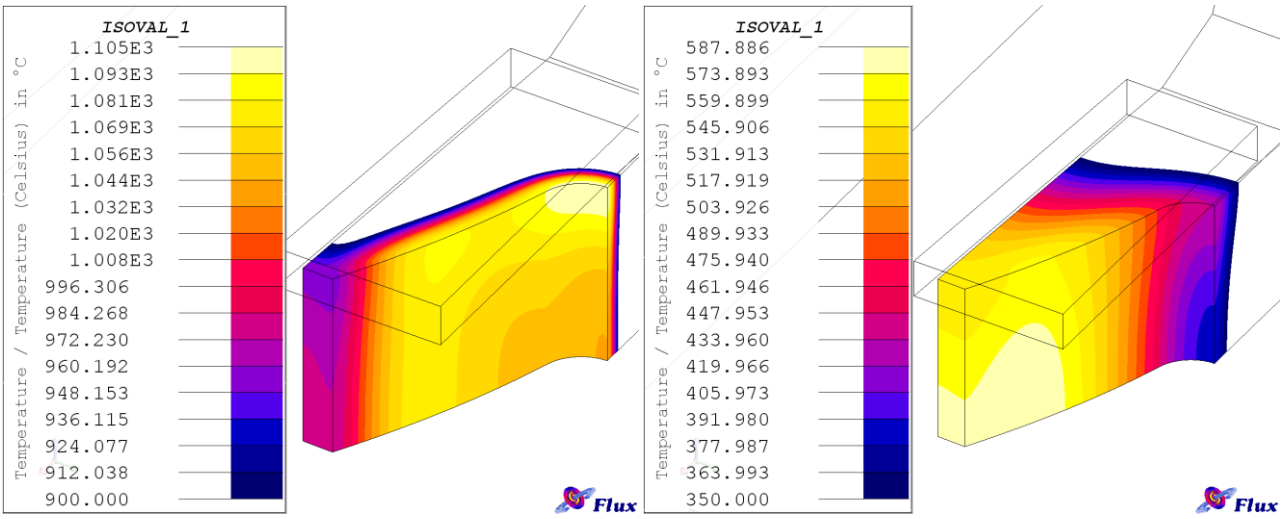

Fig. 4.15 isotherms at the end of HF and MF heating respectively, recipe 3

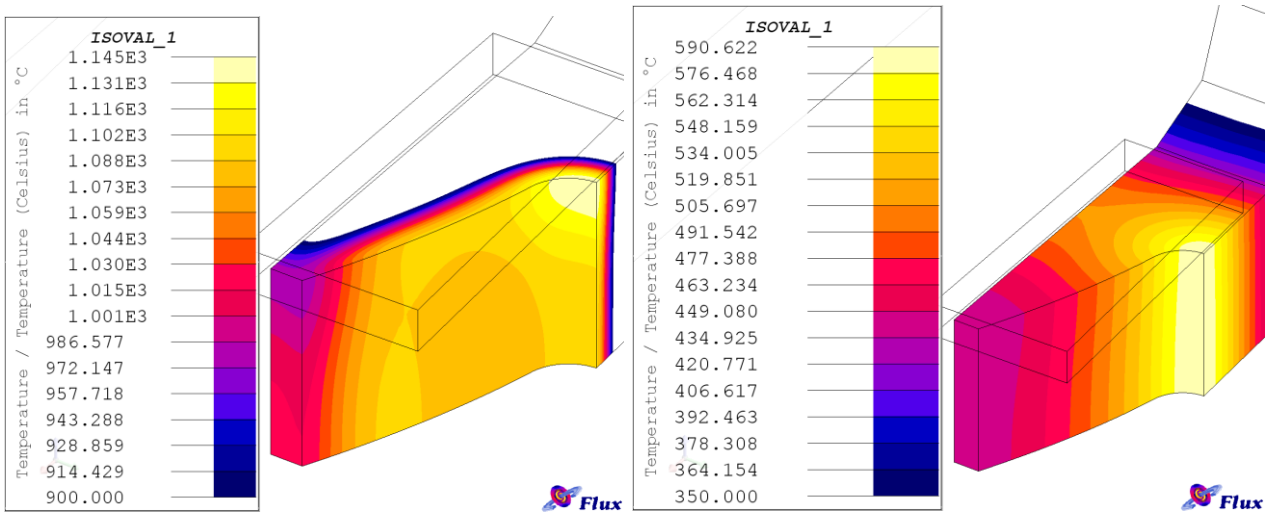

Fig. 4.16 isotherms at the end of HF and MF heating respectively, recipe 4

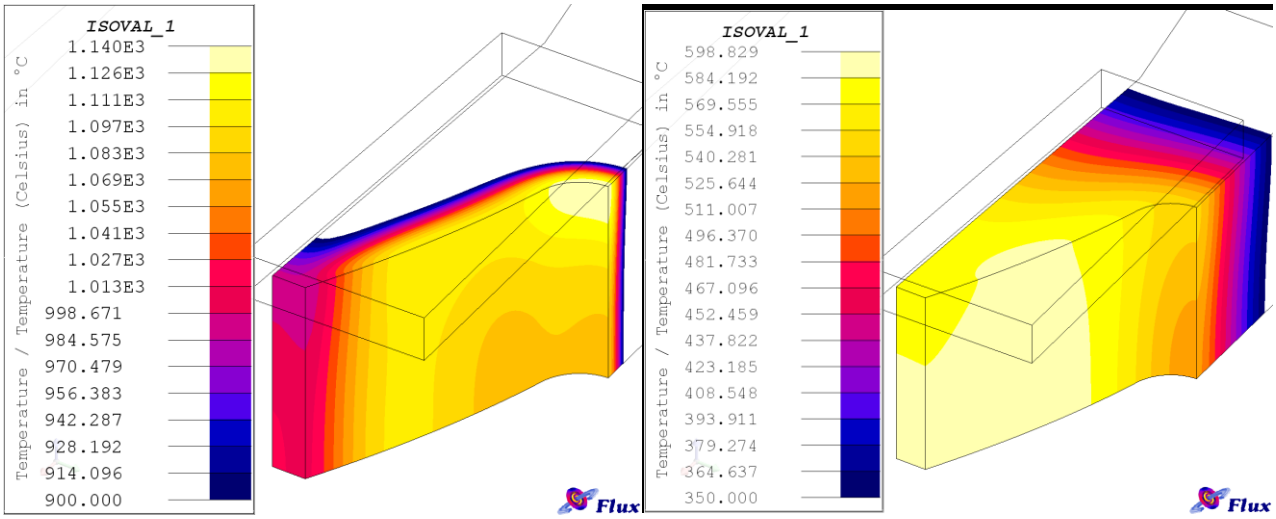

Fig. 4.17 isotherms at the end of HF and MF heating respectively, recipe 5

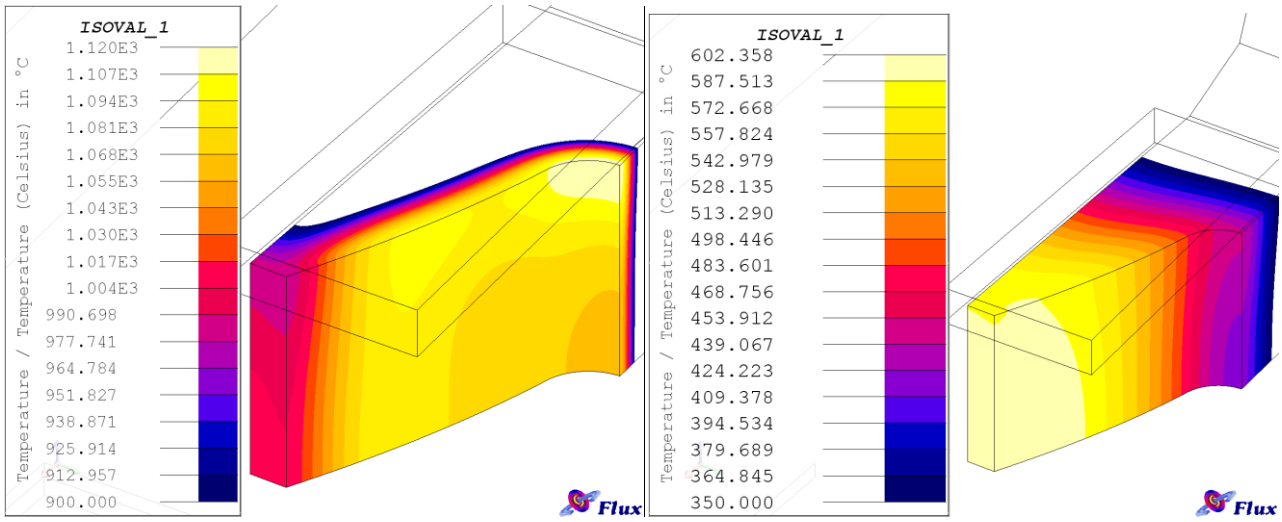

Fig. 4.18 isotherms at the end of HF and MF heating respectively, recipe 6

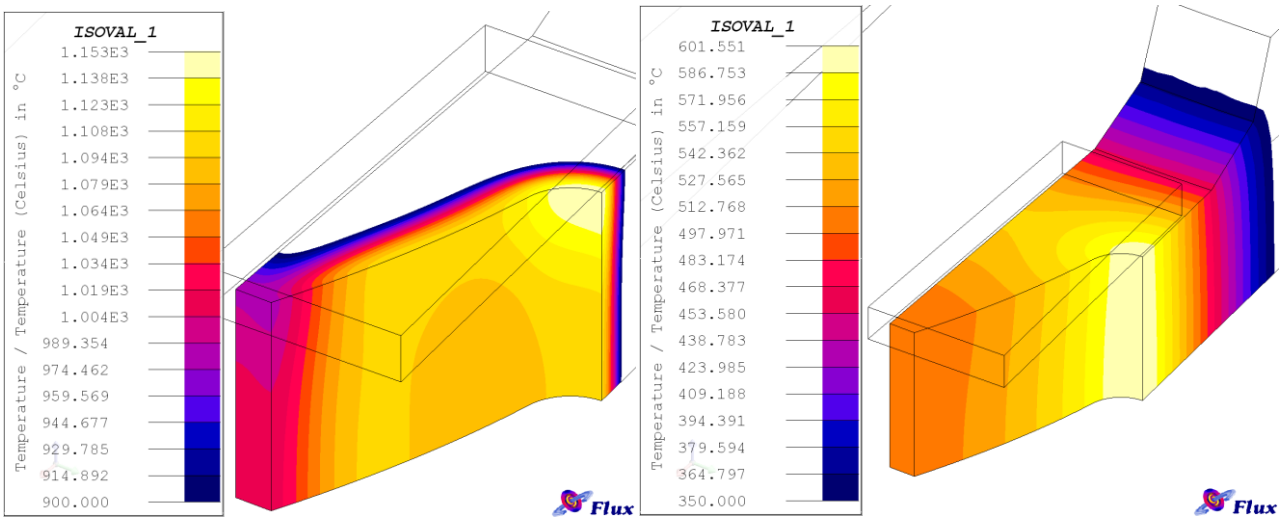

Fig. 4.19 isotherms at the end of HF and MF heating respectively, recipe 7

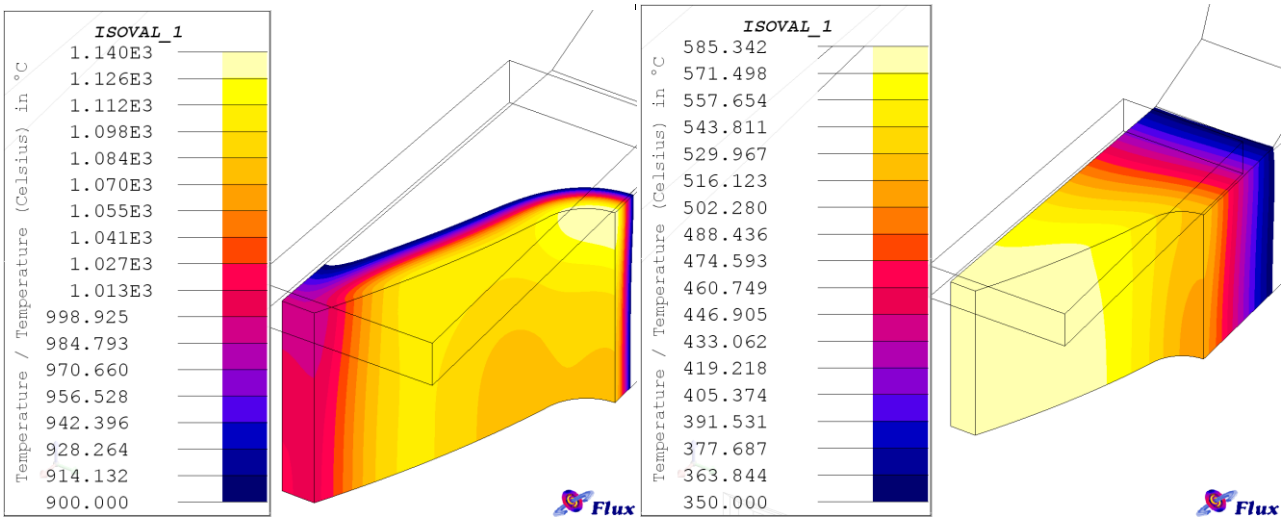

Fig. 4.20 isotherms at the end of HF and MF heating respectively, recipe 8

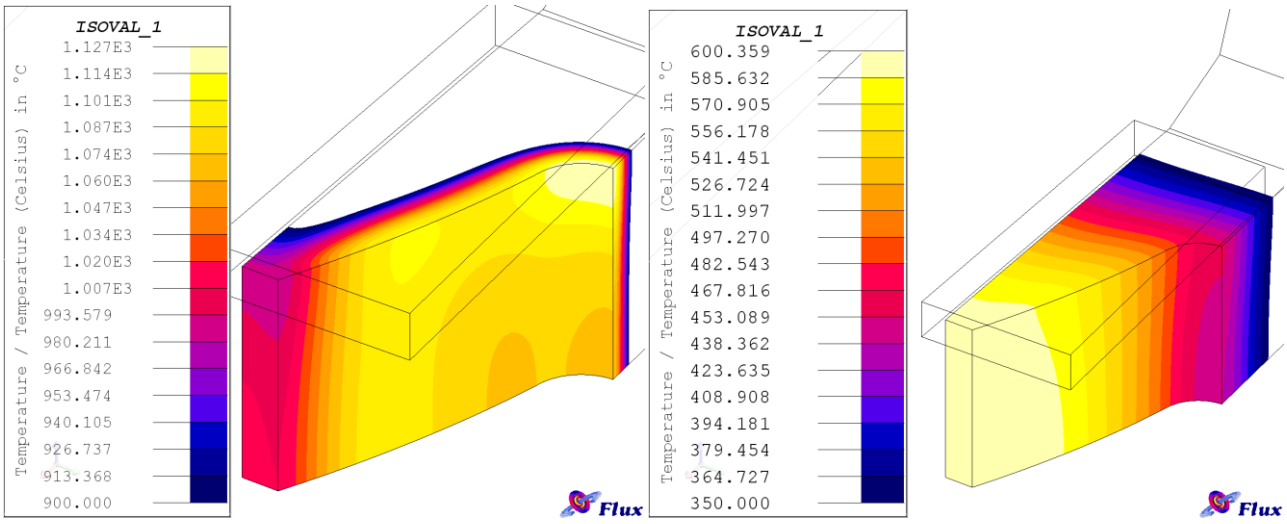

Fig. 4.21 isotherms at the end of HF and MF heating respectively, recipe 9

The chart presented below shows for the nine recipes the depth of the 900°C isotherm in the root and in the tip at the end of HF phase.

Chart 4.2 Depth of the 900°C isotherm

Recipe	900°C depth in the tip		900°C depth in the root	
	SM (mm)	MD (mm)	SM (mm)	MD (mm)
1	0.63	1.15	0.66	0.52
2	1.35	1.57	0.65	0.52
3	1.10	1.35	0.56	0.44
4	1.18	1.48	0.77	0.65
5	1.54	1.69	0.71	0.58
6	1.4	1.59	0.62	0.51
7	1.38	1.57	0.81	0.69
8	1.50	1.65	0.72	0.59
9	1.45	1.62	0.65	0.54

From a first graphical interpretation we can see that at 10000 Hz the longer preheating is, the higher is the temperature in the root at the end of the MF phase. This is certainly due to the fact that the penetration depth at 10000 Hz in the AISI 4340 steel is rather small (0.8 mm), and the induced power is deposited superficially. Therefore heat flows from the tooth towards the root and having longer preheating phase allows the root to be more heated.

Indeed, the more difficult task in induction hardening is to heat the root, from where the heat will flow towards the core of the gear by conduction, despite the fact that inducted power is concentrated in the root. So a preheating that allows the root to reach a higher temperature leads to a more homogeneous hardened profile.

A different behavior is noticed for 1000 Hz preheating. Indeed figures show that the more preheating lasts, the more the heat flows from the root to the other parts of the gear. This is due to the higher penetration depth, that allows to heat directly the root, and longer preheating makes the heat flow in other parts of the gear.

In the 5000 Hz preheating the behavior is between the other two cases.

There are not so many differences between the distribution of temperature of the 9 recipes after HF heating. Nevertheless, we can conclude that a long 1000 Hz preheating would be better in order to obtain an hardened depth in the tooth close to the one in the root, compatibly with the characteristic of the power generator.

4.5 conclusions

It is possible to summarize the obtained results as follows:

- The presence of the flux concentrator over the gear is very important to reduce the edge effect, otherwise difficult to control.
- In both cases of 5 and 10 kHz MF phase, longer preheating (5 s) allows the root to be better heated than shorter preheating.
- Preheating phase with lower frequency (1 kHz rather that 10 kHz) leads to better profile temperature's at the end of HF phase, because the root is better preheated. In this case, longer preheating phase allows the heat to flow also toward the parts adjacent to the root.
- Variations on the dimension of the coil affect the final temperature's distribution. In order to the power to be equally distributed, the height of the coil should not be greater than the height of the gear.

5. Validation of numerical modeling

5.1 Introduction

Due to the complexity of the phenomena involved in the process of induction hardening, it is necessary to introduce several simplifications and approximations in the numerical model, such as in the description of relative magnetic permeability as a function of temperature and magnetic field strength. These simplifications may lead to errors in the distributions of temperature and hence also in the final microstructure of the material of the workpiece.

In this chapter we are going to compare the experimental results of an induction hardening process of a gear with those obtained from simulations, in order to validate the numerical models, and investigate the possibility to use them for the prediction of hardness profile.

5.2 Analysis of experimental procedure

A robust method is used for the measurement of surface temperature fields during fast induction heating.

It is based on the original coupling of temperature indicating lacquers and a high-speed camera system. Image analysis tools have been implemented to automatically extract the temporal evolution of isotherms.

This method allows the full history of surface isotherms to be accurately documented for a 2 s high frequency heating.

Prior to each test, the upper side of the spur gear was coated with a specific temperature indicating lacquer. Such lacquers contain chemicals in suspension that transform or evaporate at given temperatures, with an accuracy of ± 1% of the indicated temperature. A high-speed camera is set 25 cm above the gear by means of a tripod. The magnification is adjusted so that two teeth are observed within the camera's field of view. The gear is lightened up enough for the lacquer coating to appear uniform.

The camera records 512*352 pixels images at a frame rate of 2000 images per second. A typical image is shown in figure 5.1.

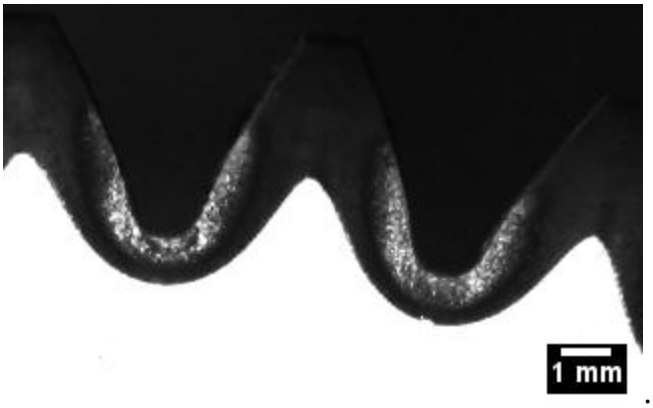

Fig. 5.1 Typical Image of the acquisition.

The induction heating treatments were performed using a single turn coil on a dual simultaneous MF and HF frequencies generator designed by EFD Induction. The coil has a 110-mm inner diameter and a 8-mm thickness.

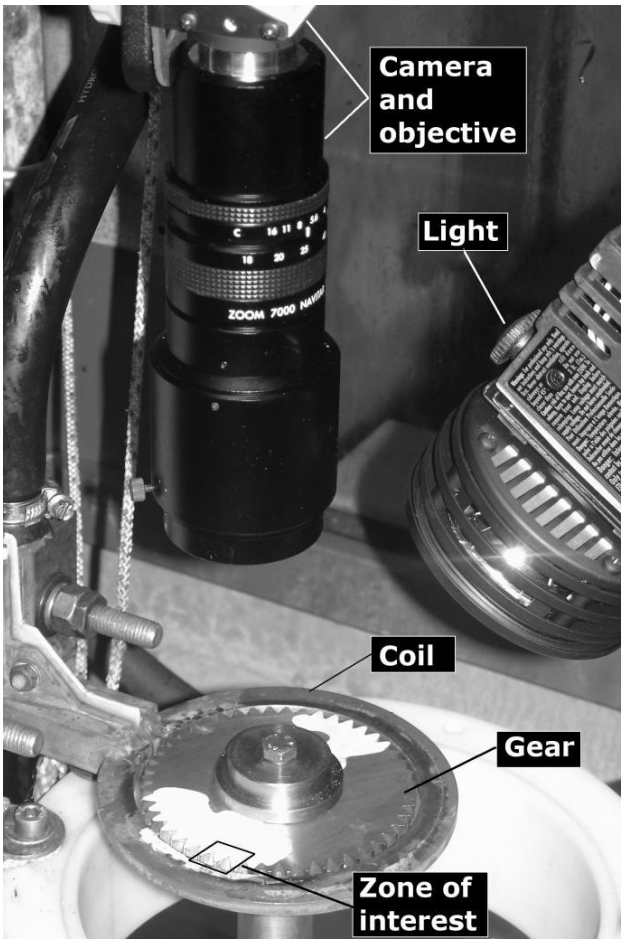

Fig. 5.2 Experimental setting.

A final air cooling without rotating the gear is expected.

A full characterization of the temperature evolution versus time has been conducted at the surface of 2 teeth of the gear heated by 2 s HF heating at 45 kW and then cooled in air.

Two isotherms, 816^0C, and 927^0C, were acquired every 0.3 ms with a spatial resolution of 0.045 mm per pixel.

5.3 Numerical simulation

A steady-state AC Magnetic 3D with Thermal Transient model of the gear has been built in FLUX 3D, following the method proposed in chapter three.

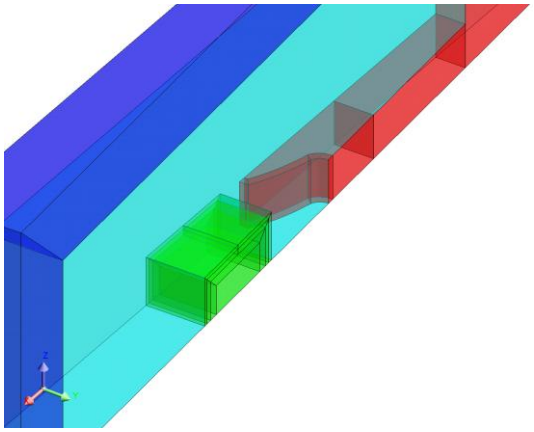

Fig. 5.3 Model of the gear in FLUX 3D

It has been chosen to build a mapped mesh 0.5 mm depth on the tooth profile and in the external part of the inductor, due to the value of skin depth at 190000 Hz

$$\delta_{AISI4340,190000} = \sqrt{\frac{2 \cdot \rho}{\omega \cdot \mu_r \cdot \mu_0}} = 0.18\ mm$$

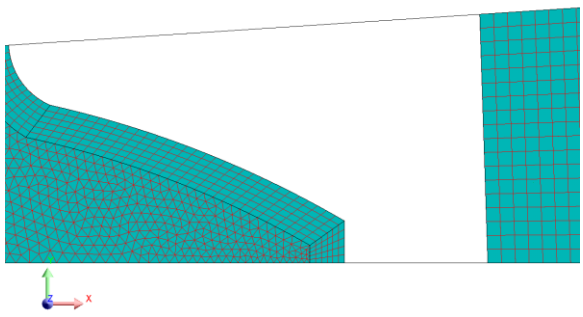

Fig. 5.4 mesh used in the model

Four different simulations have been considered, in order to understand the influence of the material's properties on the temperature distribution:

- **Recipe 1:** A value of $\mu_{r20} = 10$ has been considered. The variation of the relative magnetic permeability is shown in figure 5.5.

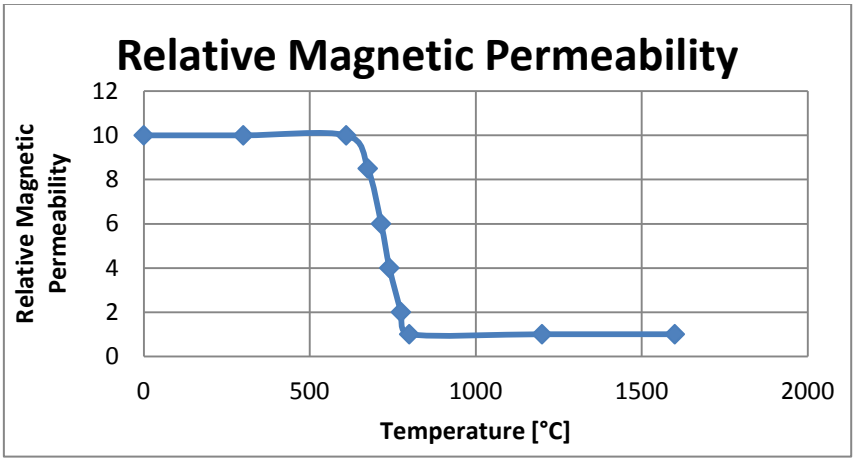

Fig. 5.5 Relative magnetic permeability trend in recipe 1

The trend of specific heat as a function of temperature is the one you can find in literature, and it does not take into account the variation of the temperature Ac1 and Ac3 as a function of the heating rate.

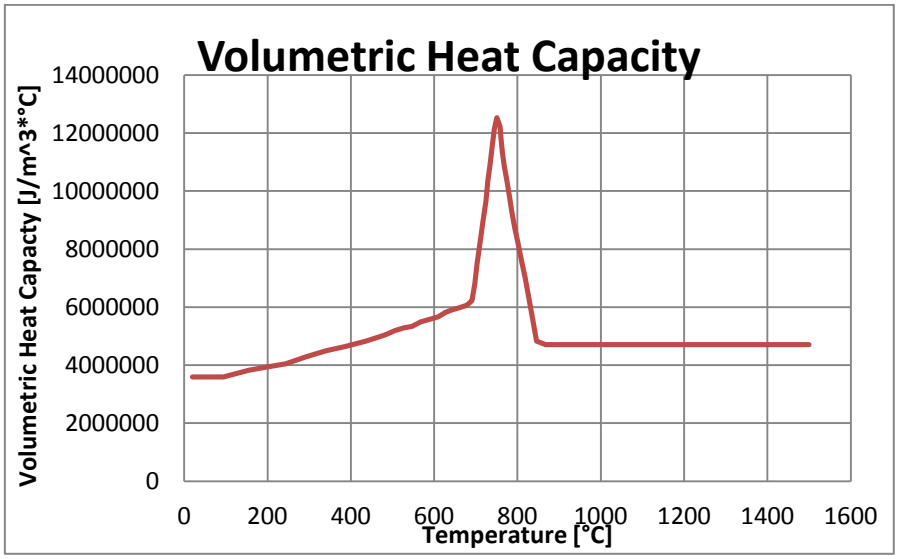

Fig. 5.6 Volumetric heat capacity trend in recipe 1

- **Recipe 2:** The second simulation has been done by keeping the same volumetric heat capacity trend of the first simulation, and considering the $\mu_{r20} = 3$, according with figure 5.7.

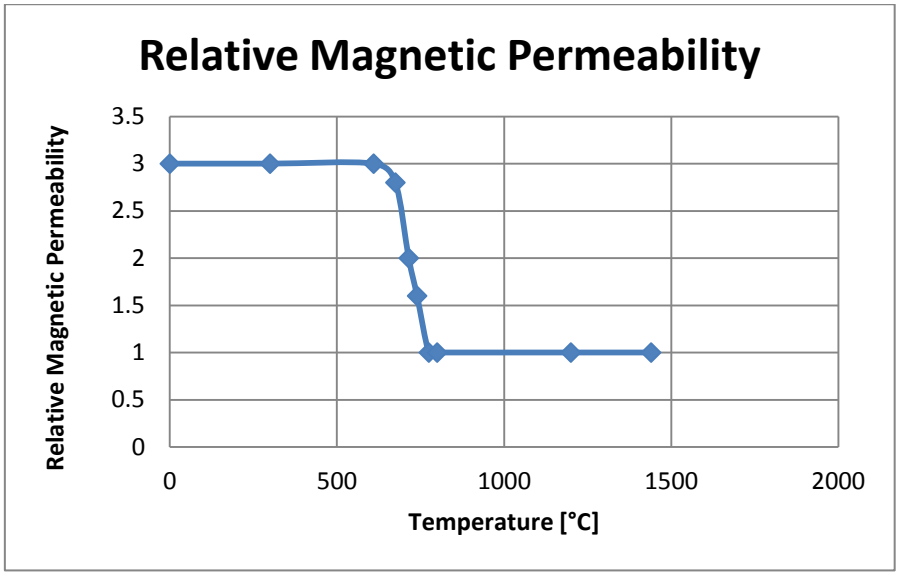

Fig. 5.7 Relative magnetic permeability trend on recipe 2

- **Recipe 3:** In the third simulation the value of μ_{r20} was kept at 10 while the trend of the volumetric heat capacity presents a shifted latent heat peak, considering increased Ac1 and Ac3 temperatures, 760°C and 960°C respectively.

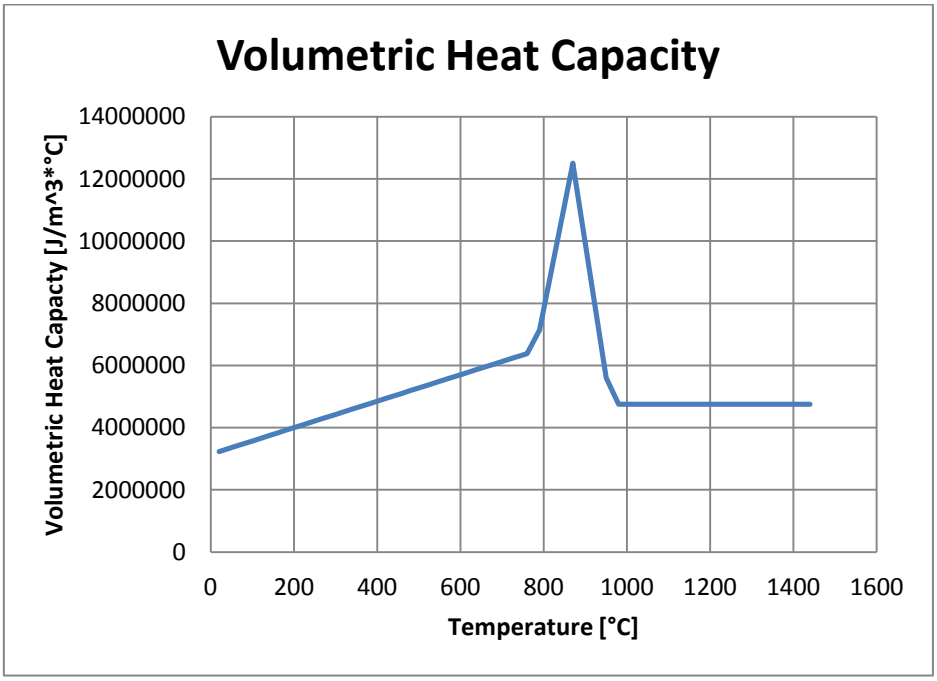

Fig. 5.8 Volumetric heat capacity trend on recipe 3

- **Recipe 4:** In this recipe the value of μ_{r20} was kept equal to 3 and the latent heat peak was shifted as in recipe 3.

5.4 Comparison between experimental and numerical result: Isotherm's evolution

The first step in the validation of numerical models was the analysis of the isotherm's evolution. The simplest recipe of induction hardening has been considered (2 s HF), i.e. without preheating or double frequency hardening in order to avoid the influence of other parameters. Indeed no lower temperature lacquers have been used in the experimental procedure.

In the development of the numerical models, the power has been calibrated by considering the 816 ° C's isotherm depth in the root of the gear equal to the experimental one at the end of the 2 s HF.

Here images of the gear are shown at different time steps of the heating phase, for each of the four recipes.

T=2 s

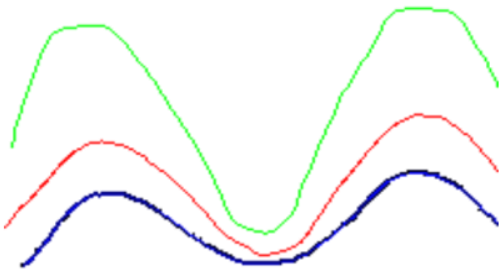

Fig. 5.9 sights of experimental isotherms

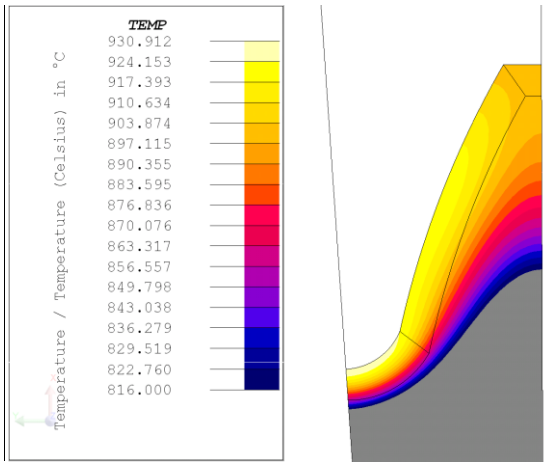

Fig. 5.10 simulated isotherms, $\mu_r = 10$

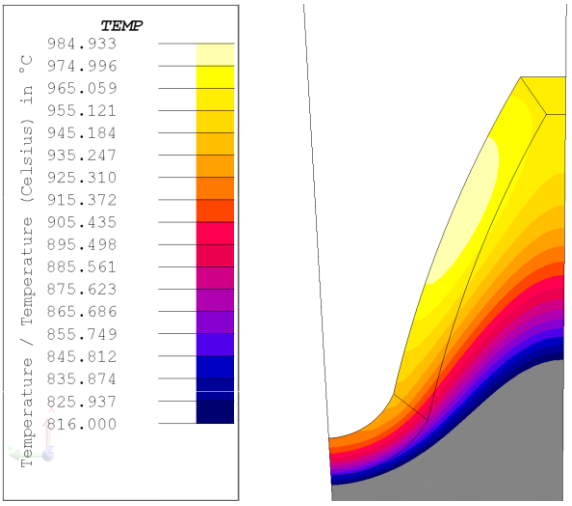

Fig. 5.11 simulated isotherms, $\mu_r = 3$

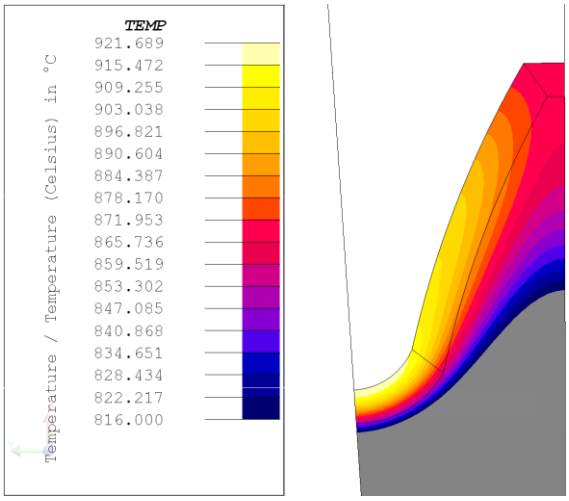

Fig. 5.12 simulated isotherms, $\mu_r = 10$, shifted latent heat peak

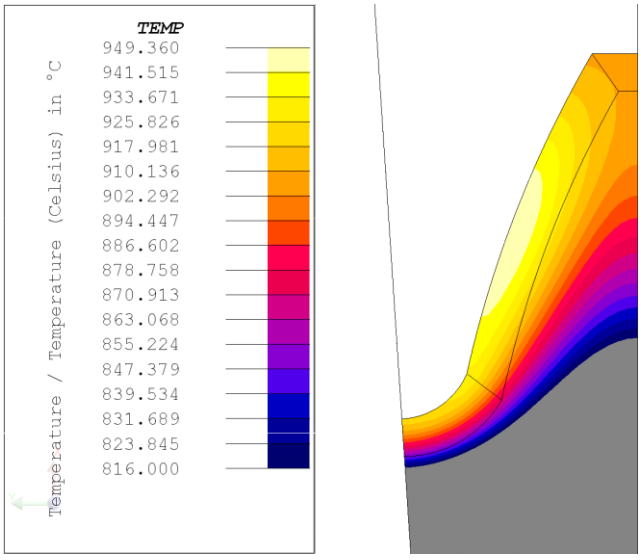

Fig. 5.13 simulated isotherms, $\mu_r = 3$, shifted latent heat peak

T=1.92 s

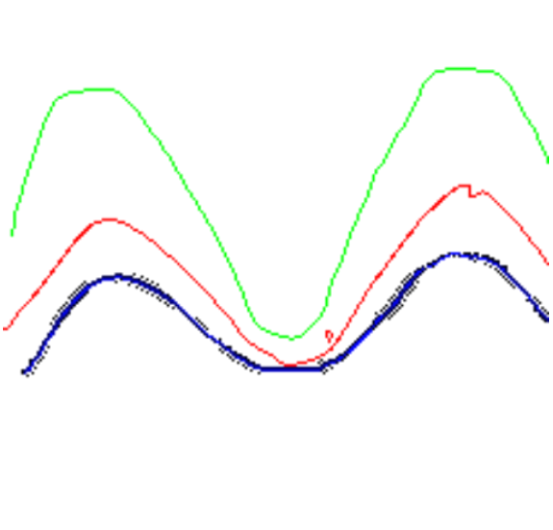

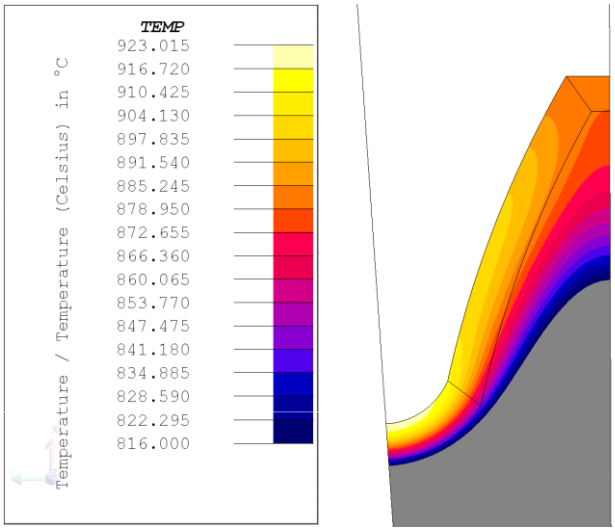

Fig. 5.14 sights of experimental isotherms

Fig. 5.15 simulated isotherms, $\mu_r = 10$

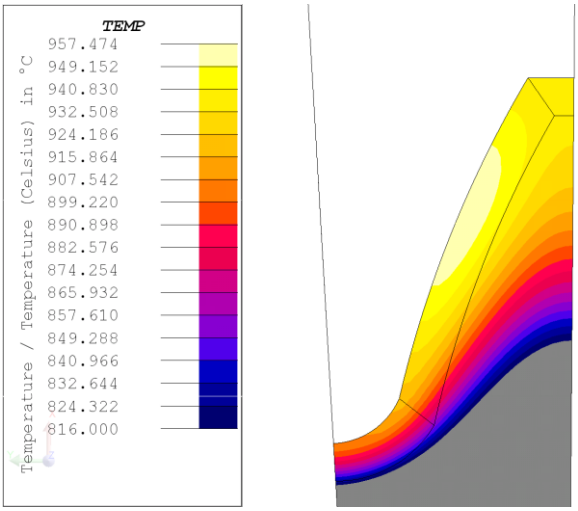

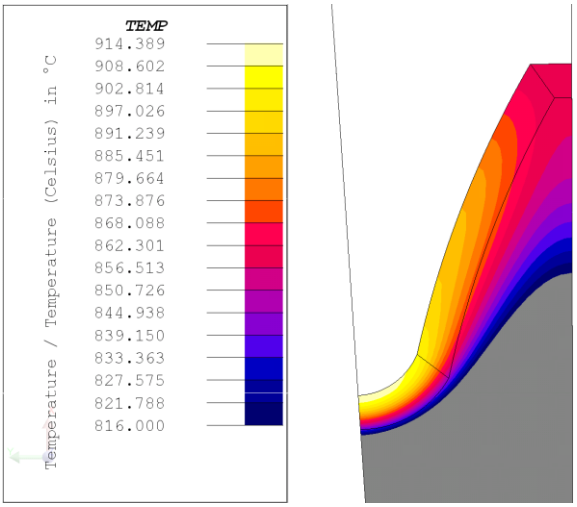

Fig. 5.16 simulated isotherms, $\mu_r = 10$ **Fig. 5.17** simulated isotherms, $\mu_r = 10$, shifted latent heat peak

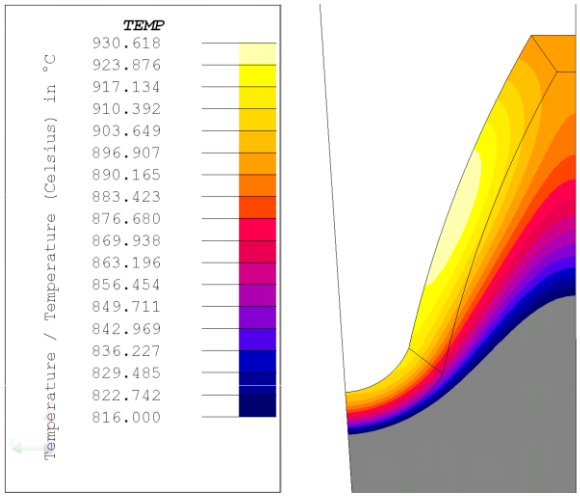

Fig. 5.18 simulated isotherms, $\mu_r = 3$, shifted latent heat peak

T=1.86 s

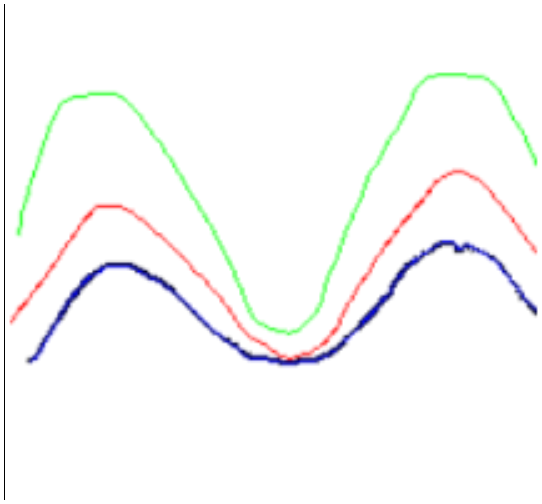

Fig. 5.19 sights of experimental isotherms

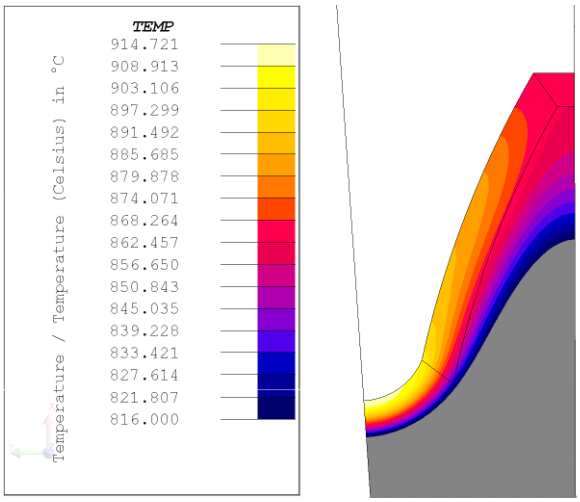

Fig. 5.20 simulated isotherms, $\mu_r = 10$

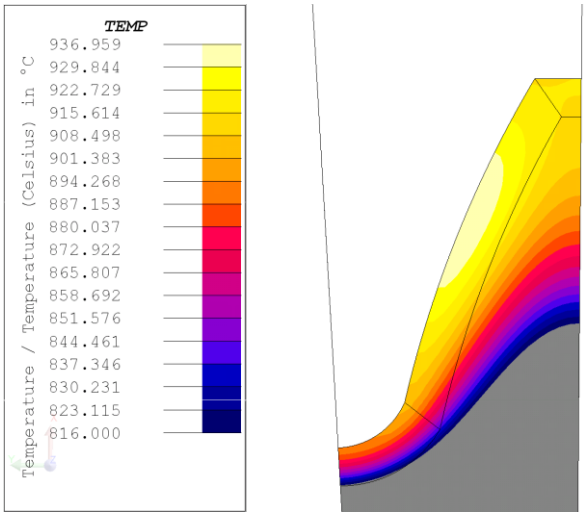

Fig. 5.21 simulated isotherms, $\mu_r = 3$

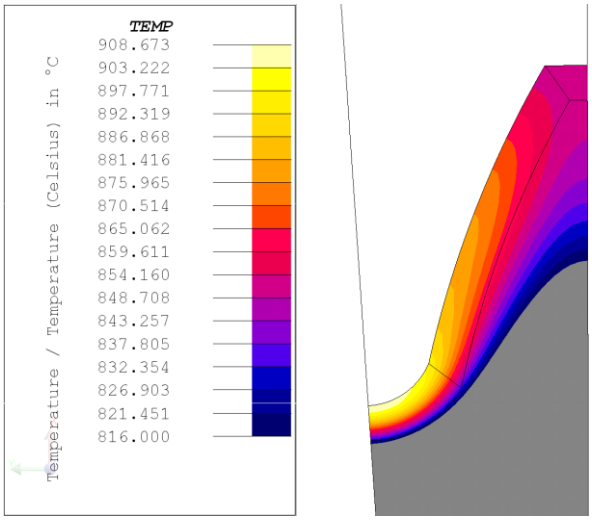

Fig. 5.22 simulated isotherms, $\mu_r = 10$, shifted latent heat peak

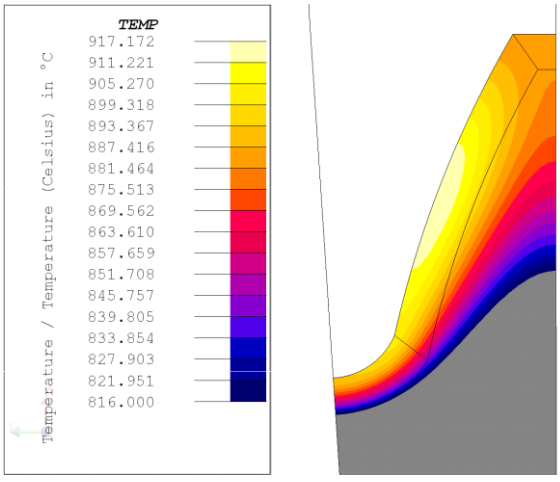

Fig. 5.23 simulated isotherms, $\mu_r = 3$, shifted latent heat peak

T=1.80 s

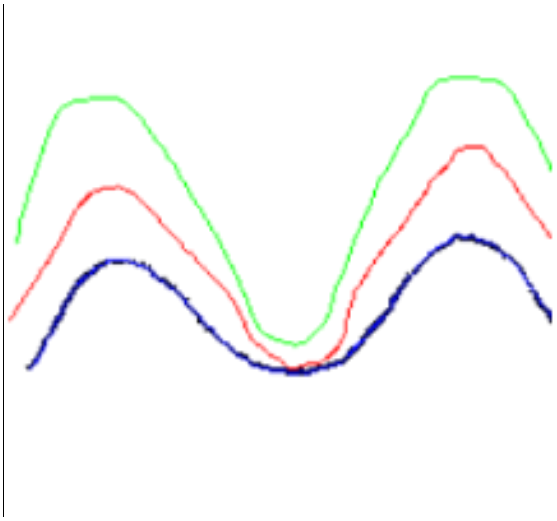

Fig. 5.24 sights of experimental isotherms

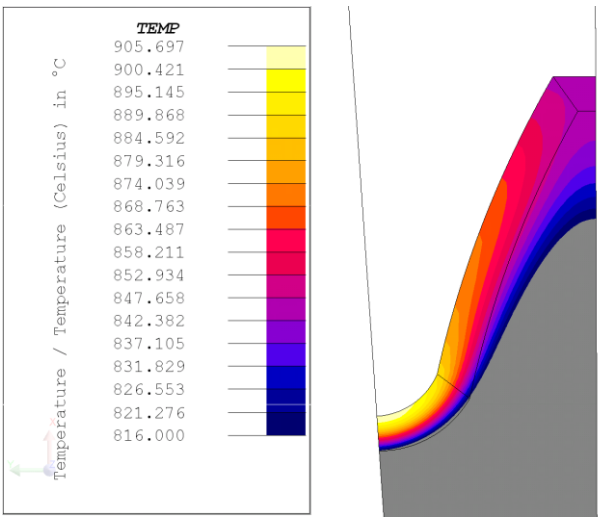

Fig. 5.25 simulated isotherms, $\mu_r = 10$

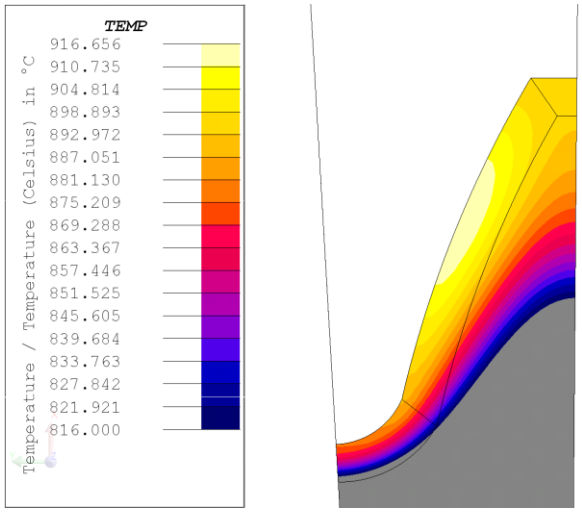

Fig. 5.26 simulated isotherms, $\mu_r = 3$

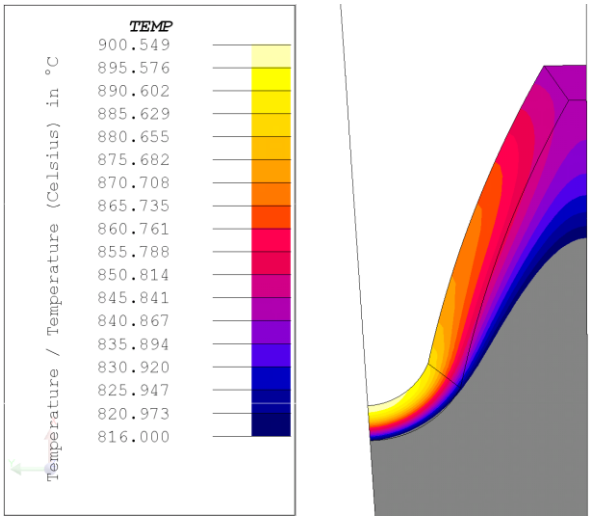

Fig. 5.27 simulated isotherms, $\mu_r = 10$, shifted latent heat peak

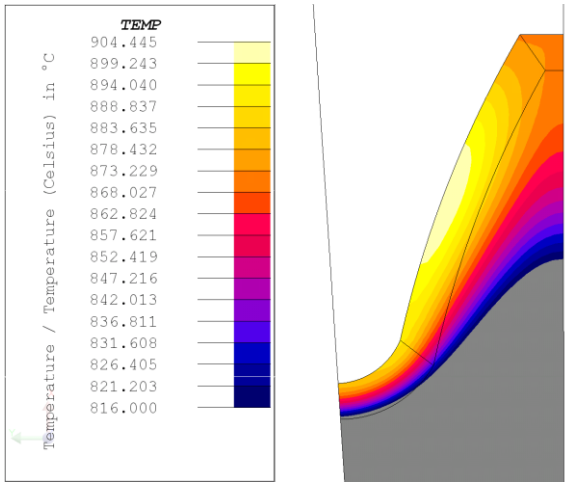

Fig. 5.28 simulated isotherms, $\mu_r = 3$, shifted latent heat peak

T=1.74 s

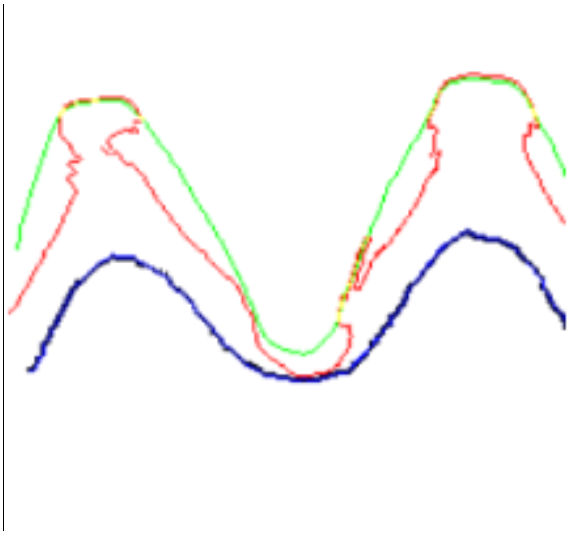

Fig. 5.29 sights of experimental isotherms

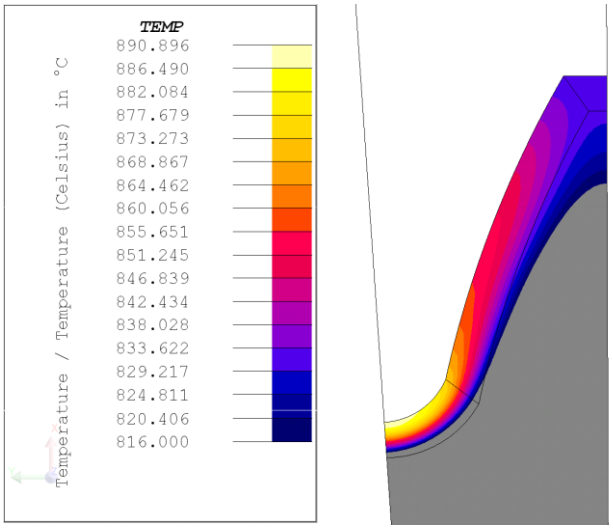

Fig. 5.30 simulated isotherms, $\mu_r = 10$

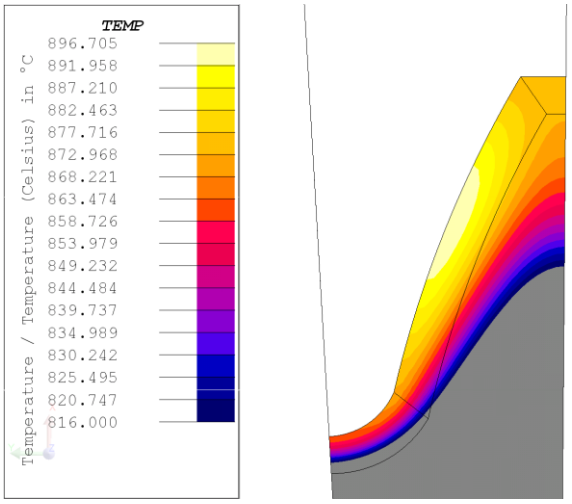

Fig. 5.31 simulated isotherms, $\mu_r = 3$

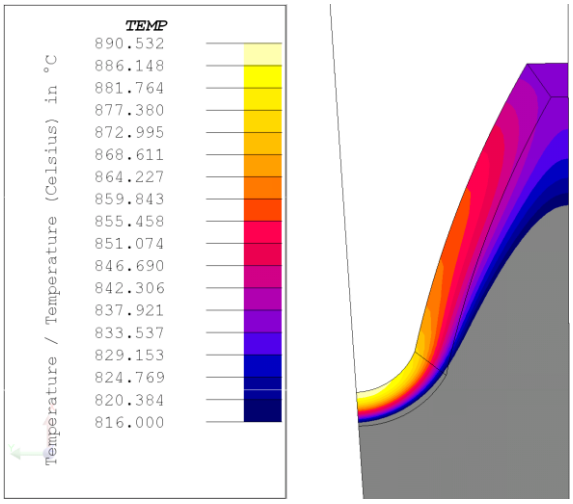

Fig. 5.32 simulated isotherms, $\mu_r = 10$, shifted latent heat peak

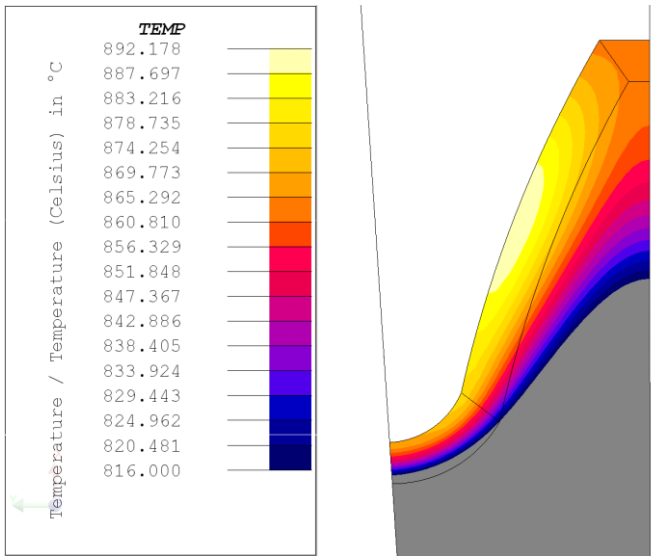

Fig. 5.33 simulated isotherms, $\mu_r = 3$, shifted latent heat peak

T=1.70 s

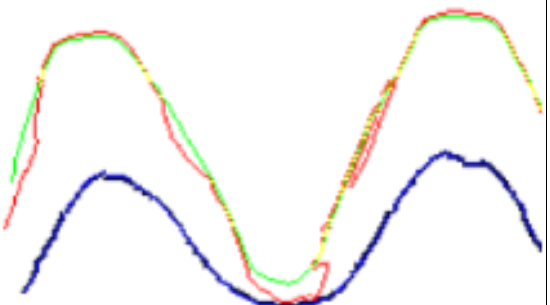

Fig. 5.34 sights of experimental isotherms

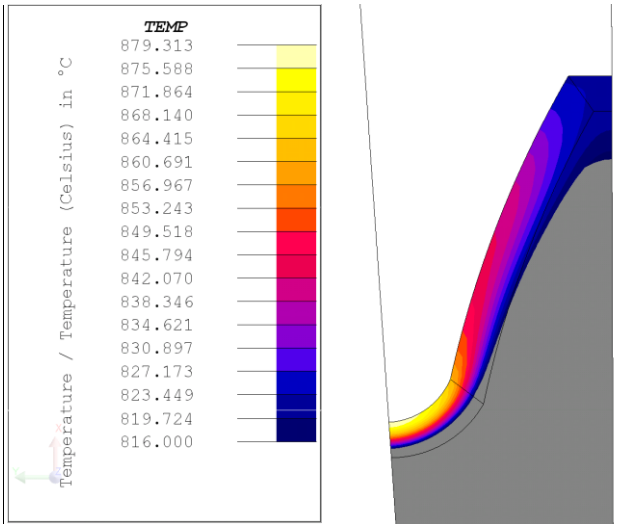

Fig. 5.35 simulated isotherms, $\mu_r = 10$

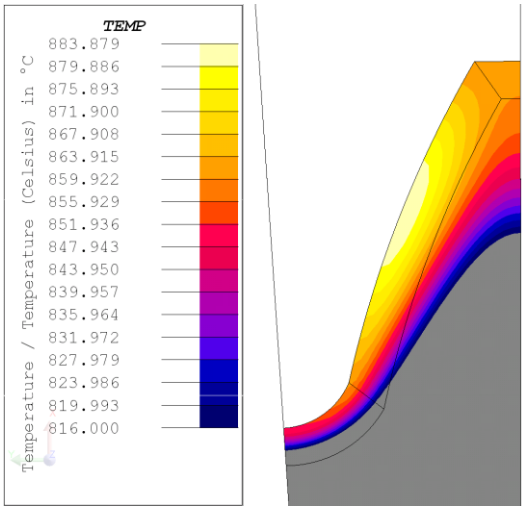

Fig. 5.36 simulated isotherms, $\mu_r = 3$

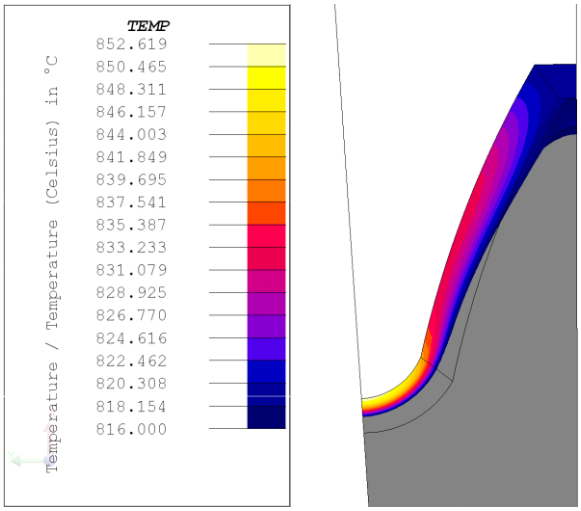

Fig. 5.37 simulated isotherms, $\mu_r = 10$, shifted latent heat peak

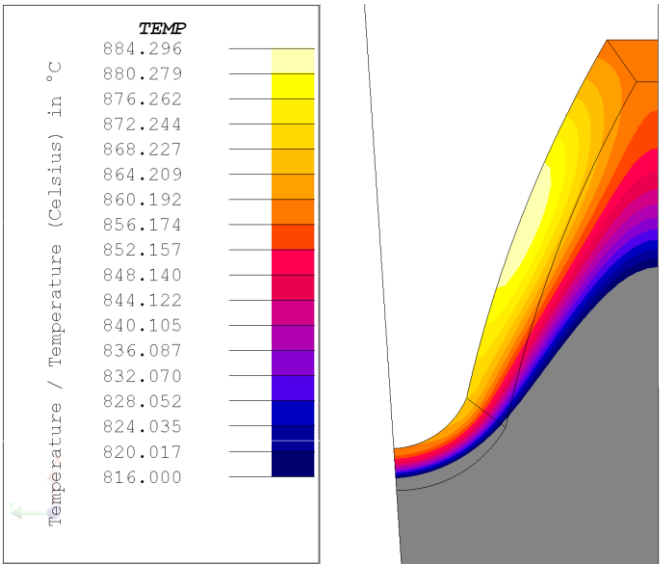

Fig. 5.38 simulated isotherms, $\mu_r = 3$, shifted latent heat peak

T=1.60 s

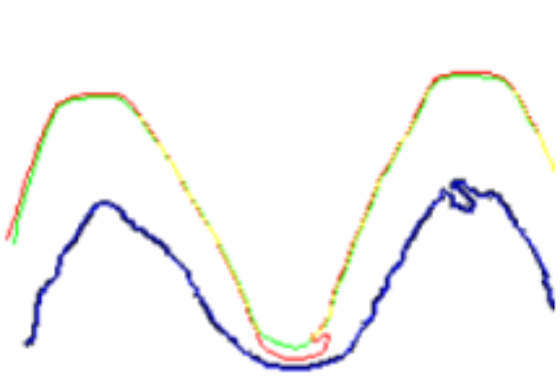

Fig. 5.39 sights of experimental isotherms

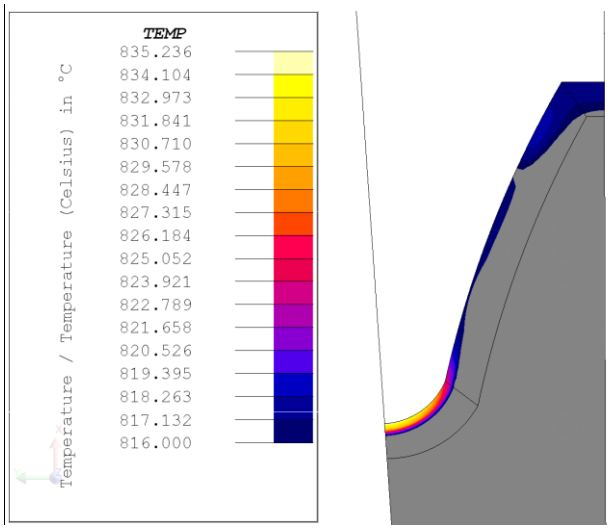

Fig. 5.40 simulated isotherms, $\mu_r = 10$

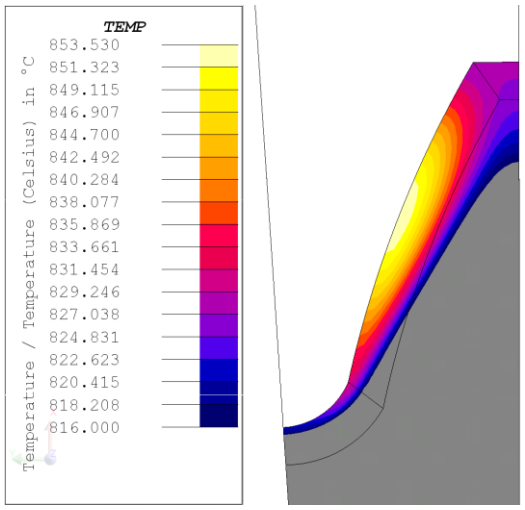

Fig. 5.41 simulated isotherms, $\mu_r = 3$

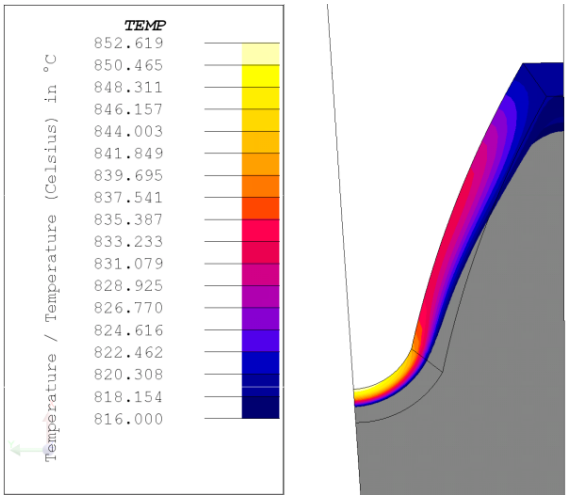

Fig. 5.42 simulated isotherms, $\mu_r = 10$, shifted latent heat peak

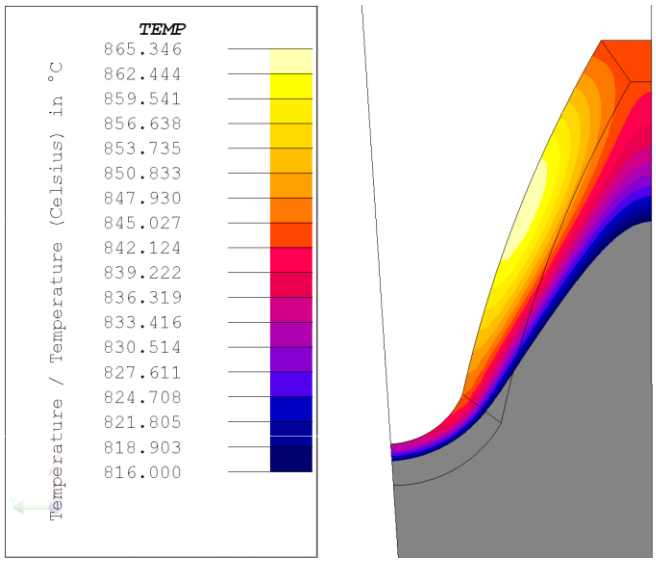

Fig. 5.43 simulated isotherms, $\mu_r = 3$, shifted latent heat peak

T=1.50 s

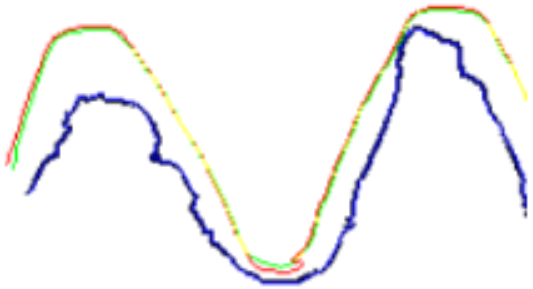

Fig. 5.44 sights of experimental isotherms

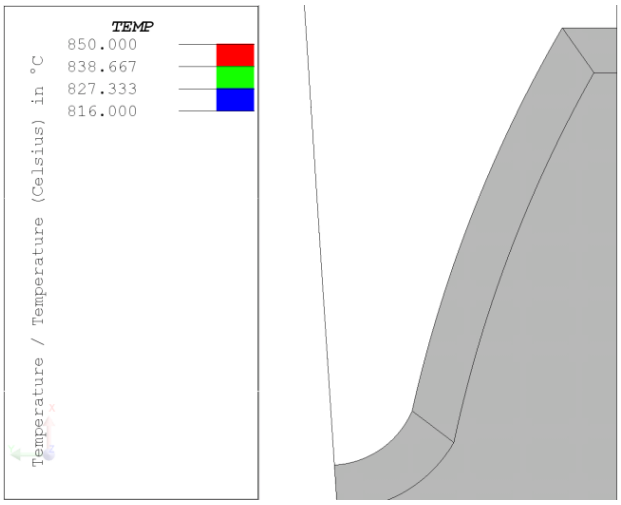

Fig. 5.45 simulated isotherms, $\mu_r = 10$

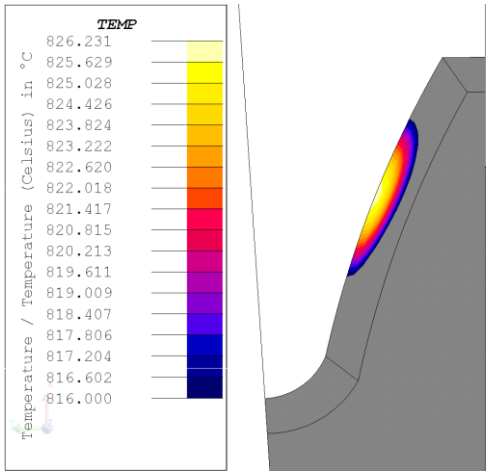

Fig. 5.46 simulated isotherms, $\mu_r = 3$

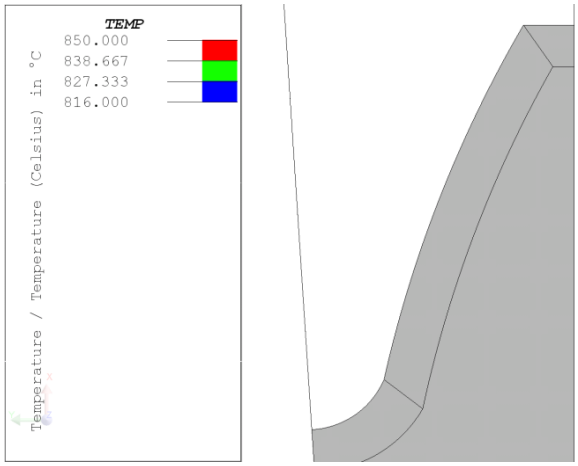

Fig. 5.47 simulated isotherms, $\mu_r = 10$, shifted latent heat peak

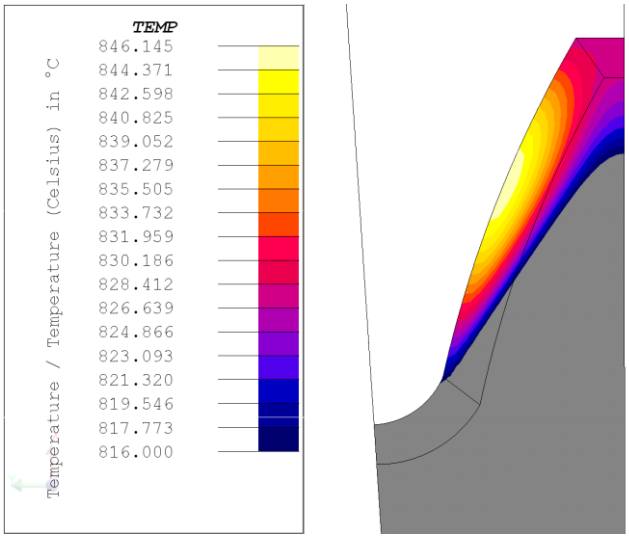

Fig. 5.48 simulated isotherms, $\mu_r = 3$, shifted latent heat peak

T=1,35 s

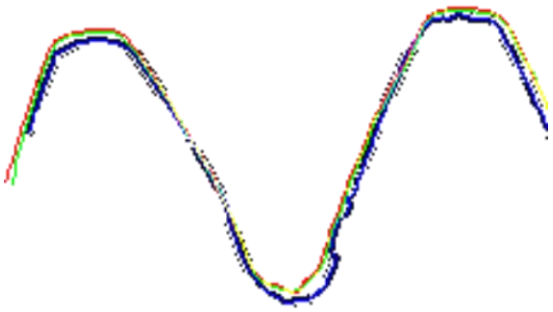

Fig. 5.49 sights of experimental isotherms

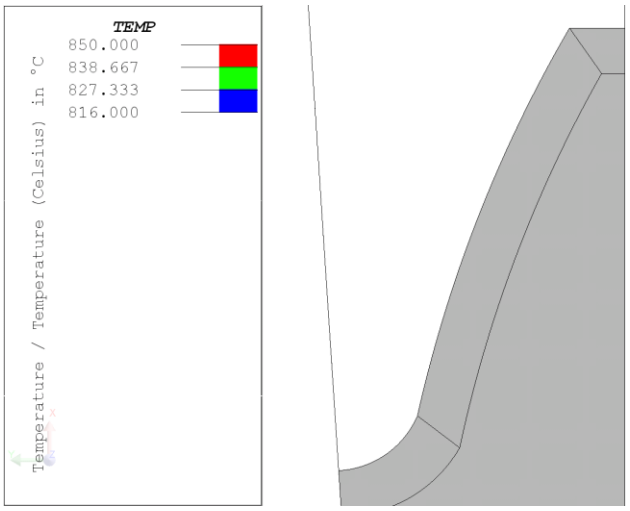

Fig. 5.50 simulated isotherms, $\mu_r = 10$

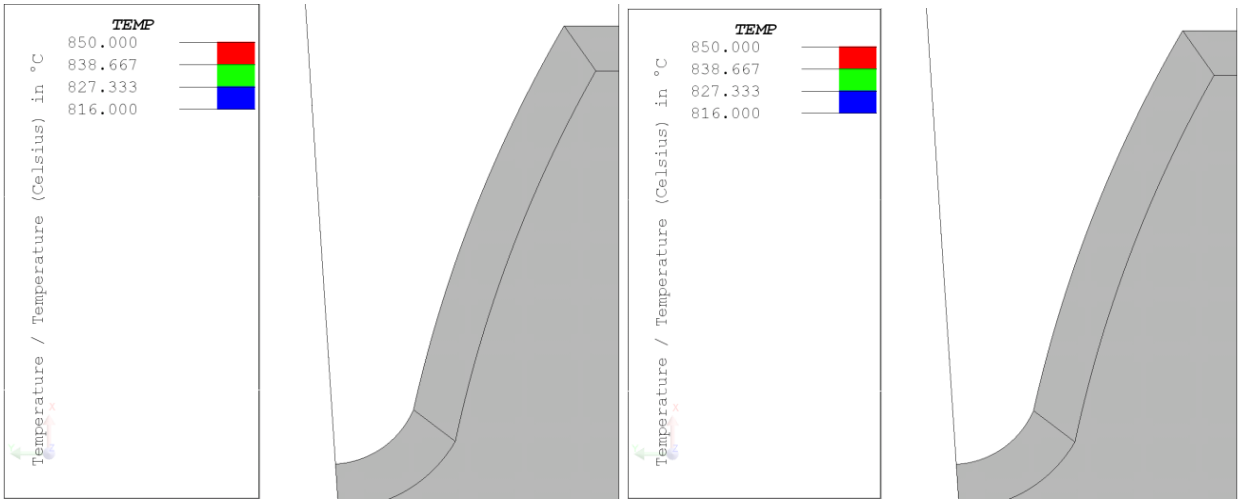

Fig. 5.51 simulated isotherms, $\mu_r = 3$ **Fig. 5.52** simulated isotherms, $\mu_r = 10$, shifted latent heat peak

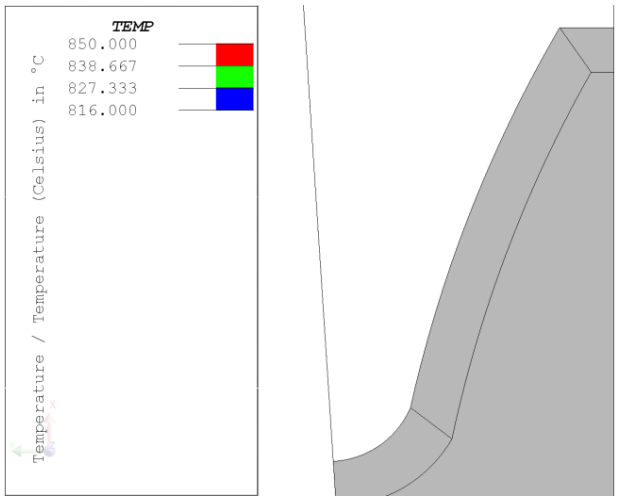

Fig. 5.53 simulated isotherms, $\mu_r = 3$, shifted latent heat peak

After the first graphical evaluation it is important to consider the actual depth of the two isotherms considered. For this reason the isotherm's depth has been reported in the following graphs for the different time steps, for all the three recipes.

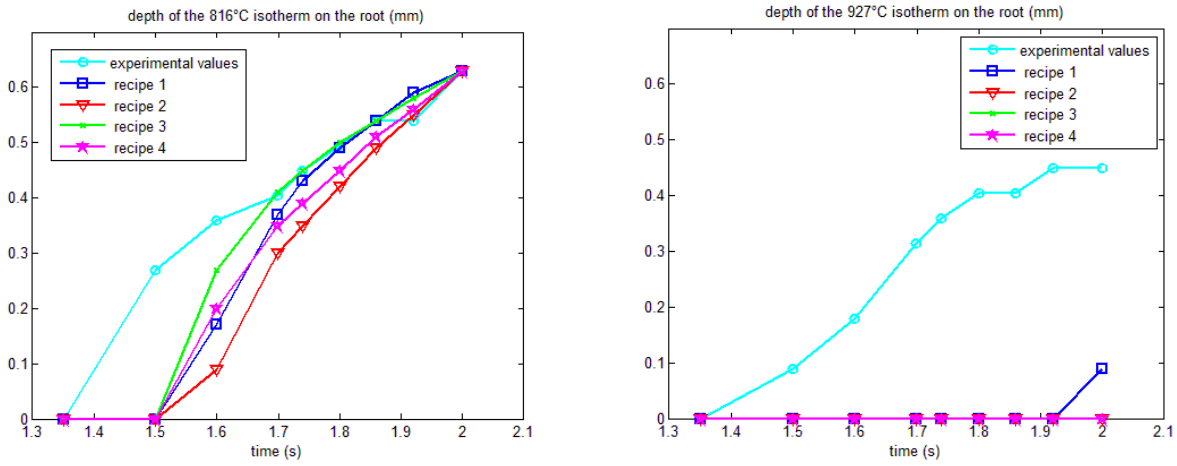

Fig. 5.54 depth of the 816°C and 927°C isotherms on the root of the gear.

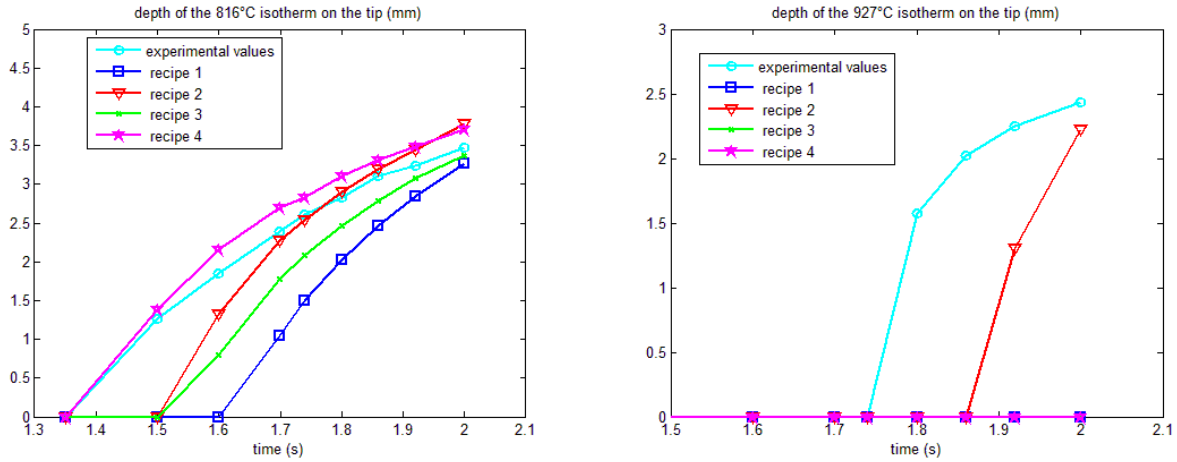

Fig. 5.55 depth of the 816°C and 927°C isotherms on the tip of the gear

Observations

A qualitative analysis of the evolution of the experimental isotherms highlights the fact that the temperature rises first at the root (fig. 5.39). Then, there is another starting point of the same isotherm in the flank of the tooth (fig. 5.34) and subsequently it continues growing until reaching the isotherm on the other flank of the tooth.

Consequently, despite the fact that HF heating is known to heat the nearest parts of the tooth to the coil, i.e., the tooth tip, the present method allowed to originally identify three heating steps of

temperature evolution during HF heating: temperature increases first at the tooth root, then along the edge of the active profile, and finally in the rest of the tooth surface.

The comparison between experimental and simulated results shows that

- In the recipes 1 ($\mu_r = 10$), 3 ($\mu_r = 10$ and shifted latent heat peak) and 4 ($\mu_r = 3$ and shifted latent heat peak) the 927°C isotherm doesn't appear at all (fig. 5.54 and fig. 5.55), except a little in the root for recipe 1. This represent the greatest difference between the results of numerical models and the experimental ones. It is supposed to be due to the possible too high value of latent heat peak. Unfortunately there are no data in literature about volumetric heat capacity in non-equilibrium conditions.
- There is a delay in the appearance of the simulated isotherms as clearly shown in figure 5.54 and 5.55, for all the recipes considered except the fourth in the tip. This delay could be due to the fact that in the simulation the power is not constant during heating, since voltage control was carried out (fig. 5.56).

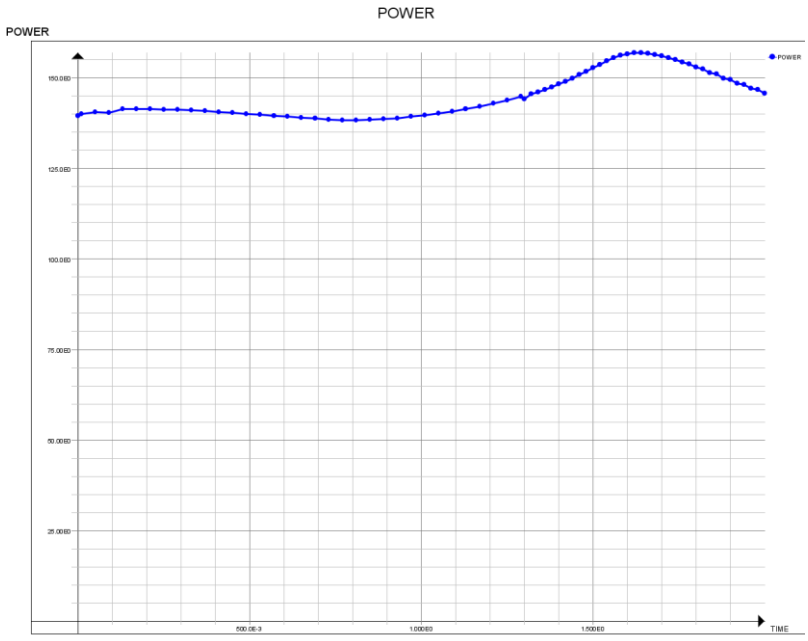

Fig. 5.56 power dissipated on the gear and in the coil

Power increases of about 5% of the initial value at about 1.3 s.

This in addition to the possible too high value of latent heat peak.

- Looking at figure 5.55 we can see that considering $\mu_r = 3$ as in recipe 2 and 4 we obtain a little overestimation in the depth of 816° isotherm in the tip of the root. Moreover, having a glance for example at figure 5.46 and 5.48 we can see that isotherms do not start from the root as in the real case. Nonetheless the 927°C isotherm is not so deep in the tip as it should, and in the root it doesn't appear at all (fig. 5.54 and 5.55).

- For recipe 1 and 3, i.e. both with $\mu_r = 10$, there is good agreement between the experimental 816°C isotherm and the simulated ones in the tip at the end of the heating (fig. 5.55). However in recipe 3 which has a shifted latent heat peak the evolution of the 816°C isotherm better approaches the real one, since it appears before than in recipe 1 and as we can see from fig. 5.42, isotherms grow also from the flank of the tooth.

5.5 Comparison between experimental and numerical results: The edge effect

It is important to remember that the method proposed in the previous chapter just compares the evolution of the isotherms seen from above the gear, according to the position of the high speed camera. Therefore it is not possible to make considerations on the truthfulness of the simulations about the depth of the isotherms within the tooth.

It is well known that the extern of the gear is overheated than the inside because of the edge effect. This is due to the magnetic field lines, that tend to close within the gear.

In order to know if simulations well predict the edge effect it is possible to consider the hardened depth on the profile section in the root and in the tip respectively.

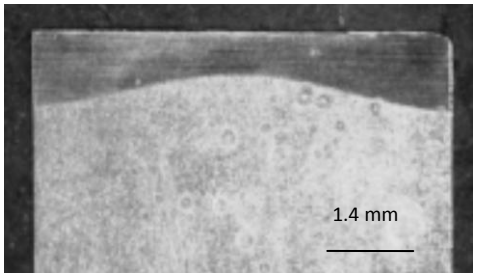

Fig. 5.57 hardened profile section on the root

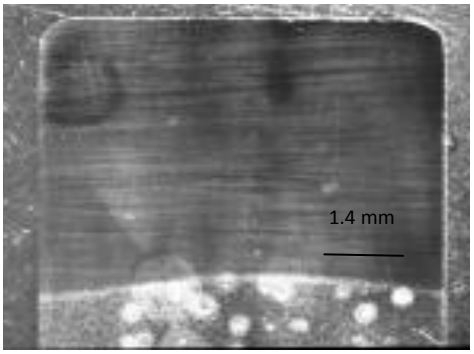

Fig. 5.58 hardened profile section on the tip

Chart 5.1 numerical value of hardened depth on the tip and on the root of the gear

	Top	Middle	$\frac{\text{(Hardened depth on the middle)}}{\text{(hardened depth on top)}}\%$
Hardened depth on tip (mm)	5.08	4.78	94%
Hardened depth on root (mm)	1.15	0.75	65%

These data highlights the fact that despite the edge effect, the centre of the gear is hardened, even if in minor depth.

We can observe that the hardened depth is deeper than the 816°C isotherm at the end of the heating phase, as shown in chart 5.1. This could be due to the fact that the Ac3 temperature is lower than 816°C, and even because the 816°C isotherm increases a few its depth on the tip by conduction once the heating phase is ended i.e. T=2 s.

Chart 5.2 Depth of 816°C isotherm from experimental data

	Root	Tip
Depth of the 816°C isotherm at T=2 s (mm)	0.63	3.46
Depth of the 816°C isotherm at T=2.66 s	0.63	3.65

In order to obtain an hypothetical value of hardened depth from the simulated results, the temperature in the root has been calculated at the same depth of the actual hardened layer. Then, the depth reached by that temperature in the tip has been calculated. It is important to remember that this procedure is just a rough approximation since it doesn't take into consideration the different heating rate in the different parts of the gear. The results of all the four recipes are reported in chart 5.3.

Chart 5.3 Results for the evaluation of the edge effect

	Recipe 1	Recipe 2	Recipe 3	Recipe 4
Temperature at 1.15 mm depth on the root top (°C) (T.D.R)	686	690	689	698
Depth reached by T.D.R on the root middle (mm)	0.61	0.71	0.68	0.74

$\frac{\text{Depth reached by T. D. R. on the root middle (mm)}}{1.15\ (mm)}\%$	53%	62%	59%	64%
Depth reached by T.D.R. on the tip top	4.82	5.02	4.94	5.04
Depth reached by T.D.R. on the tip middle	4.30	4.66	4.53	4.76
$\frac{\text{Depth reached by T. D. R. on the tip middle}}{\text{Depth reached by T. D. R. on the tip top}}\%$	89%	93%	92%	94%

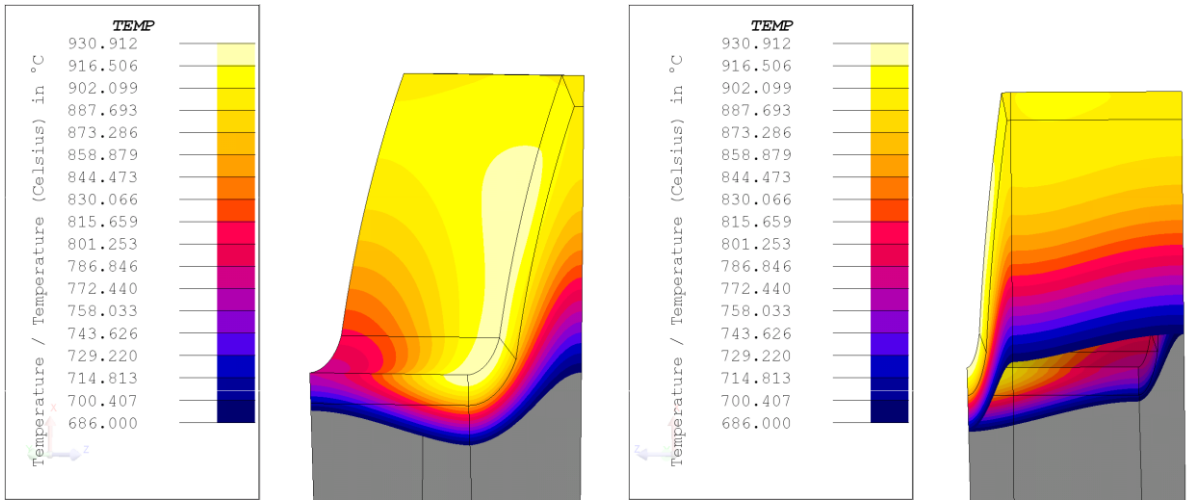

Fig. 59 Hypothetical hardened depth for recipe 1

Observations:

What the chart shows is that the edge effect is lightly overestimated in the simulations. Indeed, in all the four recipes the ratio between the hypothetical hardened depth on the top and the hypothetical hardened depth on the middle is lower than in the actual case (chart 5.3). It is important to highlight that a final air cooling was done in the experimental phase and hence diffusion may helps to increase the hardened depth in the middle of the gear.
In particular considering higher values of μ_r in the numerical model, the edge effect results enhanced, while it results reduced considering a shifted latent heat peak.

It is very important to observe that the temperature obtained at 1.15 mm in the top of the root (chart 5.3) is far from the actual Ac3 temperature, for all the four recipes. Indeed, considering a heating

rate of about 500°C/s for the hardened layer, Ac3 temperature should be higher. Recalling the comparison made in the first part of this study, there is a delay in the appearance of the simulated isotherms (figure 56 and 57). Thus, the real Ac3 temperature isotherm probably appears on delay too, showing us a lower temperature. Moreover, after the end of the HF heating, the heat surely flows toward the centre of the gear by conduction. Therefore this study doesn't compare the real hardened depth but allows us to estimate the edge effect in a numerical model.

5.6 Conclusions:

Once we have been studying the differences between numerical models and experimental results, we can conclude that even if the present work provides a promising tool to validate simulation models, it is difficult to properly estimate the evolution of the temperature profiles during the induction hardening of a real gear. As a matter of fact, if one calibrate the model in order to have an accurate temperature at a given depth for a given time, the temperature profiles tend to not be accurate at other locations, nor at other times. On the other hand simulation well predicts the intensity of the edge effect. Several approximations of material behaviors were tested, showing how the simulations are sensitive to the simplifications introduced in the material descriptions.

It is necessary to do integral measurements of the machine's parameters in order to perform a better comparison. As a matter of fact it is not easy to estimate the actual efficiency of the hardening machine and hence to know how much kW are really lost in the gear and in the coil. Therefore in the simulations the power was an unknown, and hence the decision to calibrate it by reaching the same depth of the 816°C isotherms. In this way, considering an efficiency of 0.8 of the hardening machine, the power lost in the coil and in the gear during the simulated process just reach about 85% of the actual one. This difference may has an effect on the underestimation of the 927°C isotherm of the simulations. As a result it is necessary for the simulations to have a precise reference, such as the current flowing in the coil during the process.

6. Conclusion

The importance of being able to adequately simulate induction hardening processes is generally accepted by the process development community. As a matter of fact FEM software allows the designers to avoid a trial and error approach that is costly and time consuming, in defining the induction hardening parameters.

The study of sensitivity presented in this work, applied to the fast induction treatment of a 4340 steel spur gear, shows the results that is possible to obtain with numerical models.

The description of relative magnetic permeability as a function of temperature and magnetic field strength, the thermal properties of materials when exposed to high heating rates, the shift of metallurgical transformation temperature, remain complex issues that are quite difficult to reproduce in numerical models.

On way to validate the prediction of the electromagnetic coupled with thermal phenomena by the simulations, the present work proposed various approximations of material behaviors, showing how the simulations are sensitive to the simplifications introduced in the material descriptions. In addition, the comparison with the experimental results showed how difficult it is to properly reproduce the experimental profiles of temperatures. As a matter of fact, if one calibrates his model in order to have an accurate temperature at a given depth for a given time, the temperature profiles tend to not be accurate at other locations, nor at other times.

This work also shows that it would be important to have a precise reference, such as the current flowing in the coil during the process, in order to be able to perform a better comparison.

Therefore this study should be a motivation to further improve numerical models and in particular it would be interesting:

- To perform integral measurements of the machine's parameters such as the current in the coil, in order to have a precise reference for the simulations.
- To perform measurements in order to understand the real behavior of relative magnetic permeability since there is no data in literature for AISI 4340.

- To develop numerical models that better describe the real behavior of the material's properties (relative magnetic permeability as a function of temperature and magnetic field).
- To compare different recipes of hardening, for example with preheating phase. It should be necessary to have lower temperature's lacquers.

Bibliography

[1] Lupi S., *"Appunti di elettrotermia", A.A. 2005-2006;*

[2] Larregain B., Vanderesse N., Bridier F., Bocher P., Arkinson P., *"Method for accurate surface temperature measurements during fast induction heating"*, Proceedings of the 26th ASM Heat Treating Society Conference 2011;

[3] Lupi S., Dughiero F., Forzan M., "*Modelling Single- and Double-Frequency Induction Hardening of Gear-Wheels*". The 5th International Symposium on Electromagnetic Processing of Materials, 2006, Sendai, Japan, ISIJ;

[4] Totten G. E., Maurice A. H. Howes, "*Steel Heat Treatment Handbook*", New York, Marcel Dekker, 11A, 11B, 1997;

[5] Ang S., Oliva A., "*power switching converters",* second edition, Taylor & francis Group, 2005;

[6] Rudnev V., Metallurgical fine points of induction hardening, 2005;

[7] Rudnev V., Loveless D., Cook R., Black M., "*Handbook of Induction Heating*", CRC Taylor & Francis (2003);

[8] Candeo A. *et al*, "*Multiphysics Modeling of Induction Hardening of Ring Gears for the Aerospace Industry*" IEEE Transactions on Magnetics, Vol. 47, No. 5 (2011), pp. 918-921;

[9] Barka N., "*Etude de sensibilité du profil de dureté des engrenages traités thermiquement par induction en foncion paramétres machine*", PhD Thesis, ETS Montréal, 2011;

[10] Billiard V., *"Modélisation de la phase de refroidissement d'un procédé de trempe par induction",* Master thesis, ETS Montréal, 2010;

[11] Spezzapria M., *"Simulazione numerica del processo di tempra ad induzione di ruote dentate per l'industria aeronautica",* Master thesis, Università Degli Studi Di Padova, 2011;

[12] Schlesselmann D., Jestremski M., Rodman D., Nacke B., *"numerical simulation methods for complex induction hardening process",* Institute of electrotechnology and Institute of Material science, Leibniz University of Hanover;

[13] Rudnev, V., Loveless, D., Cook, R., Black, M., *"Handbook of Induction Heating",* CRC Taylor & Francis (2003);

[14] Martin Fisk, *"Simulation of Induction Heating in Manifacturing"*, Lulea University of Technology, Department of Applied Physics and Mechanical Engineering;

[15] Miklòs Kuczmann, *"Potential Formulations in Magnetics Applying the Finite Element Method",* Laboratory of Electromagnetic Fields *"Szèchenyi Istvàn",* University Gyor, Hungary, 2009;

[16] K.D. Clarke, C.J. Van Tyne, "*Effect of Prior Microstructure and Heating Rate on Austenite Formation Kinetics in Three Steels for Induction Hardened Components",* Progress Report, Department of Metallurgical and Materials Engineering, Colorado School of Mines, Golden, USA, 2005;